Investigation into PI Controller Output Ripple in MRAS Based Electric Drives

Muez Shiref

H.D, M.Sc.

A thesis submitted for the degree of
Doctor of Philosophy

September 2013

School of Electrical and Electronic Engineering

Newcastle University
United Kingdom

School of Electrical and Electronic Engineering

Abstract

In *Sensorless* speed drives, which employ a model reference adaptive system (MRAS) with a PI based adaptation mechanism, the gains of the adaptation mechanism play an important role into the general performance of the drives. The higher the gain, the faster the response and the more robust the drive is going to be against load disturbance. Although it is desirable to utilise an adaptation mechanism with high PI gains, it was demonstrated that high gains will cause the estimated speed to exhibit a high level of noise. More recently it was identified that the generated noise consists of high-order harmonics.

As far as the literature is concerned, even though the high-order harmonic phenomenon was identified and addressed by few researchers, there was no description in their literature of the generated high-order harmonics or an assessment of their effect in terms of being problematic.

Therefore, the aim of this research is to not only investigate the generation of high-order harmonics, but also to establish whether any generated noise in the estimated speed bear an effect on the overall speed estimation process.

An MRAS based speed estimator is implemented to calculate the rotor flux-linkage and the speed estimates required in achieving field orientation and establishing speed control. An investigation has been carried out to gauge how the PI controller gains can influence the speed estimation process of the drive system. As well as examining the estimated speed for any trace of excessive noise and harmonics generation.

It is revealed experimentally that no high-order harmonics were generated while implementing an adaptation mechanism with high PI gains. However, it was found that high PI gains do causes the estimated speed to become relatively noisy and also starts to carry some fundamental frequency components relevant to the stator's electrical frequency. Therefore a programmable adaptive adjustment mechanism has been successfully developed not only to avoid the excessive generation of noise but also improve the speed estimation process. The performance of both of the static adaptation mechanism and the proposed adaptive one was assessed and compared.

Dedication

This dissertation is lovingly dedicated to my dear mother,

Latifa Amer Mohamed Misurati.

هذه الأطروحة مكرسة بمحبة إلي والدتي العزيزة،

" لطفيّة " عامر محمد المصراتي.

Acknowledgments

I would like to sincerely thank my supervisor, Dr. Matthew Armstrong, for his professional guidance and support throughout the course of the research.

I would like to acknowledge the assistance provided by all the technical support staff in the School of Electrical and Electronic Engineering.

Finally, I would like to express my true gratitude to my family for their continuous support and unconditional affection. And also I would like to thank my friends back home for their unwavering belief in me.

Table of Contents

List of Figures

Nomenclature

Principle Nomenclature

Subscripts:

a, b, c	phases of the original three-phases system, stator phase variables,
(d, q)	axes of the two-phase system in the rotating reference frame,
(α, β)	axes of the two-phase system in the stationary reference frame,
(d^r, q^r)	rotor direct and quadrature axes.
(d^s, q^s)	stator direct and quadrature axes
s	stator,
r	rotor,

Superscripts:

s	stationary reference frame,
r	rotor reference frame,

ia_s, ib_s, ic_s	three-phase stator current in the stationary reference frame,
va_s, vb_s, vc_s	three-phase stator voltage in the stationary reference frame,
$\left(v_{ds}{}^s, v_{qs}{}^s\right)$	(d, q) - components of stator voltages in the stationary reference frame
$\left(i_{ds}{}^s, i_{qs}{}^s\right)$	(d, q) - components of stator currents in the stationary reference frame
$\left(\psi_{\mathrm{dr}}{}^{\mathrm{s}}, \psi_{\mathrm{qr}}{}^{\mathrm{s}}\right)$	rotor flux-linkage vector in the stator reference frame,
$\left(\hat{\psi}_{\mathrm{dr}}{}^{\mathrm{s}}, \hat{\psi}_{\mathrm{qr}}{}^{\mathrm{s}}\right)$	estimated rotor flux-linkage vector in the stator reference frame,
$\left(\psi_{\mathrm{ds}}{}^{\mathrm{s}}, \psi_{\mathrm{qs}}{}^{\mathrm{s}}\right)$	stator flux-linkage vector in the stator reference frame,
L_{ls}, L_{lr}	stator and rotor leakage inductances
$\mathrm{L_s}, \mathrm{L_r}$	stator and rotor self inductance
L_m	mutual inductance
σ	leakage inductance
PO	percentage overshoot

R_s	stator equivalent resistance
R_r	rotor equivalent resistance
RPM	revolutions per minute
Fs	sampling frequency
T_r	rotor time constant
Ts	sampling time
T_e	electromagnetic torque
T_L	load torque
q	reactive power
$\hat{\omega}_r$	estimated rotor speed
ω_r	actual rotor speed
ω_r^*	speed demand
θ_r	rotor flux angle
B	friction coefficient
J	moment of inertia

List of Acronyms

AC	Alternating Current
ADC	Analogue to Digital Converter
AFFO	Adaptive Full-order Flux Observer
AI	Artificial Intelligence
APFO	Adaptive pseudoreduced-order Flux Observer
CM	Current Model
DAC	Digital to Analogue Converter
DC	Direct Current
DSP	Digital Signal Processor
DTC	Direct Torque Control
EKF	Extended *Kalman* Filter

ELO	Extended *Luenberger* Observer
EMF	Electro-motive Force
FFT	Fast *Fourier* Transform
FL	Fuzzy Logic
FLC	Fuzzy Logic Control
FOC	Field Oriented Control
GA	Genetic Algorithm
HPF	High-pass Filter
IM	Induction Motor
LPF	Low-pass Filters
MMF	Magneto-motive Force
MRAC	Model Reference Adaptive Control
MRAS	Model Reference Adaptive Systems
MSE	Mean-squared Error
NN	Neural Network
OLS	Ordinary Least-Squares
PCLPF	Programmable Cascaded Low Pass Filter
PI	Proportional-Integral
PMSM	Permanent Magnet Synchronous Motor
PU	Per-unit
PWM	Pulse Width Modulation
RFO	Rotor Flux Oriented
RTI	Real Time Interface
RTW	Real Time Workshop
SA	Simulated Annealing
SM	Sliding Mode
SMC	Sliding Mode Control
SVM	Space Vector Modulation

UKF	Unscented *Kalman* Filter
V/f	Volts/Hertz
VM	Voltage Model
VSC	Variable Structure Control
WNN	Wavelet Neural Network

Chapter 1 – Introduction

1.1 AC Motor Drives

Until recently, variable-speed ac drives have been employed to carryout relatively undemanding tasks in applications where the use of DC motors is inappropriate due to harsh working environments and their shortcomings owing to their construction consisting of the commutator and brushes. That is to say, DC motors require periodic maintenance; they cannot be used in explosive or corrosive environments and they have limited commutator capability under high-speed and high-voltage operational conditions [1].

The lower cost of AC motors has also been a crucial economic factor, especially to manufacturing industries where multiple-motor systems are used, for example: steel works, rolling mills and the paper and plastic-film industries [2], because of the high cost of efficient static inverters with fast switching frequency. However, in consideration of the extensive advancement in the field of power electronics, there is a prevailing tendency toward the implementation of inexpensive and more effective power converters, including single motor AC drives that have begun to compete favourably on a purely financial basis with DC drives [3].

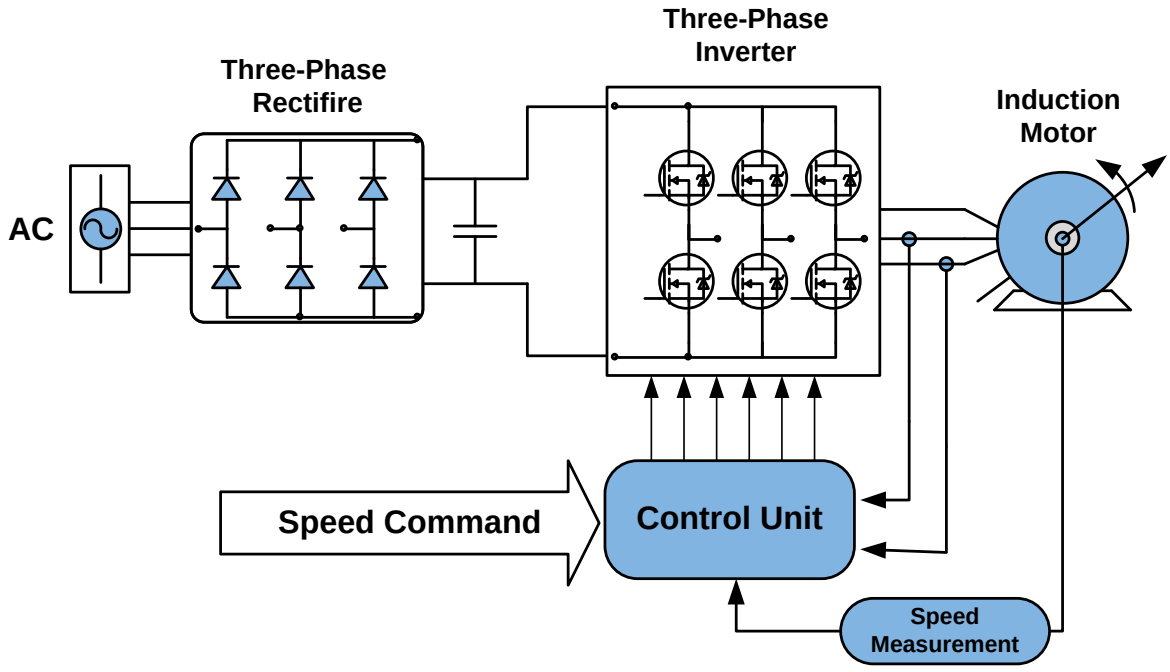

Figure 1. 1 Schematic diagram of a generic AC motor drive

Induction motors in general and squirrel-cage rotor induction motors in particular, are simple, rugged and one of the most cost effective machines available for all power ratings. This in turn makes AC drive systems containing a squirrel-cage induction motor have a certain cost advantage [3]. Owing to their excellent control capabilities, variable speed drives that incorporate AC motors and utilize modern static converters and torque control can compete well with high-performance four-quadrant DC drives [3].

Since the majority of the energy consumed in industry can be traced back to high-powered but relatively unsophisticated machinery, such as: pumps, fans, blowers, grinders and compressors, the conservation of energy is considered an additional economical advantage where there is evidence that negates the requirement for high dynamic performance drives. However, speed control can bring substantial energy savings in most cases. High-performance induction motor drives, such as those for machine tools or elevators, in which an accurate control of torque and position is essential, are still relatively rare, even though many sophisticated control techniques have already reached the stage of practicality [1].

1.2 Vector Control Based Drives

Vector control drives are one particular type of torque-controlled drive. The other type of high-performance torque-controlled drive is a so-called direct torque-controlled drive [3]. Within this drive, direct torque control is achieved by direct and independent control of the flux linkages and electromagnetic torque through the selection of optimal inverter switching modes, which generates fast torque response, low inverter switching frequency, and low harmonic losses.

Vector control of AC motors was pioneered in Germany by *Blaschke* and *Hasse* starting in 1968 and in the early 1970s, and further developed by *Leonhard* in the 1980s, opened up the opportunity for AC drives to not only match the performance of a DC drive but to also improve upon it. Similarly, direct-torque controlled drives were introduced in 1984 by *Takahashi* and *Toshihiko* in Japan and also in Germany by *Depenbrock* [4-6].

Nowadays, vector control drives have achieved a high degree of maturity, becoming increasingly popular in a wide range of applications and have established a substantial and continually increasing market worldwide [4-6]. Vector control techniques incorporating fast microprocessors and digital signal processors have made possible the application of induction motors and synchronous motor drives for high-performance application where traditionally only DC motors drives have been applied. In the past,

such control techniques would not have been possible because of the complex hardware and software required to solve the control problem. Torque control in AC machines is achieved by controlling the motor currents. In an AC machine, in contrast to DC machines, both the phase angle and the modulus of the current has to been controlled, meaning that the current vector has to be controlled, hence the terminology 'vector control' [3].

Furthermore, in DC machines, the orientation of the field flux and armature m.m.f. is fixed by the commutator and the brushes, while in AC machines, the field flux and the spatial angle of the armature m.m.f. require external control. In the absence of this control, the spatial angle between the various fields in AC machines varies with the load and may yield unwanted oscillating dynamic response. By means of a vector control within AC machines, the torque and flux producing current components are decoupled and the resultant transient response characteristics are similar to those of a separately excited DC machine. Such a system will adapt to any load disturbances or reference value variations as fast as a DC machine [3].

As a result of rapid developments in the field of microelectronics, torque control of various types of AC machines is expected to become a commonly used technique. Even when high dynamic performance is not required, servo-like high-performance plays a secondary role to reliability and efficiency in terms of energy savings [1, 3].

1.3 Sensorless Speed Control and Associated Issues

In the past two decades, significant efforts have been made to introduce sensorless control by means of vector and direct torque techniques [3, 7-9]. The drives are usually referred to as 'sensorless' drives, regardless of the fact that there are other sensors in the drive system, such as current and voltage sensors. This is because the term 'sensorless' in this context refers only to the speed and shaft sensors.

Sensorless vector drives have become the favourable option for industry and almost every large manufacturer such as *Control Techniques plc*, *Siemens*, *Hitachi*, *Yaskawa*, *Eurotherm* has introduced a sensorless induction motor drive [3]. High-performance sensorless drives have been successfully applied in medium and high speed regions. However, the inability to operate at very low frequencies without speed or position sensors is still considered a critical problem, especially for sensorless induction motor drives [9]; in view of the fact that some applications such as cranes, traction drives and

presses are required to maintain the desired torque down to zero speed [10]. Over the past twenty years, a significant amount of research effort has been focused on extending the operating region of sensorless drives near zero stator frequency [11, 12]. In general, to solve the problems that occur at low frequencies, a number of special techniques have also been proposed by various investigators. For example, techniques that deliberately introduced asymmetries within the machines, or in which extra signals are injected into the stator [3, 13].

So far, these techniques have not been accepted by industry as a consequence of their side effects and other problems. It would appear that, as a general rule, industrially acceptable sensorless solutions must be applicable to mass produced motors, except when the drive system is an integrated drive where the motor, inverter and controllers are part of a single system provided by the same manufacturer. In such a case, special techniques are also possible that will be discussed briefly later in this chapter and in more detail within chapter two [3].

Conventionally, the speed of an electrical machine can be measured conveniently by DC tacho-generators, which are by today's standard are of a brushless design. The rotor position can be measured either by using electromagnetic resolvers or digitally by using incremental or absolute encoders. Optical encoders are one of the most widely used positional-based sensors currently in use. Electromagnetic resolvers are popular for measuring the rotor position because of their rugged construction and higher operational temperature [3]. Obviously, if the rotor position is monitored then the speed, which is the first derivative of the position, can be estimated directly from this position but the speed estimation accuracy is limited by both the resolution of the position transducer and the sampling rate.

In order to reduce the total hardware complexity and cost while maintaining mechanical robustness and reliability of the drive and also avoiding the degradation of noise immunity, it is desirable to eliminate the aforementioned sensors within vector controlled and direct-torque controlled drives. Not only does an electromechanical sensor increase the inertia of the motor, which is undesirable in high-performance drives, but it also increases the maintenance requirements [14]. In very small motors, this almost becomes a requirement as it is infeasible to use electromechanical sensors. In a low-power torque controlled drive, the cost of such sensors can almost be equal to the rest of the development costs for the entire motor. Speed sensors can neither be mounted on motors within drives that operate in hostile environments nor in high-speed

drives where the rated speed is increased to effectively boost power density and efficiency. The reason for this is due to the high rotational speeds, where the centrifugal forces on a rotating motor rotor can be exceedingly high that will cause the constructive materials to disintegrate [15].

As the efficiency and performance of real-time computational DSPs improve, so too can the speed and position estimation be improved through the use of software-based state-estimation techniques, utilising stator voltage and current measurements. It is also possible to use other types of solutions, for instance stator phase third harmonics or rotor slot harmonics [3, 7, 13].

In short, sensorless drives should facilitate the following characteristics: a reduction of hardware complexity and cost, increased mechanical robustness and overall ruggedness, operation in hostile environments, higher reliability, decreased maintenance requirements, increased noise immunity, unaffected machine inertia and applicability to off-the-shelf motors [3, 9, 13].

Regarding the speed control of sensorless-based drives, there are a number of speed estimation techniques that vary from open-loop speed estimators to artificial intelligence based estimators. A number of techniques have been proposed for rotor speed estimation in sensorless induction motor drives, based on the machine fundamental model [3, 16]. Among these techniques, model reference adaptive system (MRAS) based schemes are the most common strategies employed due to their relative simplicity and low computational effort[12].

MRAS based schemes are arguably the most popular speed estimators because they deliver high control performance with relative simplicity. In an MRAS based speed estimator, the estimation is achieved by means of calculations that are based on electrical quantities that are in essence, the measurements of current and voltage. MRAS based estimators will be discussed in detail in chapter 2.

An MRAS system consists of two estimators that are the reference model and the adaptive model. The reference model is based on the motor’s stator equations, while the adaptive model is based on the rotor’s equations. These estimators independently calculate the state variables, which are compared to derive the error. This error is then driven into the adaptation mechanism that estimates the speed of the motor. This estimated speed is used to adjust the adaptive model, ensuring that the drive system performs optimally.

In the last two decades, a considerable amount of research has been undertaken to increase the accuracy of all sensorless speed motor drives, including MRAS based speed drives [3, 8, 9]. Particular, attention and effort has been dedicated to improve the speed estimation performance of such drives at low and near zero speeds, where the estimation performance is usually compromised. This is due to imprecise observations of dynamic quantities and high sensitivity to variation of motor parameters [9, 11, 12, 17-19].

Various control algorithms and numerous solutions utilising MRAS have been proposed, ranging from the trial of different types of MRAS based systems. Other solutions have included the replacement of the constant adaptation mechanism with an intelligent mechanism based on a combination of fuzzy-logic and neural networks, as well as proposing a variety of dynamic reference models to estimate online the induction motor parameters such as the stator and the rotor resistance [20-27].

Interestingly enough, despite the wide range of research and proposed solutions in the area of sensorless speed estimation via means of model referencing, there has been an issue with respect to the resultant generated noise as the result of high PI controller gains, which have received very little attention [28, 29]. This noise, which is produced by the adaptation mechanism of the PI controller, may imposes upon the estimated speed by containing high-order harmonics as the value of the PI controller gains Kp & Ki are increased.

The issue of noise in general has been first pointed out by *Schauder* [30], who pioneered sensorless speed identification via MRAS, in the context of analysing the dynamic response of the MRAS based speed identification drive. The analysis revealed that the bandwidth with which the measured speed is tracked is only limited by noise considerations. *Schauder's* proof has been supported by many researchers, particularly by *Peng* and *Fukao* [31] by building upon *Schauder's* work. This resulted in two variations of an MRAS based speed identification, namely the back-emf based MRAS and the reactive power based MRAS. *Peng* and *Fukao* not only subscribed to *Schaudre's* analysis but also proved that that K_p and K_i of the PI adaptation gains should be set as high as possible in order to achieve a fast and robust dynamic response.

Over the years it has been established that a high adaptation mechanism gain can help an MRAS based system to achieve a fast and robust dynamic response, particularly during a transient state and also against a mechanical load disturbance [3, 12, 30-32].

As a part of *Wang's* [33] detailed investigation onto the effect of parameter variation effect in MRAS based sensorless drive, it was reported that high adaptation gains were necessary not only to maintain fast and robust dynamic responses, but also because the input into the PI controller is essentially the angular difference between the two rotor flux-linkage estimates. Furthermore, it was shown that the high PI gains caused the speed estimate to exhibit a high-level of noise. In [33], the authors resorted to applying a low-pass filter to the estimated speed throughout the whole of the experimental investigation. However, the authors in [33] conceded that implementing a low pass caused a time delay that significantly affected the response time.

As far as the literature review is concerned, the alleged high-order harmonics phenomenon has been identified by *Santhosh* and *Kojabadi* [28, 29] yet only investigated by *Kojabadi* [29], which is the only published piece of research that has been dedicated to proving that the effect of the PI controller on the generation of noise and harmonics does exist.

In [29], the effect of the adaptive PI controller gain on the speed estimation was investigated in the context of implementing an adaptive full-order flux observer based MRAS; the design of which incorporates the estimation of the IM stator resistance. The proclaimed simulation and experimental tests demonstrated that with larger gains for the adaptive PI controller, the convergence for the speed estimation is fast. However, the high-order harmonics and noise are included in the estimated speed, which means that the process of selecting PI gain values of the adaptive mechanism is a compromise between either achieving a fast response or a high robustness to noise.

The work published by *Kojabadi* [29] was dedicated to a thorough investigation into the effect of the adaptation mechanism gains on the speed estimation and the generation of noise. Even though it was reported that the simulation and experimental investigation demonstrated that high PI gains caused the estimated speed to contain high-order harmonics and noise, no description was included in the literature with which the

aforementioned effect was explained. Furthermore, *Kojabadi* and the other researchers didn't include within their literature any accounts that quantified the extent of this effect and whether or not the generated noise and harmonics posed a problem.

1.4 Research Objectives

In view of the fact that while the phenomenon of generated high-order harmonics within the estimated speed measurements has been acknowledged for many years, no studies within the existing literature have offered a detailed description to either show how the gains of the adaptation mechanism can cause the generation of such harmonics in the estimated speed or assess their effect on the performance of the speed estimation process. The main goal of this research is to evaluate a high-performance sensorless vector control drive. An MRAS based speed estimator is implemented to calculate the rotor flux-linkage and the speed estimates required to achieve field orientation and speed control. The dynamic performance of such a scheme has substantial dependency on the design of an adaptation mechanism with a PI controller, which is employed to tune the estimated speed. A detailed investigation has been carried out to gauge how the PI controller gains influence the speed estimation process of the drive system.

Furthermore, since there has been neither a study dedicated to tackle the alleged phenomenon of high-order harmonics, nor explicitly demonstrating the existence of such a phenomenon. The research reported in this thesis will not only examine the estimated speed for any excessive noise and resulting generated harmonics by analysing the harmonic spectrum, but also present an unparalleled detailed description on how the PI gains of the adaptation mechanism can cause the estimated speed to exhibit a high level of noise. The harmonic analysis will present a unique insight into the characteristics of the generated noise and its association to the motor's stator frequency. More importantly, the harmonic analysis will unequivocally show that even though in the real drive system the high PI gains can cause the estimated speed to become noisy, the presence of high-order harmonics in the estimated speed is insignificant.

Therefore, in order to overcome the excessive generation of ripple in the estimated speed, a programmable adaptive algorithm to replace the static PI controller of the adaptation mechanism has been successfully developed to not only avoid the excessive

generation of noise, but to also improve the dynamic performance of the sensorless speed drives. The performance of both the static adaptation mechanism and the proposed adaptive algorithm has been thoroughly assessed and compared. The main objectives of this study can be summarised as follows:

1. investigate and quantify the noise generation effects caused by the gains in the adaptation mechanism in a sensorless vector control system, based upon a standard direct vector controller and a standard rotor flux-linkage based MRAS speed estimator
2. demonstrate that while high PI gains can improve the drives performance in terms of being both dynamically robust and achieving fast convergence, they cause the estimated speed to exhibit a rising level of noise ripple
3. analyse the harmonic spectrum of the generated noise in the estimated speed signal in order to reveal its frequency composition
4. analyse the harmonic spectrum of the actual speed signal to investigate for any transfer of noise components
5. develop a novel adaptive algorithm to replace the static PI controller of the adaptation mechanism, maintaining a robust dynamic response and avoiding the generation of unnecessary ripple in the estimated speed
6. confirm the effectiveness of the modified adaptation mechanism by experimental evaluation under both no-load and loaded conditions.

1.5 Contribution to Knowledge

The excessive generation of ripple within the estimated speed causes the actual speed to deviate from the reference speed in the sensorless mode. Although existing research into sensorless speed estimation via model referencing has acknowledged the generation of noise and subscribed to the notion of high-order harmonics generation, it has been mainly restricted to improving the drives performance at low- and near zero-speed with no attempts to incorporate a solution to overcome the issue of noise. The contribution of this thesis to knowledge lies in the following:

1. the presentation of a detailed evaluation via simulation and experimental implementation of the drives performance under different adaptation mechanism gains in both transient and steady state

2. an unprecedented harmonic analysis investigating the frequency spectrum of the generated noise in the estimated speed is presented that clearly disproves the existence of high-order harmonics
3. the characteristics of the generated ripple in the estimated speed and its relationship to the motors stator frequency are revealed
4. a novel adaptive adaptation mechanism is developed to replace the fixed gains adaptation mechanism
5. enhanced speed estimation is verified and a more robust dynamic performance is achieved experimentally.

1.6 Thesis Outline and structure

A review of the different types of MRAS based speed estimators in addition to a survey on the existing literature that proposes solutions to either tackle performance issues or improve upon them is provided in chapter 2. Chapter 3 describes the (d, q) dynamic model of the induction machine along with the associated axes transformations, illustrates the dynamic modelling of the MRAS based on the flux vector estimation in the stationary reference frame and presents the discrete-time representation of modelled MRAS based system. Chapter 4 presents the Simulink® based simulation results acquired during the preliminary stage of the research and chapter 5 describes the experimental set up and the associated hardware used to conduct the research. The experimental results acquired during the real-time implementation investigating the performance of the developed MRAS based speed estimator under different PI gains are put forward in chapter 6. In addition, the results of the harmonic analysis that was applied to examine the harmonic spectrum of both the estimated and the actual speed signals are presented. Chapter 7 proposes a new adaptive algorithm as well as the experimental results that validate its functionality. Finally, chapter 8 includes the overall discussions and conclusions of this research and highlights the main findings and the direction of further research.

Chapter 2 - MRAS Based Speed Estimators

2.1 Introduction

Mechanical sensors are often, if not always, undesirable due to space restriction and added cost and complexity. One reason why the omission of mechanical sensors has become a prominent topic is the fact that the powerful microcomputers, which are now available at reasonable cost for the control, can be applied to estimating and controlling unmeasurable internal quantities; hence it is rational to utilise their potential of producing an estimate of speed. Since only terminal quantities, i.e. stator voltages and currents are measured from which the information on the state variables such as rotor flux-linkage, back-emf and the speed of the motor must be derived, given a nominal knowledge of the important motor parameters. An ideal estimation algorithm should produce the necessary signals on the flux wave as well as the mechanical speed and in addition, provide information on changing motor parameters so that the flux and speed models can remain tuned to the motor [3, 34].

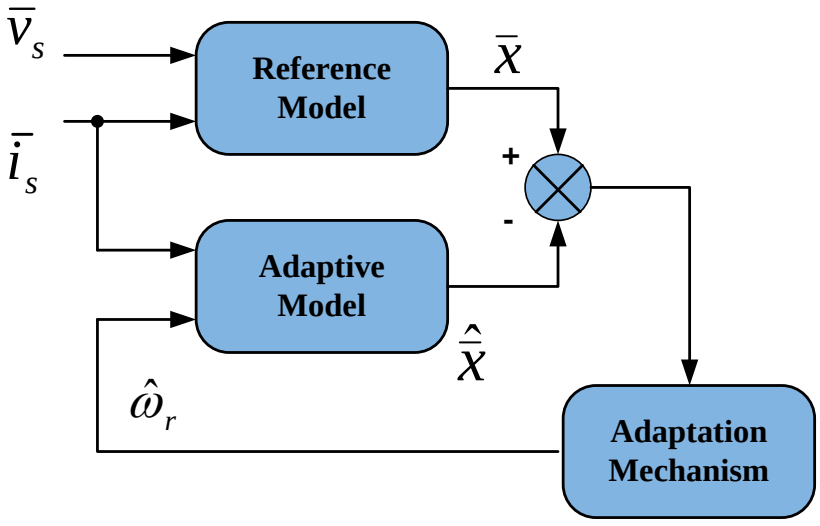

(a) MRAS-based speed estimator scheme.

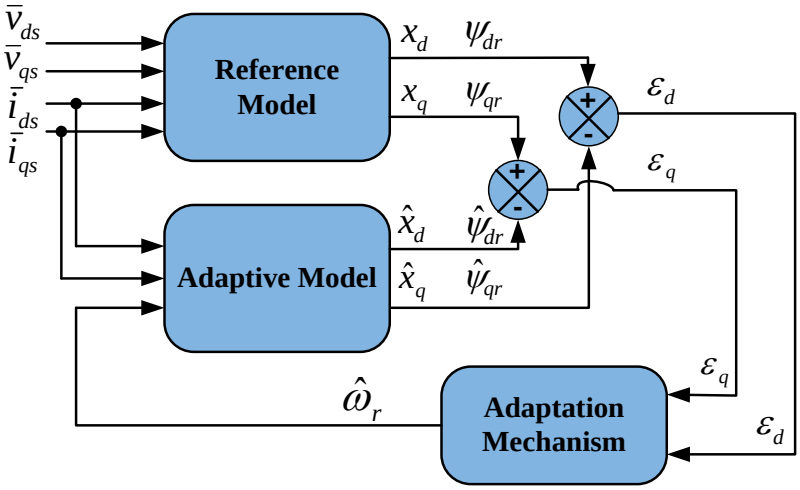

(b) MRAS-based speed estimator scheme expressed in space-vector notation.

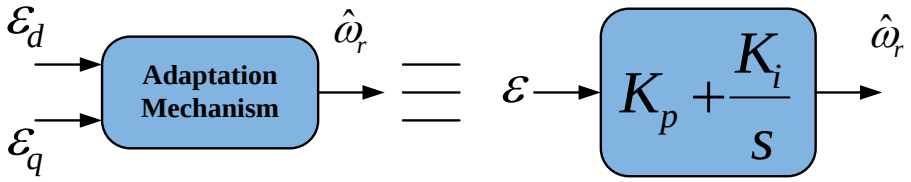

(c) Adaptation mechanism; speed tuning signal.

Figure 2. 1 MRAS based speed estimator.

MRAS is considered one of the most popular estimation systems, especially within the field of induction motor control. Not only can they deliver high control performance with relative simplicity, but when incorporated with the vector control technique, the mechanical speed sensors become dispensable, which is why MRAS is at times referred to as an estimation technique rather than a control. Since mechanical sensors degrades system reliability, especially in a hostile environment and also increases the overall system cost, sensorless control has significant advantages. The speed estimation is achieved by means of calculation based on electrical quantities, which are in essence, the measurements of current and voltage [6, 35-37].

In an MRAS system, state variables are for example, the rotor flux-linkage components of the induction machine that are obtained by using measured quantities, such as stator currents and voltages. These quantities are estimated using a reference model and are

then compared with the state variables estimated by using an adaptive model. The difference between these state variables is then used in an adaptation mechanism that generates the estimated value of the rotor speed, which adjusts the adaptive model to ensure that the drive system performs optimally.

Such a scheme is shown in figure 2.1 (a), where a compact space vector notation is used. Figure 2.1 (b) corresponds to an actual implementation for which the components of the vector space are shown.

2.2 Types of MRAS-based Speed Observers

There are different techniques that employ MRAS as a speed estimator. The methods that are used to categorise vary in different text books and other pieces of literature. Conservatively, there are two categories of MRAS based speed estimator: conventional MRAS and AI based MRAS.

2.2.1 Conventional MRAS Based Speed Estimators

In a conventional MRAS speed observer, which is based on the work originally proposed by *Schauder* [30], the speed estimation is achieved by direct synthesis from state equations. These equations are represented as two estimators where one estimator is based on stator equations, which is basically a voltage model, and the other estimator is based on the rotor equations, which is basically a current model. The appropriate adaptation mechanism can be derived by using Popov's criterion of hyperstability [3, 13, 30]. Popov's hyperstability criterion generalises the absolute stability for nonlinear systems. In contrast with other stability definitions, hyperstability explicitly takes into consideration both the influence of the input and the initial conditions of the states. Furthermore, nonlinear control using hyperstability theory yields robust stability [38]. Therefore, hyperstability theory is a useful tool for analysis of an extensive class of systems and also beneficial when applied for controller design [39].

The application of Popov's hyperstability criterion results in a stable and responsive system, where the difference between the state variables of the reference model and the adaptive model produces the state error that is manipulated into a speed tuning signal, ε, which is fed into a PI-type controller shown in figure 2.1(c) and then in turn produces the estimated speed $\hat{\omega}_r$. There are three main variations that fall under conventional MRAS based speed estimators, they differ based on the type of the tuning signal.

2.2.1.1 Rotor Flux-linkage Based MRAS Speed Estimator

Rotor flux-linkage based MRAS method was originally proposed by *Schauder* [30]. In this technique, the two estimators, which are the reference model and the adaptive model, independently estimate the rotor flux-linkage components: $\psi_{dr}{}^{s}$ and $\psi_{qr}{}^{s}$, by using the difference between the rotor flux-linkage estimates to drive the speed of the adaptive model to that of the actual speed. The expressions for the rotor flux-linkages in the stationary reference frame can be obtained by using the stator voltage equations of the induction machine, which are transformed to the stationary reference frame. These give equations (2.1) and (2.2), which are now rearranged to calculate the rotor flux-linkages:

$$\psi_{dr}{}^{s} = \frac{L_r}{L_m}[\int(v_{ds} - R_s i_{ds})dt - \sigma L_s i_{ds}] \tag{2.1}$$

and

$$\psi_{qr}{}^{s} = \frac{L_r}{L_m}\left[\int\left(v_{qs} - R_s i_{qs}\right)dt - \sigma L_s i_{qs}\right], \tag{2.2}$$

where L_s is the stator transient inductance. These two equations represent the so-called voltage model, which do not contain the rotor speed and are therefore considered to be a reference model. Conversely, when the rotor flux equations of the induction machine are expressed in the stationary reference frame, they contain both the rotor flux-linkage estimates and the speed. The equations are expressed as

$$\hat{\psi}_{dr}{}^{s} = \frac{1}{T_r}\int(L_m i_{ds} - \hat{\psi}_{dr}{}^{s} - \omega_r T_r \hat{\psi}_{qr}{}^{s})dt \tag{2.3}$$

and

$$\hat{\psi}_{qr}{}^{s} = \frac{1}{T_r}\int(L_m i_{qs} - \hat{\psi}_{qr}{}^{s} - \omega_r T_r \hat{\psi}_{dr}{}^{s})dt, \tag{2.4}$$

where T_r is the rotor time constant. These two equations correspond to the so-called current model, which contains the rotor speed and therefore represents the adaptive model. The reference and adaptive models are used to estimate the rotor flux-linkages and the angular difference of the outputs of the two estimators, $\varepsilon_{\psi} = (\psi_{qr}{}^{s}\hat{\psi}_{dr}{}^{s} - \psi_{dr}{}^{s}\hat{\psi}_{qr}{}^{s})$, is used as the speed tuning signal. This tuning signal is then fed into a linear PI controller, which provides the estimated rotor speed as shown in figure 2.2.

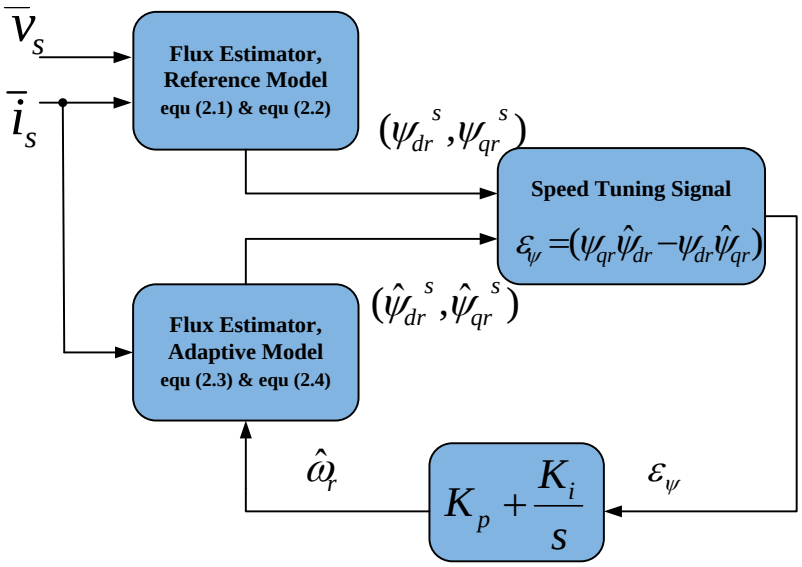

Figure 2. 2 Rotor flux-linkage based MRAS.

As discussed in the previous section, the reason for using a PI controller and the angular difference ε_ψ, is that this will give a stable nonlinear feedback system, which was rigorously proved by Popov's hyperstability criterion. The PI controller tunes the rotor speed value where the error between the two rotor flux-linkage space vectors is not zero ($\overline{\psi_r^{\ s}} \neq \overline{\hat{\psi}_r^{\ s}}$). In other words, when the rotor speed to be estimated $\hat{\omega}_r$ is changed in the adjustable model in such a way that the difference between the output of the reference model and the output of the adaptive model becomes zero, then the estimated rotor speed $\hat{\omega}_r$ is equal to the actual rotor speed ω_r. The error signal actuates the rotor-speed identification algorithm, which makes this error converge to zero. The algorithm is chosen to give a quick and stable response. Following from figure 2.2, the estimated speed can be expressed as

$$\hat{\omega}_r = K_p \varepsilon_\psi + K_i \int \varepsilon_\psi \, dt. \qquad (2.5)$$

Sensorless speed estimators that are based on rotor flux-linkage are well established, they have been extensively studied and their ability to deliver excellent performance over a wide range of speed has been verified [3, 20, 33, 40, 41]. Therefore, a rotor flux-linkage based MRAS will be implemented in this research not only because it is believed to be the most commonly implemented MRAS based scheme used for speed estimation but also because its capable of achieving correct speed estimation down to 5% rated speed[3, 33, 40].

2.2.1.2 Back-emf Based MRAS Speed Estimator

The back-emf based technique, which is based on the work of *Peng* and *Fukao* [31], uses a tuning signal based on the back-emf difference and is comparable in structure to the rotor flux-linkage scheme. Similarly, for the rotor flux-linkage, the expressions for the back-emf in the stationary reference frame can be obtained by using the stator voltage equations of the induction machine, where the direct and quadrature axis back-emfs follow from equation (2.6) and (2.7), which in turn are used in a new reference model as shown in figure 2.3.

$$e_d{}^s = \frac{L_m}{L_r}.\frac{d\psi_{dr}{}^s}{dt} = v_{ds} - R_s i_{ds} - \sigma L_s \frac{di_{ds}}{dt} \tag{2.6}$$

$$e_q{}^s = \frac{L_m}{L_r}.\frac{d\psi_{qr}{}^s}{dt} = v_{sq} - R_s i_{qs} - \sigma L_s \frac{di_{qs}}{dt} \tag{2.7}$$

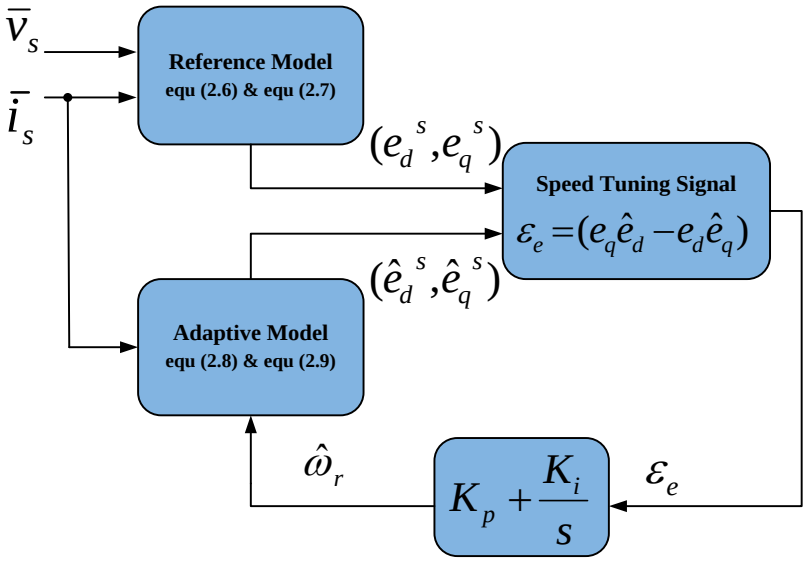

Figure 2. 3 Back-emf based MRAS.

As it can be seen from the equations above, the components of the back-emf, $e_d{}^s$ and $e_q{}^s$, can be obtained without integration, which means that the system will be unaffected by problems associated with initial conditions and drift. Similar to the rotor flux-linkage based scheme described in the previous section, in the back-emf based MRAS the stator voltages can be obtained from the monitored terminal voltages of an inverter-fed drive, or they can be reconstructed by using the inverter's switching states and the monitored DC link voltage. The corresponding back-emf equations for the adaptive model are obtained from equations (2.3) and (2.4) as

$$\hat{e}_d{}^s = \frac{L_m}{L_r}.\frac{d\hat{\psi}_{dr}{}^s}{dt} = \frac{L_m}{L_r}.\left(\frac{L_m i_{ds} - \psi_{dr} - \omega_r T_r \psi_{qr}}{T_r}\right) \quad (2.8)$$

and

$$\hat{e}_q{}^s = \frac{L_m}{L_r}.\frac{d\hat{\psi}_{qr}{}^s}{dt} = \frac{L_m}{L_r}.\left(\frac{L_m i_{ds} - \psi_{qr} - \omega_r T_r \psi_{dr}}{T_r}\right). \quad (2.9)$$

Equations (2.8) and (2.9) are used in the adaptive model shown in figure 2.3, where the speed tuning signal is $\varepsilon_e = (e_q{}^s \hat{e}_d{}^s - e_d{}^s \hat{e}_q{}^s)$, which is proportional to the angular difference between the back-emfs.

2.2.1.3 Reactive Power based MRAS speed estimator

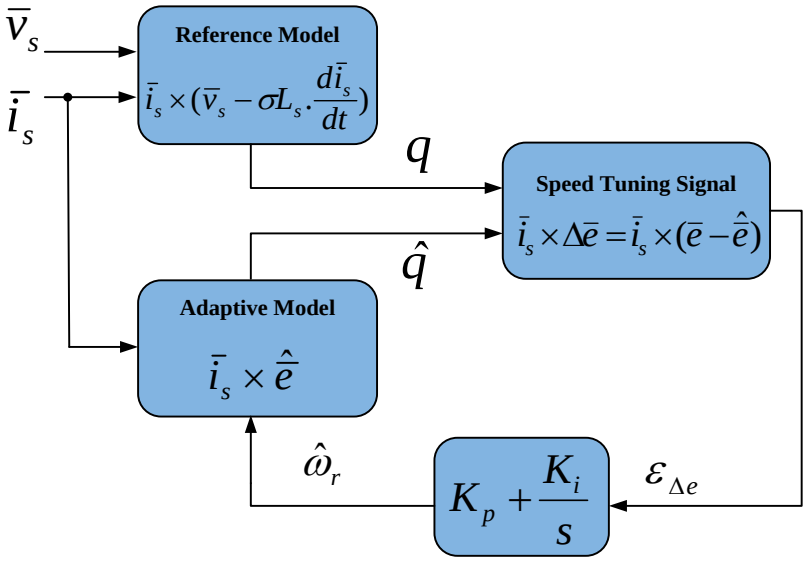

Figure 2. 4 Reactive power based MRAS.

In this scheme, which is also developed by *Peng* and *Fukao* [31], the speed tuning signal is based on the reactive power. At the time, this was a newly defined quantity that is essentially acquired from the cross product of the back-emf difference $\Delta\bar{e}$ and the stator current $\bar{\imath}_s$.

Building upon the back-emf equations, the reference model equation is defined as

$$q = \bar{e} \times \bar{\imath}_s = \bar{\imath}_s \times \left(\bar{v}_s - R_s\bar{\imath}_s - \sigma L_s \frac{d\bar{\imath}_s}{dt}\right) \quad (2.10)$$

where q is the reactive power and $\bar{e}$ is the back-emf vector, which is equal to ($e_d{}^s + je_q{}^s$)

$$q = \bar{\imath}_s \times \bar{v}_s - \sigma L_s \frac{d\bar{\imath}_s}{dt} \tag{2.11}$$

where $\bar{\imath}_s \times \bar{\imath}_s = i_{\alpha s} i_{\beta s} - i_{\beta s} i_{\alpha s} = 0$ and the inductance leakage coefficient $\sigma = 1 - \frac{{L_m}^2}{L_s L_r}$,

$$\therefore q = i_{\alpha s} v_{\beta s} - i_{\beta s} v_{\alpha s} - \sigma L_s \left(i_{\alpha s} \frac{di_{\beta s}}{dt} - i_{\beta s} \frac{di_{\alpha s}}{dt} \right). \tag{2.12}$$

Likewise, the adaptive model can be obtained by building up from the estimated back-emf where the reactive power adaptive model can be derived as

$$\hat{q} = \hat{\bar{e}} \times \bar{\imath}_s = i_{ds}.\hat{\mathrm{e}}_{\mathrm{q}}{}^{\mathrm{s}} - i_{qs}.\hat{\mathrm{e}}_{\mathrm{d}}{}^{\mathrm{s}}$$

$$= \frac{L_m}{L_r}\left[\frac{1}{T_r}\left(\psi_{\mathrm{dr}}{}^{\mathrm{s}}.\mathrm{i}_{\mathrm{qs}} - \psi_{\mathrm{qr}}{}^{\mathrm{s}}.\mathrm{i}_{\mathrm{ds}} \right) + \omega_r \left(\psi_{\mathrm{dr}}{}^{\mathrm{s}}.\mathrm{i}_{\mathrm{ds}} + \psi_{\mathrm{qr}}{}^{\mathrm{s}}.\mathrm{i}_{\mathrm{qs}} \right)\right] \tag{2.13}$$

Respectively, equations (2.12) and (2.13) can be used in a final implementation of the rotor speed observer. The reactive power based MRAS requires neither pure integration of measured variables nor the knowledge of the value of the stator resistance. Therefore, it can be considered as a more effective method than the previous two methods. When this scheme is used in a vector controlled drive, it is possible to obtain satisfactory performance even at very low speeds [20, 31, 32]. The estimator can track the actual rotor speed with a bandwidth that is only limited by noise, so the PI controller gains should be as large as possible. The scheme is insensitive to stator resistance variations and it can be shown that if in a rotor-flux-oriented vector drive, the same T_r is used as in the MRAS based speed estimator, and then the drive will be robust to the variation of T_r as well [3, 31]. Consequently, rotor flux alignment is maintained despite the fact that an incorrect value of the rotor time constant is used. This is due to the accumulative effects of the errors, which also holds for the other MRAS based speed estimators described above. However, the accuracy of the speed estimation system discussed above depends on the transient stator inductance L_s and also on the referred magnetizing inductance $\frac{L_m}{L_r}$. The latter quantity is not too problematic, since it does not change with the temperature. Furthermore, deviation of T_r from its correct value produces a steady-state error in the estimated speed, and this error can become significant at low speed. In general, the scheme can be used at very low speeds as well but not at zero stator frequency. Special care must be taken for the design of this scheme for applications

where there are negative step changes in the torque-producing stator current, otherwise it is difficult to keep the speed stable [32].

2.2.2 AI based MRAS Speed Estimator

In all of the aforementioned MRAS based techniques, there is a reference model and an adaptive model. The adaptive model incorporates the estimated rotor speed that is the output of a suitable adaptation mechanism, which utilises at its input the difference of the estimated state variables of the reference and adaptive models. Moreover, in all of the techniques, the adaptation mechanism is based on using Popov's hyperstability criterion. This has eventually resulted in an adaptation mechanism where the estimated state variables of the reference and adaptive model are manipulated into a speed tuning signal, which is subsequently fed into a PI controller containing the proportional and integrator gains of the adaptation mechanism K_p and K_i. This approach has also required the use of a mathematical model for the adaptive model. A digital implementation of such techniques is relatively simple in terms of processing requirements.

In an attempt to improve the accuracy and increase robustness of the MRAS based speed estimators, the adaptive mathematical model can be replaced by an artificial intelligent (AI) based nonlinear adaptive model. The AI based model can in turn, eliminate the need for a separate PI controller where it can be integrated into the tuning mechanism of the AI based model. Different forms of AI based models can be implemented, such as an artificial neural network (ANN), fuzzy logic or a fuzzy-neural network [1, 3, 9, 13].

There is also the option of implementing different types of speed tuning signals [1, 3, 9, 13]. Similar to the conventional PI controller based MRAS, the adaptation mechanism input signals can also take various forms in the AI based MRAS. Thus, there are various possibilities for the speed tuning signal. The possibilities are even greater since there are many types of ANNs and fuzzy-neural networks. It is believed that some of these solutions can give high accuracy and are robust to parameter variations, even at extremely low stator frequencies [1, 3, 9, 13].

2.3 MRAS in Sensorless Induction Motor Control (Problems & Proposed Solutions)

2.3.1 Introduction

Adaptive control can be realised by different strategies such as gain scheduling, self tuning regulators and via means of dual control. In terms of speed estimation of induction motors, or in other words sensorless control, there are various rotor speed estimation techniques that are proposed in the literature such as: frequency slip calculation, MRAS, speed adaptive flux observer, and extended *Kalman* filter. However, MRAS based speed estimators are probably the most common methods that are used to establish sensorless control of induction motor drives due to ease of implementation and minor computational effort [3, 12, 40]. These techniques monitor the stator voltages and current in order to calculate rotor speed from the machine equations, which are based on the machine basic model [6]. Originally, MRAS has been proposed to solve control problems where the desired performance is specified by a reference model, providing the ideal response of the plant to a given command. Based on the same mechanism, the MRAS approach can also be applied to parameter and state estimation [38, 42].

The most established MRAS scheme is based on the rotor flux-linkage estimation. This scheme was principally developed by *Schauder* [30] to achieve a basic speed control within a reasonable bandwidth, without the use of any shaft-mounted transducers. However, this scheme was proven to have a number of drawbacks, such as: sensitivity to machine parameters, flux-linkage pure integration problems, which may cause DC drift and initial condition problems [3, 9, 30], stator voltage and current acquisition problems, and inverter non-linearity [9, 11]. These problems may limit the estimator's performance at low and zero speed [31]. Applied to a vector control induction motor drive, a stator frequency with good performance above 2Hz has been reported [9, 16, 30]. Speed reversal through zero speed is possible, providing a fast transient is applied. However, operation at zero speed for longer periods of time is not satisfactory due to an incorrect rotor flux-linkage estimation [3, 43].

In order to avoid the problems associated with rotor flux-linkage based schemes, *Peng* and *Fukao* [31] proposed a MRAS based on the back-emf vector instead of the rotor

flux-linkage. This scheme provides an alternative solution without using a pure integration in the reference model, and hence has neither drift nor initial conditions problems. However, the reference model is still sensitive to stator resistance variations and may have stability problems at low stator frequency [12]. In addition, it shows low noise immunity due to stator current differentiation and poor dynamic performance at low stator frequency [41].

Another MRAS scheme based on reactive power has been developed by [31] offering robustness against stator resistance variation while avoiding pure integration. However, these two schemes exhibit an unstable nature within some operating conditions when passing through regenerating modes [12, 44, 45]. Furthermore, the back-emf and reactive power based schemes are difficult to design, and the back-emf and reactive power quantities vanish at low and zero speed [41].

2.3.2 The Problem of Pure Integration

The pure integration problem is associated with the rotor flux-linkage based MRAS and it is caused by the pure integration that is required by the reference model to calculates the rotor flux-linkage. The pure integration causes DC drift and initial condition problems in the reference model [3, 11, 46].

In rotor flux-linkage based MRAS, having some measure of low-pass filtering helps to attenuates the high-frequency components normally found in the motor terminal voltages which make it less attractive to completely eliminate the pure integrals[30]. To avoid these problems in practical implementations, a low-pass filter with the transfer function $1/(s+1/T)$ can be used instead of a pure integrator. However, since $1/(s+1/T) = (1/s).[s/(s+1/T)]$, thus in the practical system the reference model that contains $(1/s)$ is followed by a high-pass filter $[s/(s+1/T)]$.

Since the output of the modified reference model provides the modified rotor flux-linkages, the adaptive model must also be adjusted to give the corresponding modified values and therefore, the high-pass filter block $[s/(s+1/T)]$ is placed in front of the original adaptive model. The modified rotor flux-linkage based MRAS can be seen in figure 2.5. The modification of the rotor flux-linkage based MRAS has altered the mathematical structures of the reference and adaptive models while maintaining

hyperstability [30]. In practice, the cut-off frequency of the high-pass filter should be a few Hertz. Because below the cut-off frequency, the rotor speed estimation becomes inaccurate [3, 30].

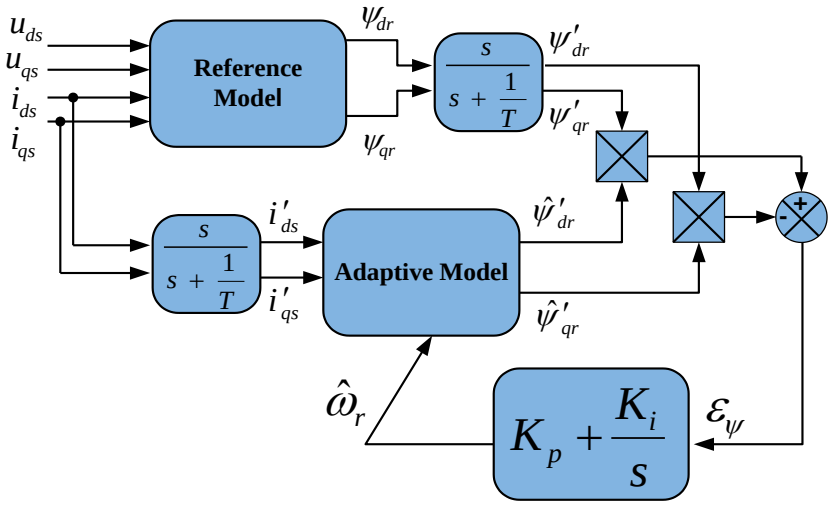

Figure 2. 5 Modified rotor flux-linkage based MRAS.

A number of more elaborate solutions have been proposed with the purpose of overcoming the pure integration problem. *Karanayil* [47] introduces a programmable cascaded low-pass filter to replace the pure integration by a cascaded filter with a small time constant to attenuate the DC offset decay time. *Hinkkanen et al* in [48] used another technique where the rotor flux-linkage is estimated by defining a modified integrator having the same frequency response as the pure integrator at steady state. *Qiang* [49] proposed a nonlinear feedback integrator for drift and DC offset compensation used for voltage model rotor flux-linkage estimator. This modified voltage model is incorporated into a rotor flux-linkage based MRAS structure as in [30] and the proposed scheme is tested when applied to a vector control induction motor drive.

Further research in [23, 46] has attempted to completely replace the voltage model by other rotor flux-linkage estimators, which may reduce the scheme's simplicity. Both schemes employ the same MRAS structure as in [30] based on the PI minimisation of the cross product of flux-linkage estimates. In [46], a state observer with current error feedback is used to generate the reference values for the rotor flux-linkage in the MRAS estimator. *Lascu et al* [23] developed a similar approach for classical direct torque

control and space vector modulation. In this modified MRAS based scheme, the reference model utilises a full order stator and rotor flux-linkage observer containing both voltage and current models, with an adaptive model based on the current model. Consequently, the speed observer uses the current model twice in the reference model, which is expressed in the rotor flux oriented reference frame, and in the adaptive model, which is expressed in the stator reference frame. Another modification to classical MRAS presented in [50], was applied by [51] using a closed-loop rotor flux-linkage observer which uses a coupling controller between the two flux-linkage estimates, voltage model and current model. Using the closed-loop topology provides the voltage model open loop integration with necessary feedback, and hence no low-pass filtering is required in the voltage model [52].

2.3.3 Variations of Motor Parameters

In essence, MRAS based speed estimators are comprised of two independent estimators that estimate the motor's state variables and these two estimators are based on the motor's mathematical model. The standard models consider the motor parameters as constants without taking into account the operational conditions; such as temperature, frequency and magnetic saturation. This means that any variation in the actual motor parameters will compromise the whole process of speed estimation. The main affected parameters are the stator and rotor resistance, which vary with temperature, and the stator and rotor leakage inductances, which vary with the operating current.

The stator resistance (R_s) has important effects on the stator flux-linkages, especially at low speeds where the stator voltages are small and therefore an accurate value of the stator resistance is required to have a satisfactory response. However, it is possible to have a rather accurate estimate of the appropriate 'hot' stator resistance by using a thermal model of the induction machine.

One of the first proposed solutions to overcome the problem associated with an inaccurate stator value was to use an MRAS based speed estimator, which does not have a stator resistance in its estimation process. This has led to the development of an MRAS that was based on reactive power. As previously mentioned in section 2.2.1.3, the scheme was developed by *Peng* and *Fukao* [31], who were also responsible for the development of the back-emf based MRAS. Additionally, the reactive power in the

MRAS based estimator is calculated from the cross product of back-emf and stator current vectors. The reference model does not contain stator resistance and is therefore independent of thermal resistive variations. The performance of this technique was experimentally verified for sensorless operation with good dynamic response. Initially this technique seemed to encompass a complete solution as it offers solution to the inherent problems associated with pure integration and also increases robustness against stator resistance mismatch. However, these quantities disappear at low or zero speed and give rise to highly nonlinear gains in the adaptive MRAS controller, where a poor result was achieved as reported by *Blasco-Gimenez* et al[20]. Furthermore, according to[31], the reactive power based estimator is robust against stator resistance and can achieve a wider bandwidth speed control. However, the motor actual speed might not converge to the speed command when the speed command is a step-down change [8]. This is because there is more than one steady state solution at any estimated speed, especially while passing through the regenerating mode. To solve this problem, *Kubota* et al [8] developed an algorithm based on reactive power with an extended *Kalman* filter to estimate the rotor flux-linkage and speed. Although this algorithm can be used in the regenerating mode, it is considered complicated to some extent.

In the reactive power based speed estimation scheme the stator resistance is eliminated from the reference model. However, the stator transient inductance is still present in the reference model. The accuracy of speed estimation is affected by variations of stator transient inductance. In order to eliminate the impact of the stator transient inductance on speed estimation and also eliminate the pure integration in the reference model, *Zhen* and *Xu* proposed a different method to improve the performance of the speed estimation in an MRAS based system. In their proposed method, the equations were derived to eliminate the stator transient inductance from the reference model. Considering that the stator resistance was still present, an online stator resistance identification scheme was applied to ensure that an accurate speed estimate can be obtained at all speeds[53].

More elaborate solutions have been proposed that incorporates online estimation of the stator resistance in the overall speed estimation scheme. The authors in [31] proposed an identification algorithm for the stator resistance using the q axis flux-linkage error in the identification process. While the authors in [21, 54] have developed an MRAS based algorithm for simultaneous stator resistance (R_s)and rotor speed (ω_r) estimation. The proposed scheme contain reference and an adaptive models and also includes two interchangeable adaptive mechanisms, one for (ω_r) estimation and the other for (R_s)

estimation. The purpose of this scheme is to compensate for the thermal variation of (R_s) in the speed reference model by a second adaptation mechanism. The proposed scheme offered superior performance and did not require steady state conditions.

Rashed and *Stronach* have incorporated a stator resistance estimator in back-emf based MRAS, where the robustness of stator resistance estimator for large resistance mismatches was verified via simulation and experimental work. The scheme was designed to be stable when both of the speed and the resistor estimators are used simultaneously in all operating modes of the drive [12].

A different technique was proposed by *Zhen* and *Xu* [53], where a mutual MRAS scheme with interchangeable reference and adaptive models was developed. This scheme was used for the rotor speed and stator resistance estimation in a position sensorless vector control of an induction motor (IM) drive. Although the system was still dependent on the stator resistance, the reference model is defined without using a pure integrator, as well as being free of stator leakage inductance. In this mutual scheme, the speed estimation stops briefly when the reference speed does not change and the estimated speed becomes stable. The two estimators then switch their functions to estimate the stator resistance, where the estimation is based on a separate adaptation mechanism. In order to achieve accurate rotor speed and stator resistance estimation, an online adaptation of the rotor time constant is incorporated. However, the two estimation algorithms are not concurrent and the drive has no speed information during stator resistance identification [21].

Blasco-Gimenez et al [55] have investigated different stator resistance tuning techniques based on the least squares circular regression algorithm (LSCRA), which is computationally intensive. In this method, the tuning was established by dividing the average value of the stator voltage and stator current acquired during a transient. This is the equivalent to a direct application of Ohm's law, since it has been proven that the average value of the stator current is not zero during transients through zero speed. The LSCRA method was proven to be very robust, and there are no extra signals to be injected into the machine, no speed measurements are required and no previous knowledge of any machine parameters is needed. However, the main drawback of the proposed method of (R_s) estimation is that it cannot be applied during steady state, since the average value of the stator currents and voltage will be zero.

Kubota et al [56] proposed simultaneous estimation of speed and rotor resistance. The speed was estimated using full-order state observers and the rotor resistance was estimated by injecting alternating current signals, superimposed on the field current demand. However, other machine parameters, namely the self inductance of the rotor and stator transient inductance that were both used in the state equation were assumed constant. Consequently, the scheme would endure performance degradation due to variation of these two parameters.

Blasco-Gimenez et al [55] after conducting a detailed study about the detuning of machine parameters, have also proposed solutions to compensate their effect on the accuracy of the speed estimate, where a scheme to tune rotor time constant was proposed. However, as pointed by *Kubota et al* [57] and *Yang et al* [58], it is theoretically impossible to simultaneously detect speed and rotor resistance using only measured stator quantities. To avoid this, *Blasco-Gimenez* used an additional measurement independent from the proposed speed estimation. Two speed estimations were executed simultaneously; one was MRAS based and the other was based on the rotor slot harmonics effect. The error between these two speed estimates was then used to drive the rotor resistance identifier. The acquired results were excellent and have verified the effectiveness of the proposed scheme.

2.3.4 Problems Associated with Stator Voltages Measurements

In MRAS based speed estimators, the measurement of the stator voltages is essential, which are then used in the reference model to estimate the state variables, such as rotor flux-linkages and back-emf. It is not necessary to monitor the stator voltages since they can be reconstructed by using the inverter switching functions and the monitored DC link voltage. For a more accurate measurement, a model for the voltage drops across the inverter switches should be included along with a thermal model that can be used to correct the value of stator resistance [3].

It is also possible to use appropriate voltage references instead of actual voltages if the switching frequency of the inverter is high compared to the electrical time constant of the motor. Such a solution has the additional advantage of further reducing the required number of sensors, and since no filtering of the voltages is required to eliminate the modulation noise, no delay is introduced due to filtering [3]. When the reconstructed stator voltages or reference voltages are used, some error compensation schemes must

be used in consideration for the following factors: voltage errors caused by the effects of dead-time insertion, voltage drop in the power electronic devices, and fluctuation of the DC link voltage.

Induction motors are normally driven using a voltage source inverter, which generates a series of rectangular pulses that continuously switch on and off to achieve a controllable variable voltage and frequency supply, meaning that the resultant stator voltage will contain high frequency harmonic components. Furthermore, non-ideal characteristics of switching devices, such as: non ideal voltage transition during switching the state of the switch on or off, unequal switching time, and dead-band insertion, can contribute to the nonlinear relation between voltage reference and inverter output.

There have been numerous attempts to improve the way the actual stator voltages are measured; one of which is employing a low-pass filter to remove high frequency components, leaving only the fundamental frequency. The drawback of this approach is that the low-pass filter will introduce lag or phase shift at the filtered output. From the control point of view, this is undesirable as it limits its dynamic performance of the system as noted by *Armstrong* [54] and *Xu et al* [59]. In addition to successful estimation, motor phase current that is already in a sinusoid shape will need to be filtered, or at least phase shifted, in order to impose the same delays and phase shifts between the two measurements. Another well known method that can support the voltage measurement process is synchronous integration, which is a nonlinear filtering method [60]. The synchronous integration technique is based on integrating the pulse width modulation (PWM) voltage signals, which are reset at the end of each PWM period. This provides the actual volts-seconds applied to the machine terminals over the PWM period. Using this technique should offer better measurements while including all of the inverter nonlinearities that can be caused by the dead-band insertion and non-ideal voltage transition while the power devices are switching on or off.

2.3.5 Proposed Improvements via the Incorporation of AI Schemes

A conventional MRAS based scheme contains a reference model and an adaptive model. The estimated rotor speed $(\hat{\omega}_r)$ is used as one of the input parameters to the adaptive model, which is the output of a suitable adaptation mechanism. Furthermore, as it was discussed in section 2.2.1, the adaptation mechanism of a conventional MRAS

based speed estimator is based on Popov's hyperstability criterion that will ultimately produced an adaptation mechanism in which the estimated state variables of the reference and adaptive models are manipulated into a speed tuning signal. This is in turn was then fed into a PI controller based adaptation mechanism.

The conventional approach also requires the use of a mathematical model for the adaptive model, where the digital implementation of such a scheme is considered relatively simple. Nevertheless, greater accuracy and robustness can be achieved if this mathematical model is not used but instead replaced with an AI based nonlinear adaptive model. It is then also possible to eliminate the need for a separate PI controller, since this can be integrated into the tuning mechanism of the AI based model.

The AI based model can take a variety of forms where it can be an ANN or a Fuzzy-neural network, etc. In addition, there is also the possibility of using different types of speed tuning signals. Furthermore, the adaptation-mechanism input signals can also take various forms, as in the non-AI based, conventional type of scheme discussed in section 2.2.1.

In view of the fact that there are different ANN configurations and a number of different types of speed tuning signal, then consequently, there are various possibilities for the speed tuning signals. However, the number of possibilities is even greater, since there are many types of ANNs and fuzzy-neural networks.

Based on the belief that the implementation of such AI based techniques may improve the performance of a system, many attempts have been made to achieve greater accuracy in an MRAS based speed estimator, and in turn, increase robustness against parameter variations, even at low stator frequency [3, 13].

2.3.5.1 Proposed Improvements via the incorporation of Fuzzy logic

Over the past two decades, there has been a significant increase in the use of fuzzy logic based controllers (FLCs) in both power systems and power electronic based applications. The use of FLCs is particularly advantageous because of its relative ease of implementation, due to the fact that they are not dependent on accurate mathematical models, which can be particularly useful in power system applications where large systems are difficult to model. Furthermore, fuzzy logic control has been found to be excellent in dealing with systems that are imprecise, nonlinear, or time-varying and with uncertain or unknown parameters and structure variations. In a fuzzy logic system, the

design can be based exclusively on linguistic information, available from experts, or by using clustered data [61, 62].

Initially, FLC techniques were implemented in various vector control based drives where the FLC was used to control the speed instead of a conventional PI controller. Most of the initial work was based on simulation. However, as early as 1995, *Vas* and *Stronach* have designed and applied a comprehensive vector controlled IM drives with multiple fuzzy based controllers to control the speed and currents.

The FLCs were used at first to estimate speed in sensorless drives containing an open-loop flux estimator. It was reported that the tuning effort required with the fuzzy controlled drive is significantly less than that required for the drive using conventional fixed gains PI controllers. There are also some improvements in transient profile of the system's response [3]. Subsequently, the FLCs were used in rotor flux-linkage speed sensorless drives that use an extended *Luenberger* observer. Reportedly, the acquired results have shown that FLCs offer high potential and significant reduction in the design effort. The concept of incorporating fuzzy logic into an ANN has been developed to enhance the adaptivity of fuzzy controllers by combining the principles of fuzzy logic and neural networks. In 1995, *Stronach* and *Vas* introduced an induction motor drive that employs a fuzzy-neural controller [63].

In 2006, *Lopez* et *al* [64] carried out an investigation on a novel speed sensorless drive for induction motors that was based on the combination of an Open Loop (OL) estimator and a steady state (SS) estimator. The novel drive structure was obtained by an intelligent combination of the open loop estimator response with the steady state response. Here, a fuzzy system applies weights to the two estimated speed values, according to the motor operating point, and averages both of the estimated speed values in order to obtain the best of both estimators. The OL estimator response is improved by means of a fuzzy based adaptive filtering to solve the problems of stator-voltage integration. The variable cut off frequency selected by a fuzzy logic depends on the operating conditions. During a transient, the FLC selects a high cut off frequency to decrease the effect of filter delay. In the steady state, where the delay effect is not important, lower values of cut off frequency are selected to eliminate the ripple of the estimated speed.

A rotor flux-linkage based MRAS with a fuzzy based adaptive model was presented in 2007 in [65]. The adaptive model was based on a self-tuning fuzzy identifier and the adaptive mechanism is based on the widely used back-propagation algorithm to minimise the difference between the output of motor's actual state variables and the output as predicted by the self-tuning fuzzy identifier. As a result, a precise estimate of the speed tracking can be obtained. The theoretical analysis and experimental results demonstrate that the self-tuning fuzzy identifier possesses a reasonably good tracking capability. It was also found that the proposed speed estimation scheme can accurately and rapidly identify the actual induction motor's speed [65]. In 2008**,** *Gadoue* [22] introduced a rotor flux-linkage based MRAS speed estimator where the adaptation mechanism was replaced with a fuzzy logic controller. A better transient performance was reported with an improved load torque disturbance rejection during both of the open and closed loop sensor less modes. In 2009, *Zerikat* [66] proposed a fuzzy neural network controller based adaptation mechanism for a rotor flux-linkage based MRAS speed estimator. The viability of this proposed structure was only verified by simulations.

2.3.5.2 Proposed Improvements via the incorporation of ANNs

An ANN, which is usually called a neural network (NN), is a mathematical model or computational model that aims to simulate the structure or functional aspects of biological neural networks. It consists of an interconnected group of artificial neurons and processes information using a connectionist approach to computation. In most cases an ANN is an adaptive system that changes its structure based on external or internal information that flows through the network during the learning phase. The basic idea behind NN assisted MRAS is to replace the adaptive model of conventional MRAS by an online trained NN as a state estimator. This strategy eliminates the need to use a mathematical adaptive model where the adaptation mechanism can also be integrated into the network tuning law [3]. However, since these proposed schemes have a similar structure to that proposed by [30], they would be affected by machine parameter variation and pure integration problems.

The above mentioned scheme was pioneered by *Ben-Brahim* [67, 68] and as far as the literature is concerned, the work carried out by *Ben-Brahim* is considered the first research related work that incorporates ANNs into an MRAS based IM drive. The specific implementation of this technique was discussed in detail by [62]. The neural

network was designed with a two-layer network based on the back-propagation technique with an unsupervised learning method. Rotor speed was chosen as the weight for the neural networks. The output of the neural network was driven to follow the desired output state by adjusting its weight using the back-propagation technique. It is apparent that this technique would be affected by the variations of motor parameters, particularly the stator resistance and problems associated with integration of voltage equation owing to the utilisation of integrating action that produces the desired output state.

A multi-layer neural network has been implemented by *Huang et al* [48] to estimate the speed where an off-line learning method was performed to train the neurons using data such as motor voltage and currents measured while running a standard drive. These sets of data were used to train the networks to adjust the weights prior to their use in the real-time control. The neural model was derived from standard stator and rotor voltage equations to obtain an explicit form of rotor speed in terms of voltage, currents and machine parameters. The work in [3] describes the speed estimation using this approach as an open-loop speed observer.

Kim et al [69] used multilayer neural networks with a hidden layer to estimate the speed of the rotor. The architecture of the neural networks was a recurrent network that uses a back-propagation technique to adjust the weight of the neurons. This recurrent configuration will increase robustness of the network against parameter variations and system noise. Here, two rotor flux-linkage observers based on voltage and current equations are used. The output of the two observers was used as an input signal for the neural networks. The error between the two observers was used to adjust the weights of the neurons and the output of the networks estimated the speed, which is then fed into the rotor flux observer. This scheme is very similar to the speed estimation system proposed by *Schauder* [30], except that the proportional and integral adaptation was replaced with neural network. Therefore, this scheme would exhibit similar performance degradation as in the model reference adaptive system, with respect to the parameters variation and the problems associated with the integration process. The subsequent addition of computing resources necessary for the neural network would further question whether such technique was justifiable. In contrast, the model reference adaptive system is known to be simple to implement without a high hardware specification.

Neural networks have also been combined with MRAS based systems for online stator and rotor resistance estimation for speed sensorless IM drives. In 2002, *Campbell* and *Sumner* [70] proposed an MRAS based sensorless IM drive using a recurrent NN to detect the thermal variations of the stator resistance at different operating conditions. This is performed based on machine current, estimated speed and an additional feed-back path representing the previous estimated values of the stator resistance. In this scheme, the motor speed is estimated based on rotor flux-linkage based MRAS. The training signals are generated from the real drive when the motor is running at different speeds with various load torques, such that the stator resistance variation can be obtained. A small DC voltage is used each time to measure the stator resistance when the machine is brought back to standstill. The training of the NN has been performed off-line using a back-propagation algorithm. The rotor resistance value is also updated assuming the same percentage change as the stator resistance. Operation at low and zero speed has been investigated by testing the proposed scheme for: load disturbance rejection at 100 rpm, deceleration to rest at rated load, and finally zero speed operation at rated load. An improved low speed operation was achieved when this NN open loop model is combined with the MRAS based speed estimator.

Karanayil et al [71] have developed an MRAS scheme based on a rotor flux-linkage where the variations of the stator and rotor resistances are tracked online. In this scheme the voltage model is used as a reference model, whereas a two layer NN mimics the adaptive current model as in [68]. To avoid pure integration in the reference model, a three stage programmable cascaded low-pass filter is used for the voltage model to synthesize the rotor flux-linkage. A back-propagation training algorithm was used online to adjust the NN weights that contain the rotor time constant information.

Two separate adaptive models were created to incorporate stator and rotor resistance estimation. In the first model, which is the stator resistance estimation, the error between the measured stator current and the estimated stator current using a neural network is back-propagated to adjust the weights of the neural network. In the second model, the error between the rotor flux-linkages based on a neural network model and a voltage model is back-propagated to adjust the weights of the neural network model for the rotor resistance estimation. Both the rotor and stator resistance variations were successfully estimated using the adaptation capabilities of neural networks. The implementation of these neural network techniques only requires a small increase of the

computation times. The feasibility and validity of the proposed identification has been established by the experimental results and satisfactory performance at low speed, which has also been reported.

Cirrincione et al [72] has developed an MRAS based speed estimator with a neural adaptive integrator in the reference model and a neural adaptive model. The scheme developed has incorporated an algorithm to compensate for inverter nonlinearity and also adopted the stator resistance online estimation technique developed by *Holtz* [11]. The neural adaptive integrator was originally developed by [73]. It was used to remove the initial value and drift problems associated with having a pure integrator in the reference model, which was discussed in section 2.1. The overall performance of the system was reported to have an improved accuracy in speed transients.

2.3.6 Harmonics & Noise in the Estimated Speed

According to the literature, the main issues that researchers have been concerned with revolve around the problem of establishing accurate speed estimation at low speed, improving the system's performance at the transient stage during the start-up of operation and load change. Numerous solutions have been tested and proposed, ranging from the development of back-emf based MRAS and reactive power based MRAS to replacing the constant adaptation mechanism with an AI based on either fuzzy logic or neural networks, or a combination of these both. Additional proposals include a variety of dynamic reference models to estimate the online induction motor parameters, such as the stator and the rotor resistance [22, 29, 74-77].

However, despite the wide range of research and proposed solutions in the area of sensorless speed estimation via means of model referencing, there has been a proclaimed issue that has received very little attention; this is the effect that the adaptation mechanism and PI controller have on the estimated speed in terms of introducing high-order harmonics, as the value of the PI controller gains, K_p and K_i, are increased. Only few researchers have acknowledged the fact that high PI gains in the adaptation mechanism have a noticeable effect on the estimated speed in a MRAS, which can be considered as negative. While higher PI gains help in achieving fast convergence, these gains can generate high-order harmonics and noise as their value increases. Even though the issue of high-order harmonics was highlighted in 2003, the

researchers that focused on developing advanced solutions failed to mention if their solution had solved the problem of harmonics or if their systems suffered any sort of side-effect from them.

As far as the literature review is concerned, the existence of the high-order harmonics phenomenon in relation to the generated noise and the estimated speed has been accepted by few researchers [28, 29] , and addressed by only one, *Kojabadi* [29]. This is the only published piece of research that is supposed to be dedicated to examining the effect of the PI controller on the generation of noise and high-order harmonics.

In [29], the effect of the adaptive PI controller gains on the speed estimation was investigated in the context of implementing an adaptive pseudoreduced-order flux observer (APFO) based MRAS, in which its design incorporates the estimation of the IM stator resistance.

The investigation was carried out by means of simulation and experiment and it was claimed that the acquired results demonstrated that with larger gains for the PI controller of the adaptation mechanism, the convergence for the speed estimation is fast. However, higher-order harmonics and noise are included in the estimated speed. This means that the selection of the adaptation mechanism gains is a compromise between achieving a fast response and a high robustness to noise with disturbances that affect the system.

On the one hand, the work published in [29] was dedicated to investigate the effect of the adaptive mechanism gains on the speed estimate. This work produced results that seem to cooperate with what has previously been acknowledged by other researchers. But on the other hand, there were no results presented that showed either an excessive noise generation or high-order harmonics in the estimated speed. Also, the influence of the generated and high-order harmonics was not mentioned in terms of being problematic or not.

Until now, have there been no studies that present a detailed account on how the PI gains of the adaptation mechanism can cause the estimated speed to exhibit high level of noise, but there have also been no studies that offer a thorough description on the property of the generated noise in the estimated speed, verifying the presence of high-order harmonics.

2.4 Summary

This chapter has presented an extensive overview of different model based techniques applied to speed sensorless IM drives, with most emphasis given to MRAS based strategies. Different problems affecting the low speed operation of MRAS observers have been pointed out. Various methods implemented in the literature to improve the rotor flux-linkage based schemes performance have been closely viewed.

As far as the literature review is concerned, most of the work published was dedicated to improving the performance of MRAS based speed estimators particularly at low speeds, as well as increasing the accuracy of the system by estimating the IM's parameters variations. However, as it has been pointed out, the issue of the generation of high-order harmonics and their effect on the estimated speed has not been dealt with. The research presented in this thesis will provide a thorough investigation into the so-called high-order harmonics phenomenon and will also establish whether any generated noise in the estimated speed bear a quantifiable effect on the overall speed control process.

Chapter 3 - MRAS Modelling for Speed Estimation

3.1 Induction Machine (d, q) Dynamic Model

Generally, high-performance drive controls, such as vector control is based on the (d, q) model of the machine. Therefore, a good understanding of the (d, q) model is essential to understand the vector control principle, which will be discussed in detail in appendix B.

The dynamic performance of an AC machine is rather complex because the three-phase rotor winding rotates in relation to the three phase stator windings as shown in figure 3.1. The machine model can be described by differential equations with a time-varying mutual inductance, but such a model tends to be very complex. A three phase machine can be represented by an equivalent two phase machine as shown in figure 3.2, where d^s and q^s correspond to the stator direct and quadrature axes, while $d^r$and q^r correspond to rotor direct and quadrature axes.

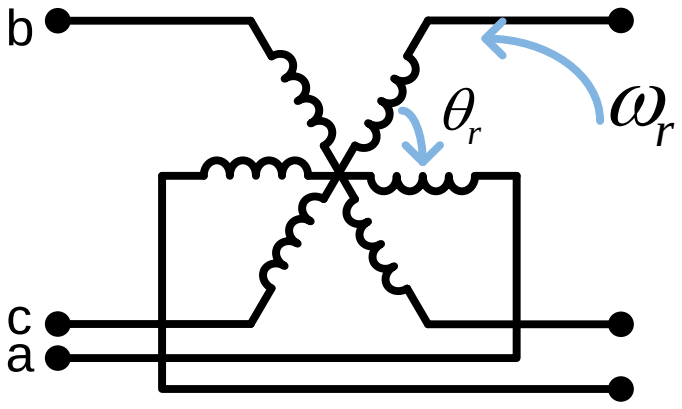

Figure 3. 1 Coupling effect in three-phase stator and rotor windings of motor.

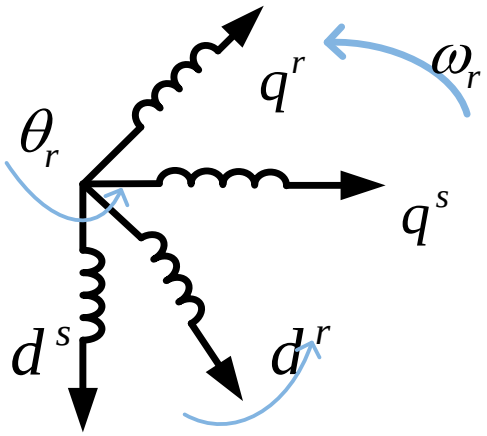

Figure 3. 2 Equivalent $d-q$ machine.

Although the time-varying parameters still remain in the equivalent two phase machine, they can be eliminated by transforming the stator variables to a synchronously rotating reference frame fixed in the rotor, [1, 13].

3.1.1 Axes Transformation

A symmetrical three-phase induction motor with stationary a_s, b_s and c_s axes at 120° angle apart is shown in figure 3.3. The goal is to transform the three-phase stationary reference frame a_s, b_s and c_s variable into two-phase stationary frame d^s and q^s variables.

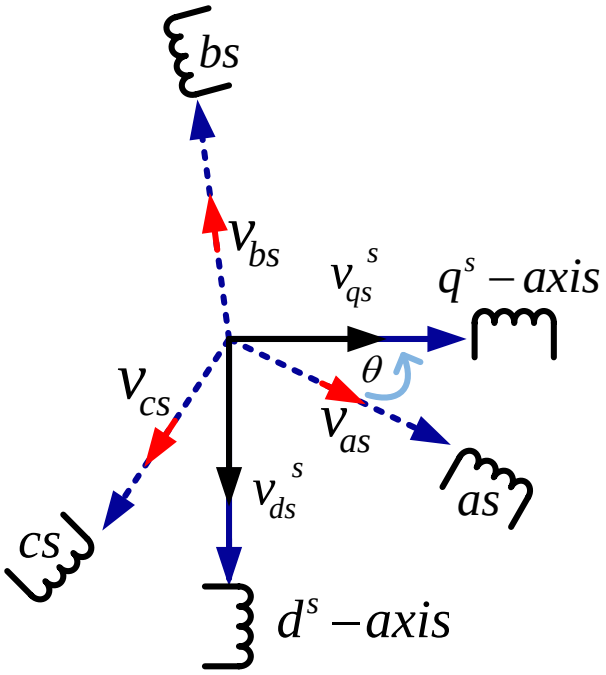

Figure 3. 3 Stationary reference frame (a, b, c) to (d_s, q_s) axes transformation.

Under the assumption that d^s and q^s are oriented at θ angle, as shown in figure 3.3, the voltages ${v_{ds}}^s$ and ${v_{qs}}^s$ can be resolved into a_s, b_s and c_s components and then represented in the matrix form as

$$\begin{bmatrix} v_{as} \\ v_{bs} \\ v_{cs} \end{bmatrix} = \begin{bmatrix} cos\theta & sin\theta & 1 \\ cos(\theta - 120^{\circ}) & sin(\theta - 120^{\circ}) & 1 \\ \cos(\theta + 120^{\circ}) & sin(\theta + 120^{\circ}) & 1 \end{bmatrix} . \begin{bmatrix} {v_{qs}}^s \\ {v_{ds}}^s \\ {v_{0s}}^s \end{bmatrix}. \tag{3.01}$$

The corresponding inverse relation is

$$\begin{bmatrix} {v_{qs}}^s \\ {v_{ds}}^s \\ {v_{0s}}^s \end{bmatrix} = \begin{bmatrix} cos\theta & cos(\theta - 120^{\circ}) & cos(\theta + 120^{\circ}) \\ sin\theta & sin(\theta - 120^{\circ}) & sin(\theta + 120^{\circ}) \\ 0.5 & 0.5 & 0.5 \end{bmatrix} . \begin{bmatrix} v_{as} \\ v_{bs} \\ v_{cs} \end{bmatrix} \tag{3.02}$$

where ${v_{0s}}^s$ is added as the zero sequence components, which may or may not be present. For convenience, θ is set to zero so that the q^s axis is aligned with the a_s axis. Ignoring the zero sequence components, the transformation relationship can be simplified as

$$v_{as} = {v_{qs}}^s, \tag{3.03}$$

$$v_{bs} = -\frac{1}{2}{v_{qs}}^s - \frac{\sqrt{3}}{2}{v_{ds}}^s, \tag{3.04}$$

$$v_{cs} = -\frac{1}{2}{v_{qs}}^s + \frac{\sqrt{3}}{2}{v_{ds}}^s, \tag{3.05}$$

and in reverse,

$${v_{qs}}^s = \frac{2}{3}v_{as} - \frac{1}{3}v_{bs} - \frac{1}{3}v_{cs} = v_{as} \tag{3.06}$$

and

$${v_{ds}}^s = \frac{1}{\sqrt{3}}v_{bs} - \frac{1}{\sqrt{3}}v_{cs}. \tag{3.07}$$

3.1.2 The Dynamic Model in a Stationary Reference Frame

Based on the Stanley derivations in the 1930s [13], the induction machine's dynamic model in the stationary reference frame can be represented as stator equations:

$${v_{ds}}^s = R_s i_{ds} + \frac{d{\psi_{ds}}^s}{dt} \tag{3.08}$$

and

$${v_{qs}}^s = \mathrm{R_s i_{qs}} + \frac{\mathrm{d}{\psi_{\mathrm{qs}}}^{\mathrm{s}}}{\mathrm{dt}}; \tag{3.09}$$

and rotor equations:

$$0 = R_r\, i_{qr}{}^s + \frac{d\psi_{qr}{}^s}{dt} - \omega_r \psi_{dr}{}^s, \tag{3.10}$$

and

$$0 = R_r\, i_{dr}{}^s + \frac{d\psi_{dr}{}^s}{dt} + \omega_r \psi_{qr}{}^s. \tag{3.11}$$

Consequently, as a result of the above equations, the (d^s, q^s) equivalent circuit in the stationary reference frame is shown in figures 3.4 (a) and (b).

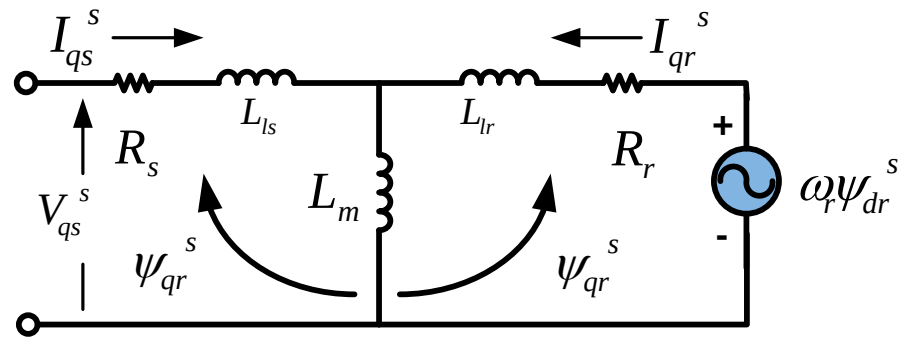

(a) *d* circuit.

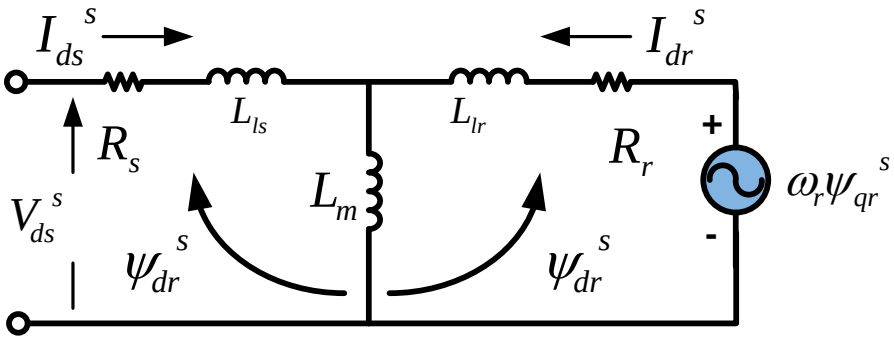

(a) *q* circuit.

Figure 3. 4 The (d^s, q^s) equivalent circuit in the stationary reference frame.

Finally, the torque equation can be expressed as

$$T_e = \frac{3}{2}\left(\frac{P}{2}\right)\left(\psi_{dr}{}^s\, i_{qr}{}^s - \psi_{qr}{}^s\, i_{dr}{}^s\right). \tag{3.12}$$

3.1.3 MRAS Based on Flux-Linkage Vector Estimation

A rotor flux-linkage based MRAS speed estimator is comprised of two independent flux estimators, where one is based on the voltage equations and the other is based on the current equations, for which the equations of both models are derived in the following sections.

3.1.3.1 Voltage Model

In this model, the machine terminal voltage and currents are sensed and the rotor flux is calculated from the stationary reference frame (d^s, q^s) equivalent circuit, as shown in figure 3.4. These equations are derived as

$$i_{qs}{}^{s} = \frac{2}{3} i_a - \frac{1}{3} i_b - \frac{1}{3} i_c = i_a, \tag{3.13}$$

$$i_{ds}{}^{s} = \frac{1}{\sqrt{3}} i_b - \frac{1}{\sqrt{3}} i_c \tag{3.14}$$

or

$$= -\frac{1}{\sqrt{3}} (i_a + 2i_b) \tag{3.15}$$

since $i_c = -(i_a + i_b)$, for isolated neutral load and

$$v_{qs}{}^{s} = \frac{2}{3} v_a - \frac{1}{3} v_b - \frac{1}{3} v_c, \tag{3.06}$$

or

$$= \frac{1}{3} (v_{ab} + v_{ac}), \tag{3.16}$$

$$v_{ds}{}^{s} = \frac{1}{\sqrt{3}} v_b - \frac{1}{\sqrt{3}} v_c, \tag{3.07}$$

or

$$= \frac{1}{\sqrt{3}} v_{bc}, \tag{3.17}$$

and

$$\psi_{\mathrm{ds}}{}^{\mathrm{s}} = \int (v_{ds}{}^{s} - R_s i_{ds}{}^{s}) dt, \tag{3.18}$$

$$\psi_{\mathrm{qs}}{}^{\mathrm{s}} = \int (\, v_{qs}{}^{s} - \; R_s i_{qs}{}^{s} \,) dt, \tag{3.19}$$

$$\hat{\psi}_s = \sqrt{\psi_{ds}{}^{s^2} + \psi_{qs}{}^{s^2}}, \tag{3.20}$$

$$\psi_{dm}{}^{s} = \psi_{ds}{}^{s} - L_{ls} i_{sd} \; = L_m (\, i_{ds}{}^{s} + \; i_{dr}{}^{s} \,), \tag{3.21}$$

$$\psi_{qm}{}^{s} = \psi_{qs}{}^{s} - \; L_{ls} i_{sq} = \; L_m (\, i_{qs}{}^{s} + \; i_{qr}{}^{s} \,), \tag{3.22}$$

$$\psi_{\mathrm{dr}}{}^{\mathrm{s}} = \mathrm{L_m} i_{ds}{}^{s} + \mathrm{L_r}\, \mathrm{i_{dr}}{}^{\mathrm{s}} \tag{3.23}$$

and

$$\psi_{\mathrm{qr}}{}^{\mathrm{s}} = \mathrm{L_m} i_{qs}{}^{s} + \mathrm{L_r}\, \mathrm{i_{qr}}{}^{\mathrm{s}}. \tag{3.24}$$

By the elimination of $\mathrm{i_{dr}}{}^{\mathrm{s}}$ and $\mathrm{i_{qr}}{}^{\mathrm{s}}$ from equations (3.23) & (3.24) and with the assistance of equations (3.21) and (3.22) respectively, provides

$$\psi_{dr}{}^{s} = \frac{L_r}{L_m} \psi_{dm}{}^{s} + L_{lr}\, i_{dr}{}^{s} \tag{3.25}$$

and

$$\psi_{qr}{}^{s} = \frac{L_r}{L_m} \psi_{qm}{}^{s} + L_{lr}\, i_{dr}{}^{s}. \tag{3.26}$$

This can also be written in the following form with the help of equations (3.21) and (3.22) as

$$\psi_{dr}{}^{s} = \frac{L_r}{L_m} (\psi_{ds}{}^{s} + \sigma L_s i_{ds}{}^{s}) \tag{3.27}$$

and

$$\psi_{qr}{}^{s} = \frac{L_r}{L_m} (\psi_{qs}{}^{s} + \sigma L_s i_{qs}{}^{s}) \tag{3.28}$$

where $\sigma = 1 - (\mathrm{L_m}^2 / \mathrm{L_r L_s})$.

After substituting $\psi_{\mathrm{ds}}{}^{\mathrm{s}}$ and $\psi_{\mathrm{ds}}{}^{\mathrm{s}}$ with their respective equivalents, the voltage model equations can be written as

$$\psi_{dr}{}^{s} = \frac{L_r}{L_m} \left(\int (v_{ds}{}^{s} - R_s i_{ds}{}^{s}) dt - \sigma L_s i_{ds}{}^{s} \right) \tag{3.29}$$

and

$$\psi_{qr}{}^{s} = \frac{L_r}{L_m} \left(\int (v_{qs}{}^{s} - R_s i_{qs}{}^{s}) dt - \sigma L_s i_{qs}{}^{s} \right). \tag{3.30}$$

Substituting equations (3.25) and (3.26) in the torque equation (3.12), in the stationary reference frame and simplifying, we get

$$T_e = \frac{3}{2}\left(\frac{P}{2}\right)\frac{L_m}{L_r}\left(\psi_{dr}{}^{s}\, i_{qr}{}^{s} - \psi_{qr}{}^{s}\, i_{dr}{}^{s}\right). \tag{3.31}$$

Figure 3.5 shows the block diagram of the flux-linkage estimator based on the derived voltage model.

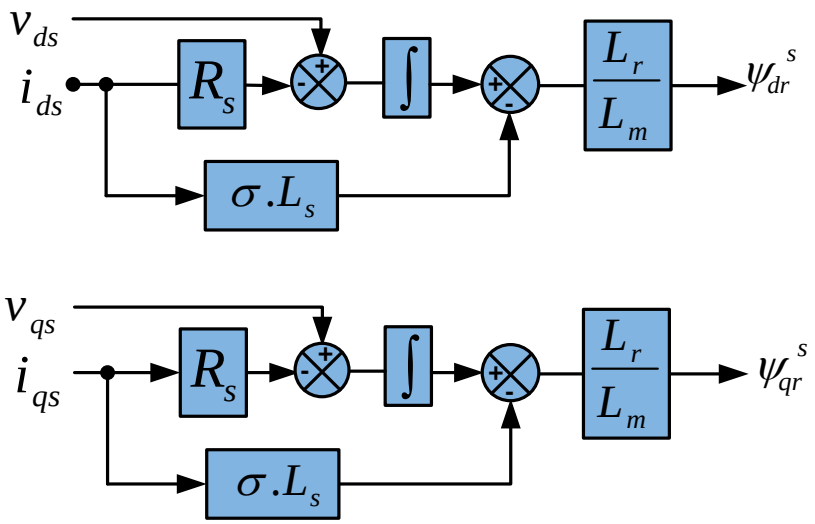

Figure 3. 5 Flux-linkage estimator based on IM's voltage model.

In conventional practice, the three-phase currents are filtered by a low-pass filter via an op-amp based circuit before being converted using an A/D converter. It is worth noting that machines are normally isolated neutral load, and therefore, only two current sensors are needed to calculate the two-phase equivalent of the measured three phase currents. Any errors in the unit vector or distortion associated with the feedback signals will affect the performance of the drive.

The method of direct vector control discussed so far is difficult to implement successfully the direct method of vector control discussed so far is difficult to implement successfully at very low frequencies, including at zero speed, because of the following problems:

- at low frequency, voltage signals ${v_{ds}}^s$ and ${v_{qs}}^s$ are very low. In addition, ideal integration becomes difficult because DC offset tends to build up at the integrator output
- the parameter variation effect of resistance R_s and inductance L_{ls}, L_{lr} and L_m tend to reduce the accuracy of estimated signals. In particular, the temperature variation of R_s becomes more dominant. However, compensation of R_s is somewhat easier, which will be discussed later. At high voltages, the effect of parameter variations is neglected.

In industrial applications, vector drives are often required to operate from zero speed, including zero speed start up. Here, direct vector control with voltage model cannot be used.

3.1.3.2 Current Model

In the low-speed region, the rotor flux components can be synthesized more easily with the help of speed and current signals. The rotor circuit equations of $(d^s,\ q^s)$ equivalent circuits shown in figures 3.4 (a) and (b) can be given as

$$0= R_r\ {i_{qr}}^s + \frac{d{\psi_{qr}}^s}{dt} - \omega_r {\psi_{dr}}^s \tag{3.32}$$

and

$$0= R_r\ {i_{dr}}^s + \frac{d{\psi_{dr}}^s}{dt} + \omega_r {\psi_{qr}}^s. \tag{3.33}$$

Adding the terms $\left(L_m\ {R_r}/{L_r}\right){i_{ds}}^s$ and $\left(L_m\ {R_r}/{L_r}\right){i_{qs}}^s$ on both sides of the above equations respectively, will produce

$$\frac{d{\psi_{dr}}^s}{dt} + \frac{R_r}{L_r}\left(L_m {i_{ds}}^s + L_r {i_{dr}}^s\right) - \omega_r {\psi_{qr}}^s = \frac{L_m R_r}{Lr} {i_{ds}}^s \tag{3.34}$$

and

$$\frac{d{\psi_{qr}}^s}{dt} + \frac{R_r}{L_r}\left(L_m {i_{qs}}^s + L_r {i_{qr}}^s\right) - \omega_r {\psi_{dr}}^s = \frac{L_m R_r}{Lr} {i_{qs}}^s. \tag{3.35}$$

Substituting equations (3.24) and (3.25) and simplifying, we get

$$\frac{d\psi_{dr}{}^{s}}{dt} = \frac{L_m}{T_r} i_{ds}{}^{s} - \omega_r \psi_{qr}{}^{s} - \frac{1}{T_r} \psi_{dr}{}^{s} \tag{3.36}$$

and

$$\frac{d\psi_{qr}{}^{s}}{dt} = \frac{L_m}{T_r} i_{qs}{}^{s} + \omega_r \psi_{dr}{}^{s} - \frac{1}{T_r} \psi_{qr}{}^{s}. \tag{3.37}$$

The circuit time constant is $T_r = {}^{L_r}/_{R_r}$, as shown in equations (3.36) and (3.37), which yield the rotor flux-linkages as functions of the stator currents and speed. Therefore, with knowledge of these signals, the rotor flux-linkage and the corresponding unit vector signals can be estimated. These equations are defined as the current model for rotor flux-linkage estimation, which was originally formulated by *Blaschke* [13] and often called the *Blachke* equation. It is shown in the block diagram form in figure 3.6, where the estimation of $\hat{\psi}_r$ is shown on the right. Flux-linkage estimation by this model requires a speed encoder, but the advantage is that the drive operation can be extended down to zero speed. However, it should be noted that the estimation accuracy is affected by the variation of machine parameters. In particular, the rotor resistance variation may be more than 50%, which becomes dominant by the temperature and skin effect. Compensation of this parameter is difficult because it is inaccessible.

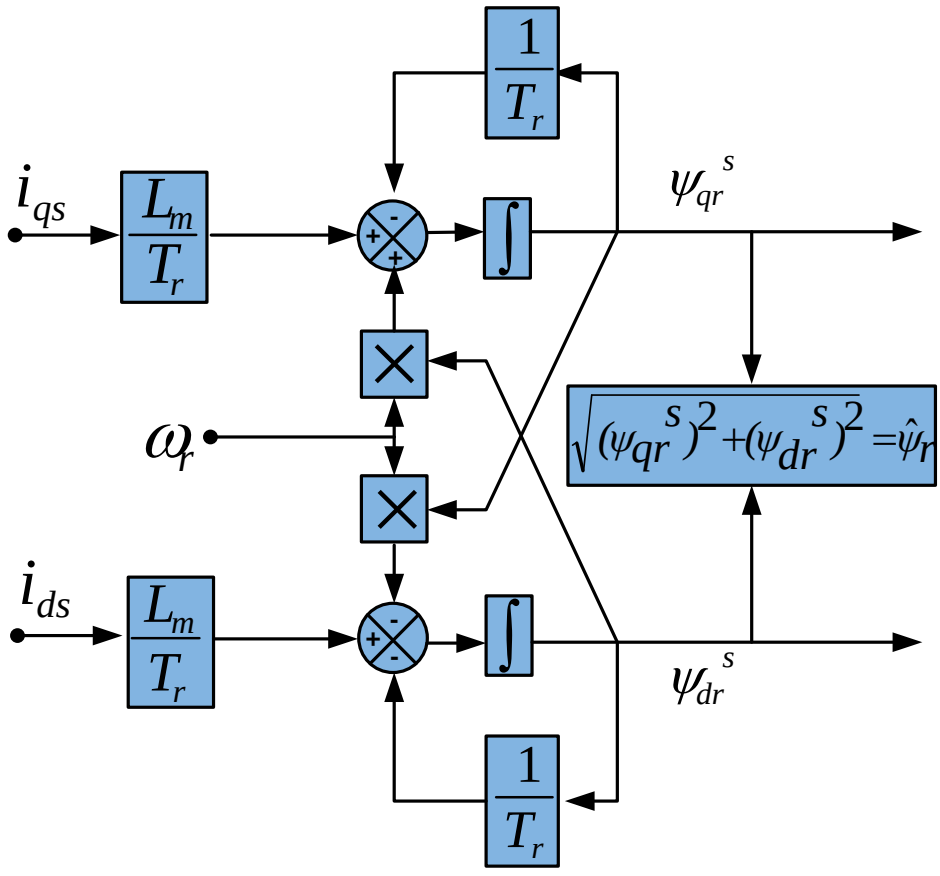

Figure 3. 6 Flux-linkage estimator based on IM's current model.

While the voltage model flux-linkage estimation is better at higher speed ranges, the current model estimation can be made at any speed. It is only logical to utilise both models simultaneously [3, 13, 78]. The voltage model becomes effective at higher speed ranges, but transitions smoothly to the current model at lower speed ranges.

The MRAS speed estimator will be based on estimating the rotor flux-linkage components $(\psi_{dr}{}^{s},\ \psi_{qr}{}^{s})$. As mentioned in the previous chapter, an MRAS based speed estimator is comprised of two models, a voltage model that represents the stator and a current model that represents the rotor.

3.1.3.3 Speed estimation and adaptation mechanism

In the rotor flux-linkage based MRAS, the state variables being estimated are the rotor flux-linkage components, namely $(\psi_{dr}{}^{s},\ \psi_{qr}{}^{s})$, which are calculated by reference model based on the motor's voltage model and $(\hat{\psi}_{dr}{}^{s},\hat{\psi}_{qr}{}^{s})$, which are calculated by the adaptive model based on the motor's current model. In an MRAS based estimator, the speed is calculated by calculating the difference between the state variables that were calculated by the reference model and the adaptive model, where the difference is essentially the error. This error is driven into an appropriate adaptation mechanism, which generates the estimated speed and in turn adjusts the adaptive model until the error is driven to zero. Figure 3.8 shows the block diagram of a rotor flux-linkage based MRAS speed estimator.

The appropriate adaptation mechanism can be derived by using Popov's criterion of hyperstability [3, 30]. This produces a stable and quick response system, where the differences between the state variables of the reference and adaptive models is manipulated into a speed tuning signal (ε), which then becomes an input for a PI type of controller, as shown in figure 3.7, which generates the estimated rotor speed.

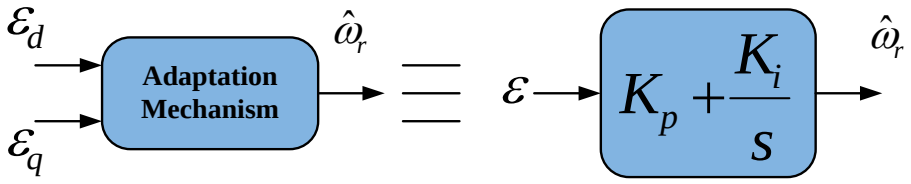

Figure 3. 7 Adaptation mechanism & speed tuning signal.

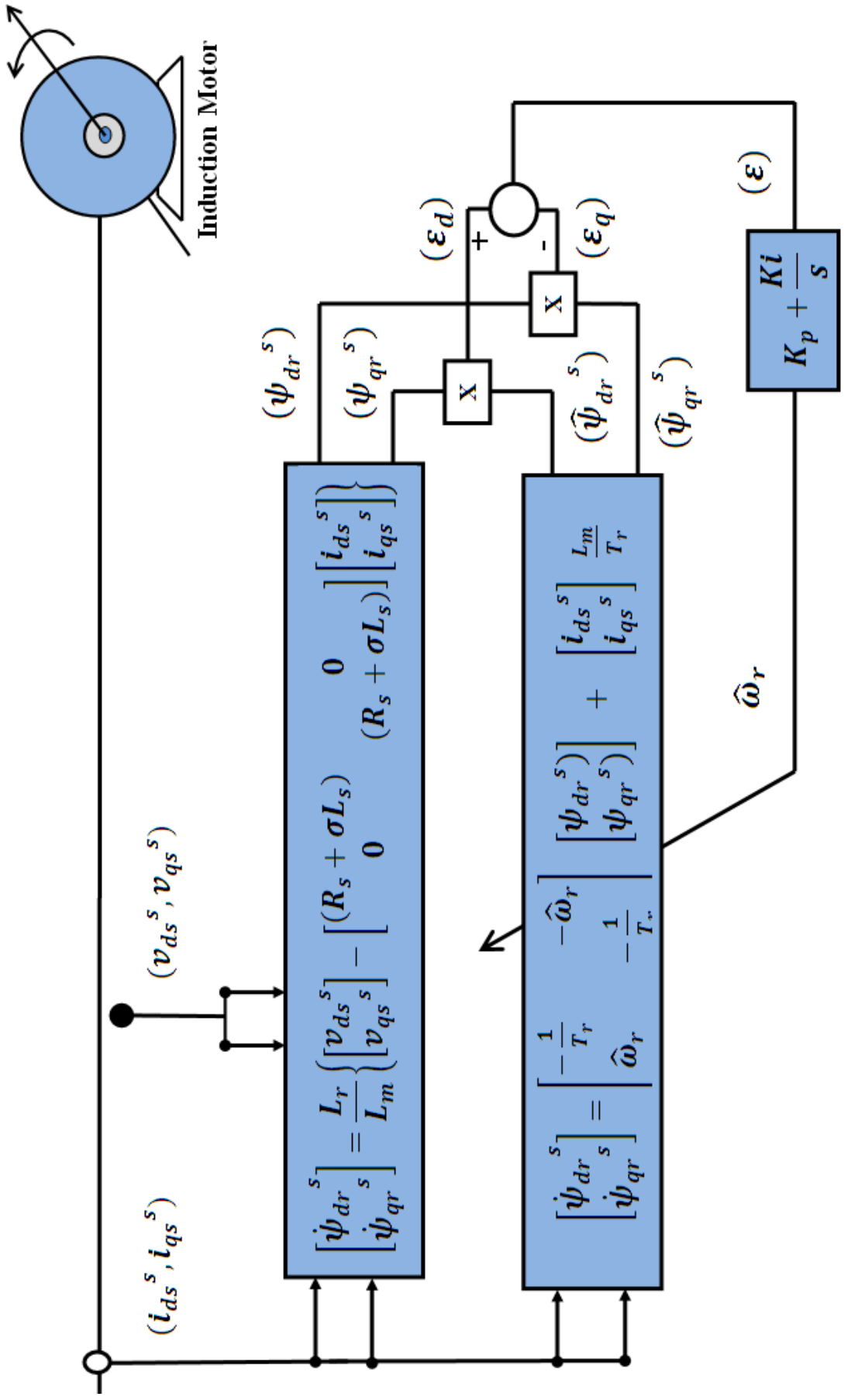

Figure 3. 8 Speed estimation by rotor flux-linkage based MRAS.

Detailed description of hyperstability theory is complex and is beyond the scope of this work. Hence, only a brief description will be given below for completion and prove why a PI controller is used as an adaptation mechanism. The particulars of the hyperstability theory can be found in *Landau* [38], where procedures of MRAS design using a hyperstability approach is illustrated. In general, a model reference adaptive speed estimator system can be represented by an equivalent nonlinear feedback system, comprising of a feed forward time-invariant linear subsystem and a feedback nonlinear time-varying subsystem. This is shown in figure 3.9.

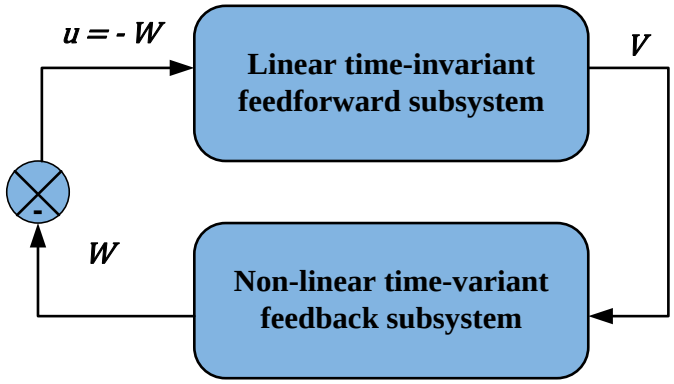

Figure 3. 9 Equivalent non-linear feedback system.

In figure 3.9, the input to the linear time-variant system is $\boldsymbol{u}$, which contains the stator voltages and currents. The output is $\boldsymbol{V}$, which is the tuning signal for the estimated speed. The generalized error, which is the output of the nonlinear time-variant system is $\boldsymbol{W}$, such that $\boldsymbol{u} = -\boldsymbol{W}$. The rotor speed estimation algorithm, which is the adaptation mechanism, is chosen according to Popov's hyperstability theory, whereby the transfer function matrix of the linear time-invariant subsystem must be strictly positive and real and the nonlinear time-varying feedback subsystem satisfies Popov's integral inequality, according to which $\int \boldsymbol{V^T W}\, \boldsymbol{dt} \geq \boldsymbol{0}$ in the time interval $[\boldsymbol{0}, \boldsymbol{t_1}]$ for all $\boldsymbol{t_1} \geq \boldsymbol{0}$. Thus, to obtain the adaptation mechanism, the transfer function $\boldsymbol{F}(s)$ of the linear time-invariant feed forward subsystem must first be obtained. It can be shown by lengthy calculation that in the scheme described below is strictly positive real [3, 30].

A possible proof uses the state variable form of the error equation, $\boldsymbol{dV/dt} = \boldsymbol{AV} - \boldsymbol{W}$, which is obtained by subtracting the state variable equations of the adjustable model from the state variable equations of the reference model. The equations of the adjustable rotor model are the rotor voltage equations in the stationary reference frame, which

were defined in equations (3.36) and (3.37) that are basically two-axis components. The reference stator model equations are the two-axis stator voltage equations in the stationary reference frame, which have been defined by equations (3.29) and (3.30).

In the resulting state variable form of the error equations, the state matrix is $\boldsymbol{A}$, where

$$\boldsymbol{A} = \begin{bmatrix} -\mathbf{1}/\boldsymbol{T_r} & -\boldsymbol{\omega_r} \\ \boldsymbol{\omega_r} & -\mathbf{1}/\boldsymbol{T_r} \end{bmatrix}.$$

The feed forward path transfer matrix of the linear time-invariant subsystem shown in figure 3.8 is $\boldsymbol{F}(s) = [s\boldsymbol{I} - \boldsymbol{A}]^{-1}$, where $\mathbf{I}$ is an identity matrix. It follows from the derivation of the error state equation that $\boldsymbol{W} = [\ \hat{\boldsymbol{\omega}}_{\boldsymbol{r}} - \boldsymbol{\omega_r}\ ]\left[\left(\hat{\boldsymbol{x}}_{\boldsymbol{q}},\ \hat{\boldsymbol{x}}_{\boldsymbol{d}}\right)\right]$, where $\left(\hat{\boldsymbol{x}}_{\boldsymbol{q}},\ \hat{\boldsymbol{x}}_{\boldsymbol{d}}\right)$ are the states estimated by the adaptive model. Therefore, when $\boldsymbol{W}$ is substituted into Popov's integral inequality $\int \boldsymbol{V^T W}\, \boldsymbol{dt} \geq \mathbf{0}$, it can be shown that this inequality can be satisfied by letting $\hat{\boldsymbol{\omega}}_{\boldsymbol{r}} = \left(\boldsymbol{K_p} + \boldsymbol{K_i}\ \frac{\mathbf{1}}{\boldsymbol{s}}\right)(\boldsymbol{\varepsilon})$. In this equation, $\frac{\mathbf{1}}{\boldsymbol{s}}$ represents an integrator and $(\boldsymbol{\varepsilon})$ is the appropriate speed tuning signal. In general, the state variables in the reference and adaptive models are $\left(\boldsymbol{x_q}, \boldsymbol{x_d}\right)$ and $\left(\hat{\boldsymbol{x}}_{\boldsymbol{q}}, \hat{\boldsymbol{x}}_{\boldsymbol{d}}\right)$, respectively and when these are used as replacements for the rotor flux-linkages $\left(\psi_{dr}{}^{s},\ \psi_{qr}{}^{s}\right)$ and $\left(\hat{\psi}_{dr}{}^{s},\ \hat{\psi}_{qr}{}^{s}\right)$, then the speed tuning signal becomes $\varepsilon_{\psi} = (\hat{\psi}_{dr}{}^{s}\ \psi_{qr}{}^{s} - \psi_{dr}{}^{s}\ \hat{\psi}_{qr}{}^{s})$. Therefore, if the state variables are the back-emf components, $\left(e_d{}^{s},\ e_q{}^{s}\right)$ and $\left(\hat{e}_d{}^{s},\ \hat{e}_q{}^{s}\right)$, then the speed tuning signal becomes $\varepsilon_e = (\hat{e}_d{}^{s}\ e_q{}^{s} - e_d{}^{s}\ \hat{e}_q{}^{s})$. It can be seen that when specified state variables are used on the outputs of the reference and adaptive models, then a corresponding speed tuning signal of that specific form is obtained by using Popov's integral inequality. It has been discussed above that when the rotor speed to be estimated is changed within the adaptive model, in such a way that the difference between the output of the reference model and the adaptive model is zero, then the estimated rotor speed is equal to the actual rotor speed. The error signal actuates the rotor-speed identification algorithm, which makes this error converge asymptotically to zero. The physical reason for the integrator in the PI controller is to ensure that the error converges asymptotically to zero [3, 30-32].

3.1.3.4 Discrete-time Representation

So far, all of the derived equations are represented in a continuous-time domain and since the experimental implementation of the MRAS based control algorithm is to be executed on a digital signal processor, a discrete-time representation is derived to facilitate such an implementation. The discrete-time equivalent of the flux-linkage based MRAS is acquired by transforming the differential equations from the continuous-time domain into the Laplace domain, which is a tool to map signals and systems behaviour from the continuous-time domain into the frequency domain. The resultant equation is then transformed into the z-domain utilising the Euler backward difference.

3.1.3.4.1 Discrete-time Voltage Model

The continuous-time representations of the voltage model equations are now transformed from the time-domain to Laplace by

$$\psi_{\mathrm{dr}}{}^{\mathrm{s}}(\mathrm{t}) = \frac{\mathrm{L_r}}{\mathrm{L_m}} \left(\int \left(v_{ds}{}^{s}(t) - R_s i_{ds}{}^{s}(t) \right) dt - \sigma \mathrm{L_s} \mathrm{i_{ds}}{}^{\mathrm{s}}(\mathrm{t}) \right) \tag{3.29}$$

and

$$\psi_{\mathrm{qr}}{}^{\mathrm{s}}(\mathrm{t}) = \frac{\mathrm{L_r}}{\mathrm{L_m}} \left(\int \left(v_{qs}{}^{s}(t) - R_s i_{qs}{}^{s}(t) \right) dt - \sigma \mathrm{L_s} \mathrm{i_{qs}}{}^{\mathrm{s}}(\mathrm{t}) \right). \tag{3.30}$$

Differentiating both side of the equations 3.29 and 3.30 will yield

$$\frac{\mathrm{d}\, \psi_{\mathrm{dr}}{}^{\mathrm{s}}(t)}{\mathrm{dt}} = \frac{\mathrm{L_r}}{\mathrm{L_m}} \left[v_{ds}{}^{s}(t) - R_s i_{ds}{}^{s}(t) - \sigma \mathrm{L_s} \frac{\mathrm{d}\, \mathrm{i_{ds}}{}^{\mathrm{s}}(t)}{\mathrm{dt}} \right] \tag{3.38}$$

and

$$\frac{\mathrm{d}\, \psi_{\mathrm{qr}}{}^{\mathrm{s}}(t)}{\mathrm{dt}} = \frac{\mathrm{L_r}}{\mathrm{L_m}} \left[v_{qs}{}^{s}(t) - R_s i_{qs}{}^{s}(t) - \sigma \mathrm{L_s} \frac{\mathrm{d}\, \mathrm{i_{qs}}{}^{\mathrm{s}}(t)}{\mathrm{dt}} \right]. \tag{3.39}$$

In order to acquire the Laplace representation of the differential equation, all of the $^{\mathrm{d}}/_{\mathrm{dt}}$ operators must be replaced with s, producing

$$\mathrm{s}\, \psi_{\mathrm{dr}}{}^{\mathrm{s}}(s) = \frac{\mathrm{L_r}}{\mathrm{L_m}} \left[v_{ds}{}^{s}(s) - R_s i_{ds}{}^{s}(s) - \sigma \mathrm{L_s} \left(\mathrm{s}\, \mathrm{i_{ds}}{}^{\mathrm{s}}(s) \right) \right] \tag{3.40}$$

and

$$\mathrm{s}\, \psi_{\mathrm{qr}}{}^{\mathrm{s}}(s) = \frac{\mathrm{L_r}}{\mathrm{L_m}} \left[v_{qs}{}^{s}(s) - R_s i_{qs}{}^{s}(s) - \sigma \mathrm{L_s} \left(\mathrm{s}\, \mathrm{i_{qs}}{}^{\mathrm{s}}(s) \right) \right]. \tag{3.41}$$

By applying the Euler backward difference approximation $s = \frac{1-z^{-1}}{T_s}$, then

$$\left[\frac{1-z^{-1}}{T_s}\right].\psi_{\mathrm{dr}}{}^{\mathrm{s}}[\mathrm{k}] = \frac{\mathrm{L_r}}{\mathrm{L_m}}\left[v_{ds}{}^{s}[k] - R_s i_{ds}{}^{s}[k] - \sigma \mathrm{L_s}\left[\frac{1-z^{-1}}{T_s}\right].\mathrm{i}_{\mathrm{ds}}{}^{\mathrm{s}}[\mathrm{k}])\right], \quad (3.42)$$

$$\frac{\psi_{\mathrm{dr}}{}^{\mathrm{s}}[\mathrm{k}]-\psi_{\mathrm{dr}}{}^{\mathrm{s}}[\mathrm{k-1}]}{\mathrm{T_s}} = \frac{\mathrm{L_r}}{\mathrm{L_m}}\left[v_{ds}{}^{s}[k] - R_s i_{ds}{}^{s}[k] - \sigma \mathrm{L_s}\left(\frac{\mathrm{i_{ds}}{}^{\mathrm{s}}[\mathrm{k}]-\mathrm{i_{ds}}{}^{\mathrm{s}}[\mathrm{k-1}]}{\mathrm{T_s}}\right)\right], \quad (3.43)$$

$$\psi_{\mathrm{dr}}{}^{\mathrm{s}}[\mathrm{k}] = \psi_{\mathrm{dr}}{}^{\mathrm{s}}[\mathrm{k}-1] + \frac{\mathrm{L_r}}{\mathrm{L_m}}\left[\left(v_{ds}{}^{s}[k] - R_s i_{ds}{}^{s}[k]\right).Ts - \sigma \mathrm{L_s}\left(\mathrm{i_{ds}}{}^{\mathrm{s}}[\mathrm{k}] - \mathrm{i_{ds}}{}^{\mathrm{s}}[\mathrm{k}-1]\right)\right]$$

$$\left[\frac{1-z^{-1}}{T_s}\right].\psi_{\mathrm{qr}}{}^{\mathrm{s}}[\mathrm{k}] = \frac{\mathrm{L_r}}{\mathrm{L_m}}\left[v_{qs}{}^{s}[k] - R_s i_{qs}{}^{s}[k] - \sigma \mathrm{L_s}\left[\frac{1-z^{-1}}{T_s}\right].\mathrm{i}_{\mathrm{qs}}{}^{\mathrm{s}}[\mathrm{k}])\right] \quad (3.45)$$

and

$$\frac{\psi_{\mathrm{qr}}{}^{\mathrm{s}}[\mathrm{k}]-\psi_{\mathrm{qr}}{}^{\mathrm{s}}[\mathrm{k-1}]}{\mathrm{T_s}} = \frac{\mathrm{L_r}}{\mathrm{L_m}}\left[v_{qs}{}^{s}[k] - R_s i_{qs}{}^{s}[k] - \sigma \mathrm{L_s}\left(\frac{\mathrm{i_{qs}}{}^{\mathrm{s}}[\mathrm{k}]-\mathrm{i_{qs}}{}^{\mathrm{s}}[\mathrm{k-1}]}{\mathrm{T_s}}\right)\right] \quad (3.46)$$

$$\psi_{\mathrm{qr}}{}^{\mathrm{s}}[\mathrm{k}] = \psi_{\mathrm{qr}}{}^{\mathrm{s}}[\mathrm{k}-1] + \frac{\mathrm{L_r}}{\mathrm{L_m}}\left[\left(v_{qs}{}^{s}[k] - R_s i_{qs}{}^{s}[k]\right).Ts - \sigma \mathrm{L_s}\left(\mathrm{i_{qs}}{}^{\mathrm{s}}[\mathrm{k}] - \mathrm{i_{qs}}{}^{\mathrm{s}}[\mathrm{k}-1]\right)\right]$$

3.1.3.4.2 Discrete-time Current Model

The continuous-time representations of the current model equations are now transformed from the time-domain to Laplace by

$$\frac{\mathrm{d}\psi_{\mathrm{dr}}{}^{\mathrm{s}}(t)}{\mathrm{dt}} = \frac{\mathrm{L_m}}{\mathrm{T_r}}\mathrm{i_{ds}}{}^{\mathrm{s}}(t) - \omega_{\mathrm{r}}(t)\psi_{\mathrm{qr}}{}^{\mathrm{s}}(t) - \frac{1}{\mathrm{T_r}}\psi_{\mathrm{dr}}{}^{\mathrm{s}}(t) \quad (3.36)$$

and

$$\frac{\mathrm{d}\psi_{\mathrm{qr}}{}^{\mathrm{s}}(t)}{\mathrm{dt}} = \frac{\mathrm{L_m}}{\mathrm{T_r}}\mathrm{i_{qs}}{}^{\mathrm{s}}(t) + \omega_{\mathrm{r}}(t)\psi_{\mathrm{dr}}{}^{\mathrm{s}}(t) - \frac{1}{\mathrm{T_r}}\psi_{\mathrm{qr}}{}^{\mathrm{s}}(t). \quad (3.37)$$

In order to acquire the Laplace representation of the differential equation, all of the d/dt operators must be replaced with s, producing

$$\mathrm{s}\,\psi_{\mathrm{dr}}{}^{\mathrm{s}}(s) = \frac{\mathrm{L_m}}{\mathrm{T_r}}\mathrm{i_{ds}}{}^{\mathrm{s}}(s) - \omega_{\mathrm{r}}\psi_{\mathrm{qr}}{}^{\mathrm{s}}(s) - \frac{1}{\mathrm{T_r}}\psi_{\mathrm{dr}}{}^{\mathrm{s}}(s) \quad (3.47)$$

and

$$\mathrm{s}\,\psi_{\mathrm{qr}}{}^{\mathrm{s}}(s) = \frac{\mathrm{L_m}}{\mathrm{T_r}}\mathrm{i_{qs}}{}^{\mathrm{s}}(s) + \omega_{\mathrm{r}}\psi_{\mathrm{dr}}{}^{\mathrm{s}}(s) - \frac{1}{\mathrm{T_r}}\psi_{\mathrm{qr}}{}^{\mathrm{s}}(s). \quad (3.48)$$

By applying the Euler backward difference approximation $s = \frac{1-z^{-1}}{T_s}$, then

$$\left[\frac{1-z^{-1}}{T_s}\right].\ \psi_{dr}{}^{s} = \frac{L_m}{T_r} i_{ds}{}^{s} - \omega_r \psi_{qr}{}^{s} - \frac{1}{T_r}\psi_{dr}{}^{s}, \tag{3.49}$$

$$\frac{\psi_{dr}{}^{s}[k]-\psi_{dr}{}^{s}[k-1]}{T_s} = \frac{L_m}{T_r} i_{ds}{}^{s} - \omega_r \psi_{qr}{}^{s} - \frac{1}{T_r}\psi_{dr}{}^{s}, \tag{3.50}$$

$$\psi_{dr}{}^{s}[k]\left[1+\frac{T_s}{T_r}\right] = \psi_{dr}{}^{s}[k-1] + \frac{L_m T_s}{T_r} i_{ds}{}^{s}[k] - T_s \omega_r \psi_{qr}{}^{s}[k], \tag{3.51}$$

$$\psi_{dr}{}^{s}[k] = \frac{1}{1+{}^{T_s}/_{T_r}}\left[\psi_{dr}{}^{s}[k-1] + \frac{L_m T_s}{T_r} i_{ds}{}^{s}[k] - T_s \omega_r \psi_{qr}{}^{s}[k]\right], \tag{3.52}$$

$$s\,\psi_{qr}{}^{s}(s) = \frac{L_m}{T_r} i_{qs}{}^{s}(s) + \omega_r(s)\psi_{dr}{}^{s}(s) - \frac{1}{T_r}\psi_{qr}{}^{s}(s), \tag{3.53}$$

$$\left[\frac{1-z^{-1}}{T_s}\right].\ \psi_{qr}{}^{s} = \frac{L_m}{T_r} i_{qs}{}^{s} - \omega_r \psi_{dr}{}^{s} - \frac{1}{T_r}\psi_{qr}{}^{s}, \tag{3.54}$$

$$\frac{\psi_{qr}{}^{s}[k]-\psi_{qr}{}^{s}[k-1]}{T_s} = \frac{L_m}{T_r} i_{qs}{}^{s} - \omega_r \psi_{dr}{}^{s} - \frac{1}{T_r}\psi_{qr}{}^{s} \tag{3.55}$$

$$\psi_{qr}{}^{s}[k]\left[1+\frac{T_s}{T_r}\right] = \psi_{qr}{}^{s}[k-1] + T_s\left(\frac{L_m}{T_r} i_{qs}{}^{s}[k]\right) - T_s(\omega_r \psi_{dr}{}^{s}[k]), \tag{3.56}$$

and

$$\psi_{qr}{}^{s}[k] = \frac{1}{1+{}^{T_s}/_{T_r}}\left[\psi_{qr}{}^{s}[k-1] + T_s\left(\frac{L_m}{T_r} i_{qs}{}^{s}[k]\right) - T_s(\omega_r \psi_{dr}{}^{s}[k])\right]. \tag{3.57}$$

3.4.3 Discrete-time PI Controller

The continuous-time PI controller representation is now transformed from the time-domain to Laplace by

$$\omega_r(t) = K_p.\,\varepsilon_\psi(t) + K_i \int \varepsilon_\psi(t)\,dt$$

In order to acquire the Laplace representation of the differential equation, all of the ${}^{d}/_{dt}$ operators must be replaced with s, producing

$$\omega_r(s) = K_p.\,\varepsilon_\psi(s) + \frac{K_i}{s}.\,\varepsilon_\psi(s) \tag{3.58}$$

By applying the Euler backward difference approximation $s = \frac{1-z^{-1}}{T_s}$, then

$$\omega_r[k] = P_{output}[k] + I_{output}[k], \tag{3.59}$$

$$P_{output}[k] = K_p\,(\varepsilon_\psi[k])$$

and

$$I_{output}[k] = K_i\,T_s\big(\varepsilon_\psi[k]\big) + I_{output}[k-1].$$

3.2 Summary

This chapter presented all the necessary steps required to model a rotor flux-linkage based MRAS for sensorless speed estimation. First, the three-phase variables were transformed into (d, q) variables in the stationary reference frame. Secondly, the dynamic model of the induction machine was derived by implementing the (d, q) transformation. Furthermore, this chapter has not only illustrated how the rotor flux-linkage based MRAS is derived based on the rotor flux-linkage vector estimation, but has also explained how the adaptation mechanism was discussed according to Popov's hyperstability criterion.

The modelled rotor flux-linkage MRAS will be implemented in real time, where it will be written in C language and then compiled to an executable format to be installed onto the digital signal processor. The first role of the MRAS is to establish the field orientation utilising the rotor flux-angle, which is calculated using the rotor flux-linkage components. The second role is to estimate the rotor speed to be used via a speed feedback signal.

Chapter 4 - Simulation and Preliminary Results

4.1 Introduction.

The speed estimation scheme that is under investigation is established on the implementation of a rotor flux-linkage based MRAS within a direct field-oriented control (FOC) of an induction motor drive. Figure 4.1 shows the overall diagram of the sensorless control scheme.

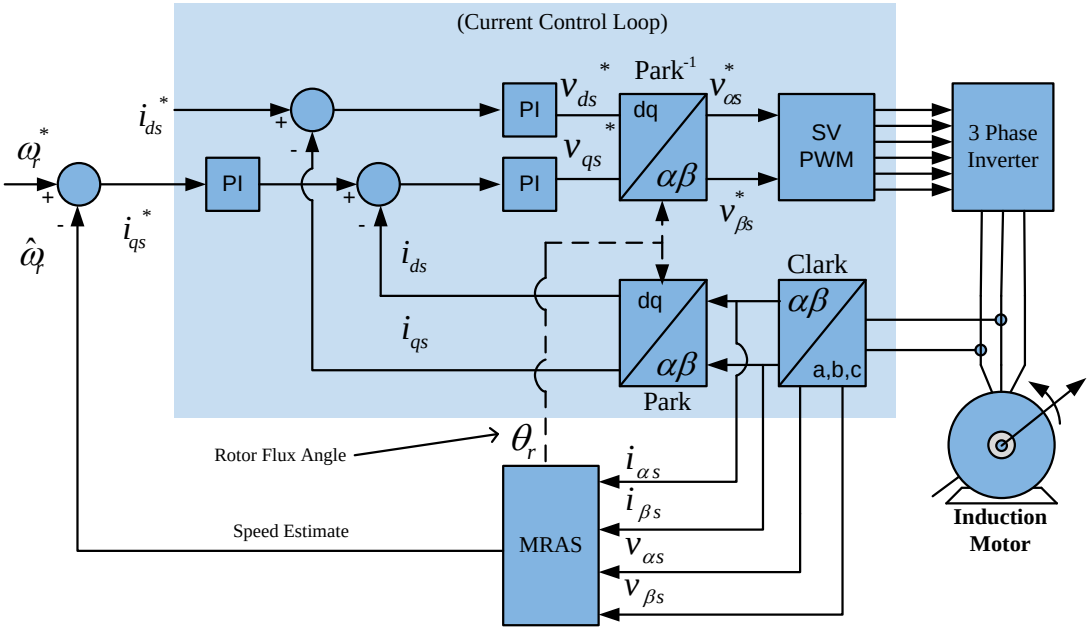

Figure 4. 1 Sensorless field-oriented control induction motor drive.

The simulation is accomplished by implementing Matlab® R2008a Simulink® tools, Version 7.6.0.324, where both the induction machine and the MRAS based estimator are mathematically derived as a dynamic (d, q) model in the stationary reference frame.

As explained in chapter 3, the rotor flux-linkage MRAS calculates the rotor's flux-components from the measured terminal voltages and currents in order to generate a speed estimate as well as the rotor flux-angle, which is essential to establish field orientation. The induction motor is fed by a PWM voltage source inverter and the inverter's switching sequence is controlled via space vector modulation (SVM) while

the duty ratio is controlled by the stator reference voltages $(V_{as}{}^{*})$ and $(V_{\beta s}{}^{*})$, which are generated from the Park inverse transformation.

The field orientation scheme is explained in detail within appendix A. In this scheme, the main purpose of the rotor flux-angle is to assist in establishing the field orientation by transforming the time-varying stator quantities into a fixed synchronously rotating reference frame.

The fundamental idea of field oriented control for AC motors, such as induction or synchronous motors, is to align the rotor flux axis into the synchronously rotating d −axis. The important result of this alignment is that the electromagnetic flux and torque produced by the motor, which can be independently controlled by the d −axis and q −axis stator current in the synchronously rotating reference frame, respectively. [3, 13, 35]

As seen in figure 4.1, the torque-producing stator current is (i_{qs}), while the rotor flux-producing stator current is (i_{ds}), because the produced torque is generated by cross product between the stator current and the rotor flux. The rotor flux angle θ_r is required to convert the (d, q) two-phase orthogonal stationary system into the rotating reference frame and vice versa. The rotor flux angle θ_r is calculated by the inverse tangent of the ratio of the rotor flux-linkage in the stationary reference frame with superscript "s". It should be noted that the rotor fluxes shown are already referred to the stator side.

The rotor flux angle is calculated using $\theta_r = tan^{-1}\ (\hat{\psi}_{qr}{}^{s} / \hat{\psi}_{dr}{}^{s})$.

In essence, the FOC scheme consists of two control loops, a current control loop and a speed control loop. The task of the speed control loop is to drive the difference between the reference speed, (ω_r^*) and the estimated speed $(\hat{\omega}_r)$ to zero. This is achieved by feeding the difference, the speed error, to a PI controller that will derive the correction torque producing current $(i_{qs}{}^{*})$, which is treated a torque reference current. Similarly to the speed control loop, the current control loop regulates both the flux and torque currents (i_{ds}) and (i_{qs}) where the regulation is established using two PI controllers. The output of the PI controllers forms the stator reference voltages $(v_{ds}{}^{*})$ and $(v_{qs}{}^{*})$. Subsequently, $(v_d{}^{*})$ and $(v_{qs}{}^{*})$ are transformed via $Park^{-1}$ (see figure 4.1) to the time-varying stator quantities $(v_\alpha{}^{*})$ and $(v_{\beta s}{}^{*})$ in order to be utilised by the SVM to generate the appropriate switching sequence.

The feedback currents are measured as three-phase currents ia_s, ib_s and ic_s from the motor terminals and then transformed via the *Clarke and Park* transformations to $(i_{\alpha s}, i_{\beta s})$ and (i_{ds}, i_{qs}) respectively, to be compared to $(\ {i_{ds}}^*, {i_{qs}}^*)$.

The terminal three phase voltages va, vb and vc are also measured at the motor terminals and transformed by a *Clarke* transformation to $(v_{\alpha s}, v_{\beta s})$. They are then fed to the rotor flux-linkage based MRAS along with (i_{ds}, i_{qs}) to be used in the speed estimation algorithm as inputs. The MRAS model will calculate the rotor flux-linkage components $({\psi_{dr}}^s,\ {\psi_{dr}}^s)$ and $({\hat{\psi}_{qr}}^s, {\hat{\psi}_{qr}}^s)$, which are sequentially are fed to the PI based adaptation mechanism in order to produce the estimated speed $(\hat{\omega}_r)$.

4.2 Simulation Preliminary Results

With regards to testing the effect of the adaptive PI gains on the estimated speed in terms of introducing high-order harmonics and noise, some initial results have been acquired. The results aim to show the effect of the adaptation mechanism, the PI controller, has on the estimated speed in relation to the generation of noise and harmonics. A range of PI gains have been tested on the simulated drive system where the estimated speed has been monitored and the overall performance of the system observed. The test was carried out by subjecting the motor to a step input of 20 RPM. Generally, the estimated and measured speeds will track each other during transient and steady states. Figures 4.2 to 4.4 show both of the actual and estimated speed for a range of PI gains of the speed estimation scheme.

4.2.1 The Effect of the Adaptation Mechanism Gains on the Speed Estimate under No-load Operations

The first test is carried out while applying an adaptation mechanism with low PI gains, where K_p was set to 40 and K_i was set to 400. As it can be seen from Figure 4.2, the low gains will cause the estimated speed to oscillate for approximately 0.14 seconds before a full convergence is achieved. The settling time, ts, for the estimated and the measured speed are 0.11 seconds and 0.12 seconds, respectively. Moreover, the low PI gains cause the measured speed to overshoot considerably beyond the desired reference speed. The percentage peak overshoot (PO) of the measured speed is 74.53%.

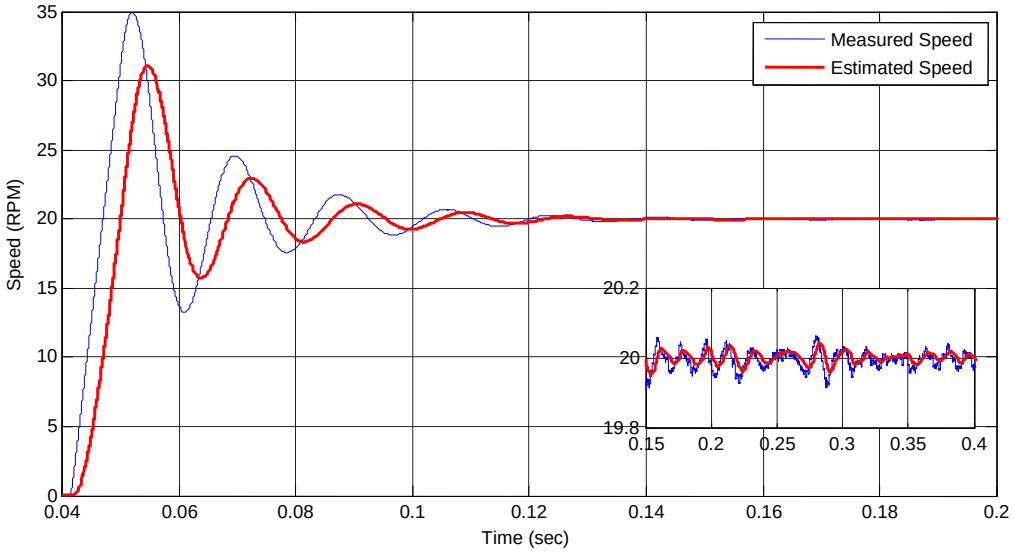

Figure 4. 2 Estimated and actual speed under no-load conditions, adaptation mechanism gains set as K_p= 40 and K_i =400.

To further evaluate the effect of the adaptation gains, a second test was carried out by increasing the value of K_p to 60 and the value of K_i to 600. It was observed in figure 4.3 that the estimated speed had exhibited fewer oscillations and the settling time of the measured speed had dropped by 41.46%. Moreover, the PO of the measured speed had decrease from 74.53% to 51.80%.

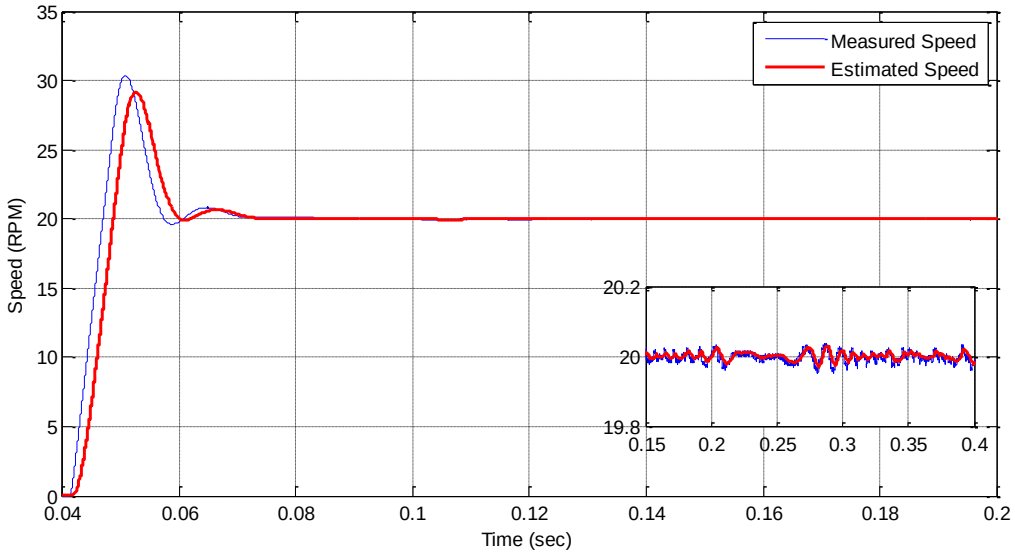

Figure 4. 3 Estimated and actual speed under no-load conditions, adaptation mechanism gains set as K_p= 60 and K_i =600.

Figure 4.4 shows how the simulated sensorless drive system responded when the PI gains of the adaptation mechanism are increased further to values of 100 for K_p and 1000 for K_i. It can be seen that there is a noticeable reduction of both the oscillations and the level of overshoot, as well as achieving a faster speed convergence. To show this fast convergence, the measured speed settling time has dropped by an indicated 3.53% and similarly, the estimated speed settling time has dropped by an indicated 4.45%. Also, the PO has dropped from 51.80% to 41.27%.

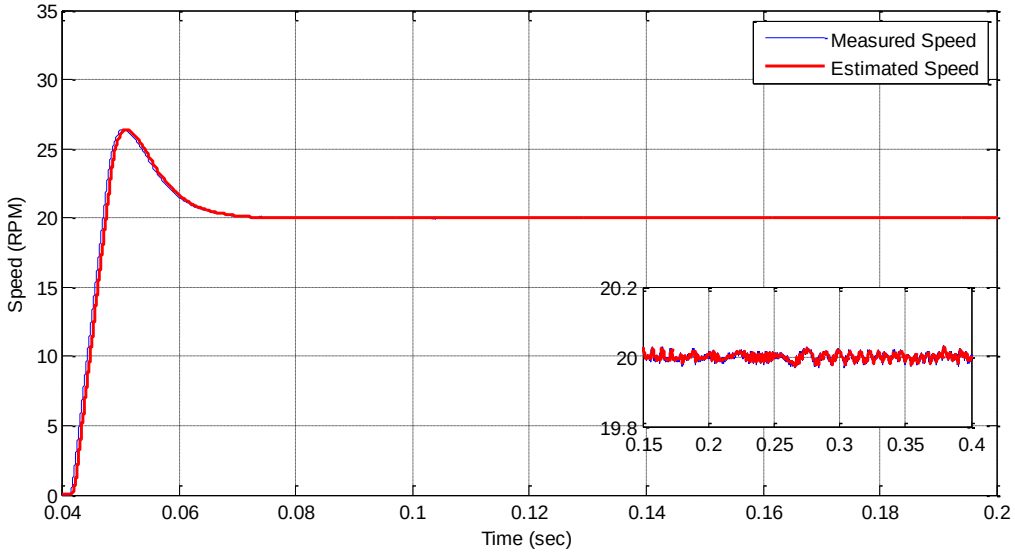

Figure 4. 4 Estimated and actual speed under no-load conditions, adaptation mechanism gains set as K_p= 100 and K_i =1000.

In order to further assess the effect of the different PI gains on the performance of the sensorless drives, the measured speed errors under the three sets of PI gains were compared. It can be seen from figure 4.4 that under the three sets of the PI gains, the measured speed error was under 0.5%. However, the measured speed error of the lowest set of PI gains is relatively higher in comparison to the PI sets with higher gains. With respect to the speed estimation error, figure 4.6 shows that the speed estimation error under the three sets of PI gains were well under 0.25%. In contrast to the measured speed error, it can be seen in figure 4.6 that the speed estimation error under the three sets of PI gains is almost identical in magnitude.

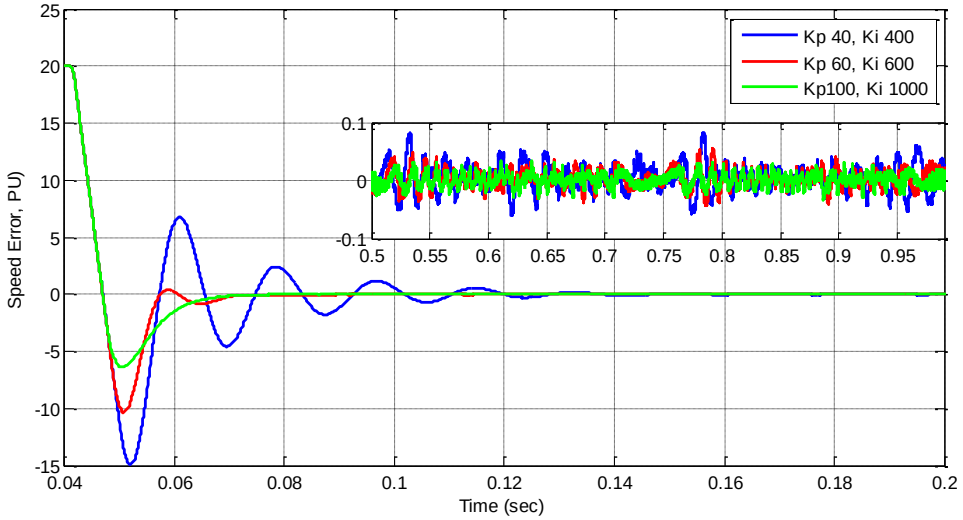

Figure 4. 5 Measured speed error comparison under no-load conditions.

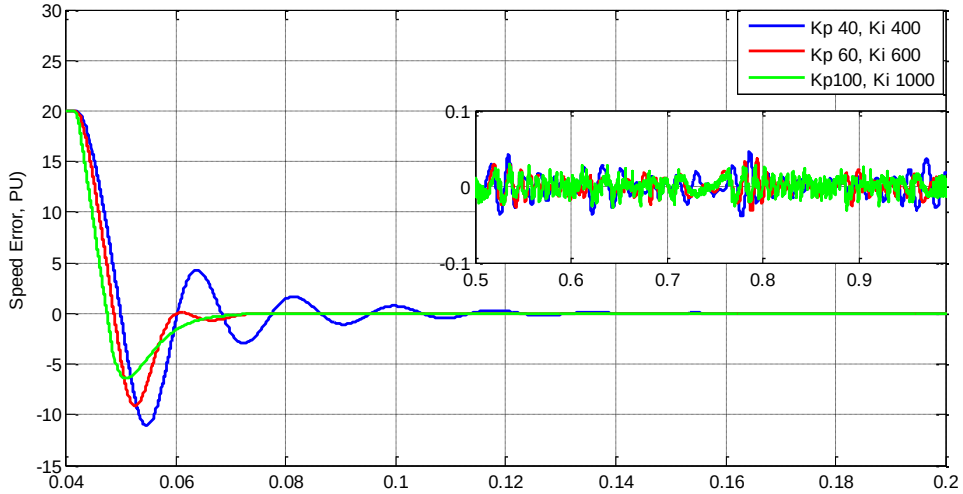

Figure 4. 6 Estimated speed error comparison under no-load conditions.

4.2.2 The Effect of the Adaptation Mechanism Gains on the Generation of High-order Harmonic under No-load Operations

In order to examine the frequency composition, a cross section of both the estimated speed and measured speed were analysed using Matlab's own FFT tool. The FFT tool is basically a readily available algorithm which performs fast Fourier transform to allow one to efficiently estimate component frequencies in data from a discrete set of values sampled at a fixed rate. Fast Fourier transforms (FFTs) have been described as "the most important numerical algorithms of our lifetime" [79]. A Fourier transform converts time or space to frequency and vice versa, and an FFT is a computer based implementation of the algorithm, used to rapidly compute such transformations.

Therefore, fast Fourier transforms are widely used for many applications in engineering, science, and mathematics. The FFT is a computationally effective method of calculating the discrete Fourier transform of a signal in the time-domain and in turn, will provide significant information about the spectral composition of this signal; that is to say, the different frequencies which constitute the signal in question.

One might be considered fortunate because Matlab® provides a readily available FFT function that is an effective tool for computing the discrete Fourier transform of a signal. The FFT contains information between 0 and F_s. However, it is known that the sampling frequency must be at least twice the highest frequency component. Therefore, the signal's spectrum should be entirely below $F_s/2$, which is known as the *Nyquist* frequency. The discrete Fourier function allows the computation of the fundamental component of a signal and also allows the observation of its harmonic components.

The examined cross section is extracted during the steady state to avoid incorporating any oscillation that may occur during transient state. Although visually, both of the speed signals seem to be free of any high levels of noise, the FFT analysis is able to reveal hidden frequency components. In order to investigate how the low adaptation gains influence the frequency spectrum of the estimated speed, the FFT analysis in figure 4.7 shows that the manifestation of high-order components in the frequency composition of the estimated speed is fairly insignificant where the highest harmonic component, which is relative to fundamental component is less than 0.06%.

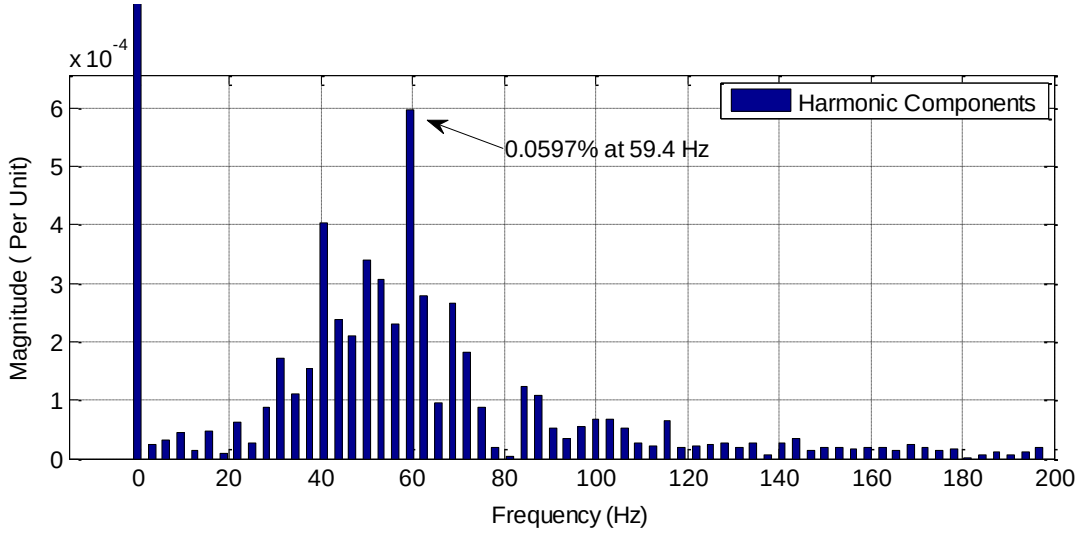

Figure 4. 7 Harmonic components at estimated speed K_p=40 K_i =400.

In practice, the terms of probing for high frequency components, analysing the frequency spectrum of the measured speed signal to some extent might be considered irrelevant, due to the fact that the characteristics of the measured speed mainly depend of the quality of the speed measurement unit. This is in most cases comprised of an incremental encoder and an encoder interface circuit. However, performing FFT analysis on the measured speed might reveal any hidden low frequency components, as it will be demonstrated in the experimental investigation section in chapter 6. Nevertheless, a spectral analysis has been carried out on the measured speed and in a similar manner, the performed FFT algorithm shown in figure 4.8 shows a negligible presence of high-order harmonics, where the highest harmonic components, which is also relative to fundamental components, is less than 0.093%.

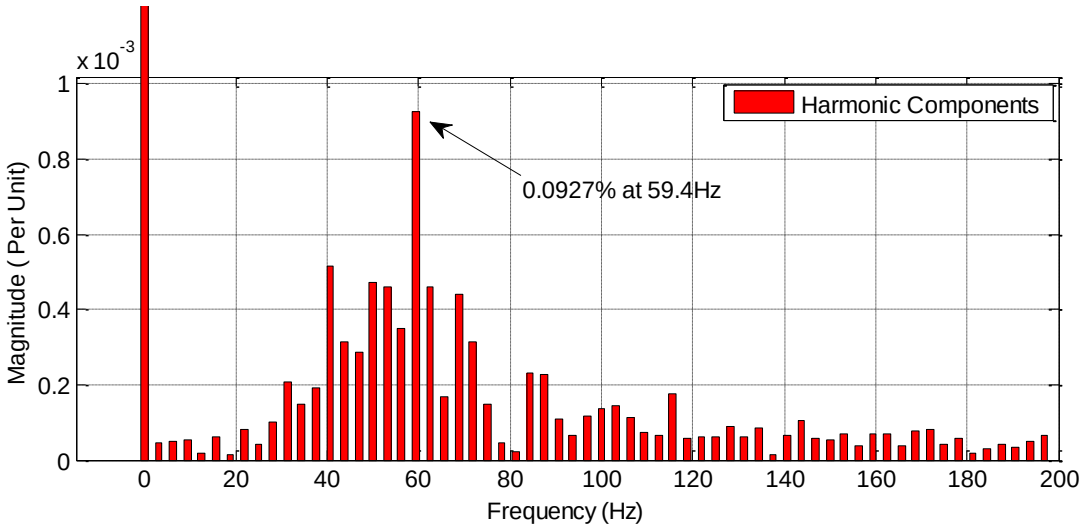

Figure 4. 8 Harmonic components at measured speed K_p=40 K_i =400.

Following the increase of the PI gains to K_p=100 and K_i =1000, the FFT analysis has shown a slight decrease in the magnitude of the harmonic components, which are less than 0.017%. This corresponds with figure 4.4, which shows that both the estimated and measured speeds follow each other very closely in contrast to figure 4.2, where both speeds seem to be somewhat oscillatory during the steady state.

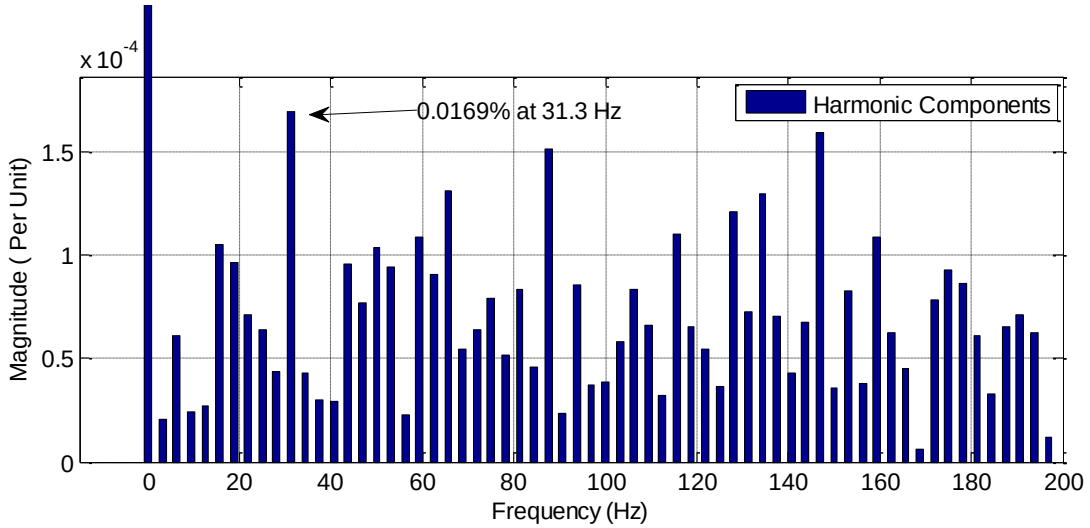

Figure 4. 9 Harmonic components at estimated speed K_p=100 K_i =1000.

In figure 4.8, the FFT analysis also shows a decrease in the magnitude of the harmonic components, which is can also be explained by referring back to figure 4.4 where the zoomed in cross section shows a visible reduction in the amplitude of the oscillations compared to those oscillation found in figure 4.2, when a PI of low gains was applied.

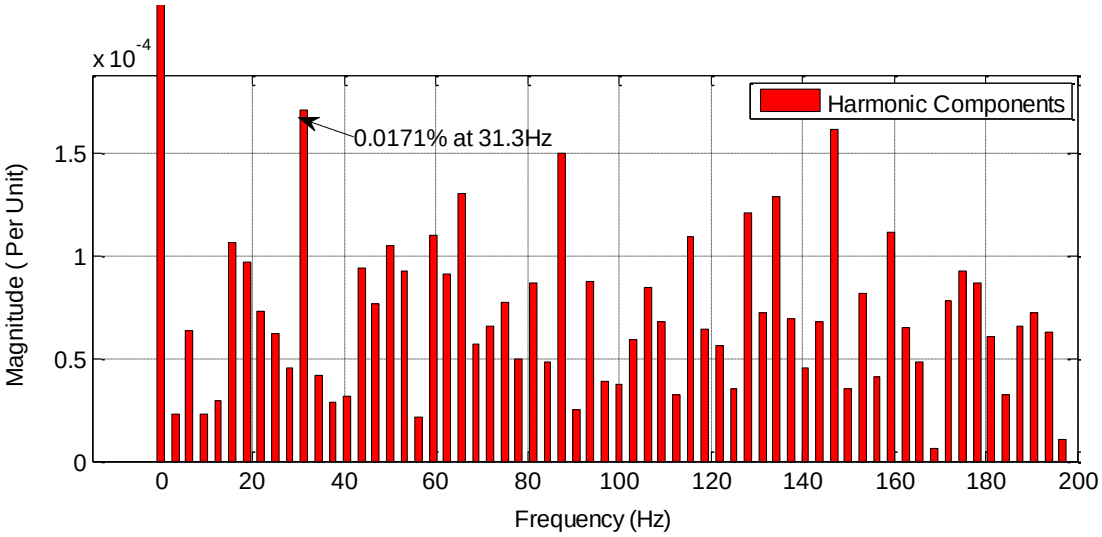

Figure 4. 10 Harmonic components at measured speed K_p=100 K_i =1000.

4.2.3 The Effect of the Adaptation Mechanism Gains the Estimate Speed under Loaded Operations

The performance of the modelled MRAS based speed estimator was also tested by exerting a full torque load during a steady state and using the same set of PI gains from the no-load operation. Figure 4.11 demonstrates that a low gains PI based adaptation mechanism will tend to weaken the dynamic performance of the sensorless drive, in terms of rejecting a load type disturbance. As it can be seen from figure 4.11, the speed starts to oscillate when a sudden load is exerted and by zooming in at cross section during the steady state, it can be seen clearly that there is a steady state error for the measured speed is typically under 1%.

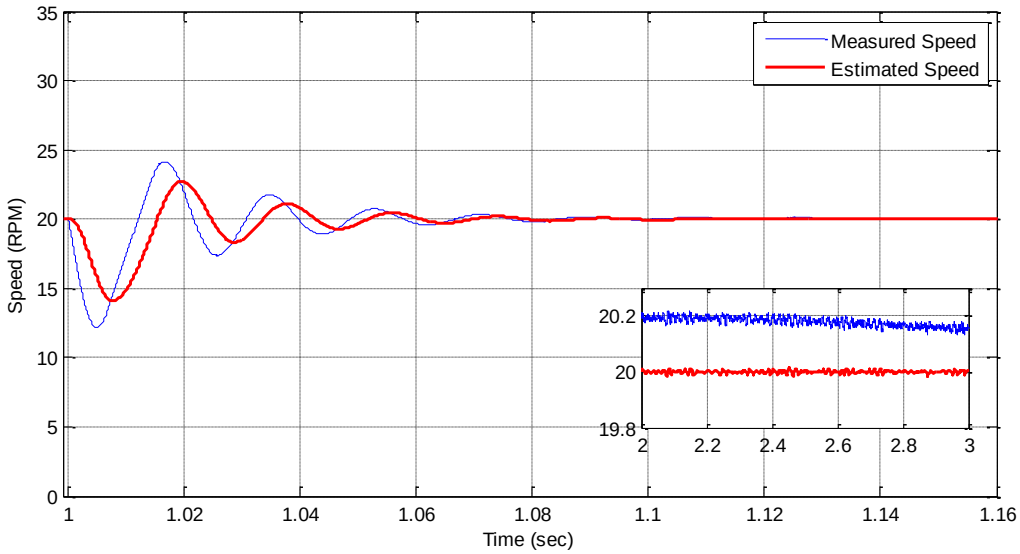

Figure 4. 11 Estimated & Measured Speed under loaded conditions, adaptation mechanism gains set as K_p= 40 and K_i =400.

In comparison to figure 4.11, figure 4.12 shows how an increase of PI gains improves the performance of the sensorlees drive, where the measured speed was not as oscillatory and the drive managed to compensate and converge to the desired speed limit, as set by the reference speed. Figure 4.13 also shows an improved steady state performance where there is a noticeable reduction in the steady state error of the measured speed is typically halved to under 0.5%.

Figure 4.13, demonstrates how an adaptation mechanism that employs a PI with high gains improves the dynamic performance with respect to load disturbance rejection. It

can be seen from figure 4.13 that not only does the sensorless drive recover more rapidly after a sudden full torque load has been exerted, but also how the steady state error is significantly reduced.

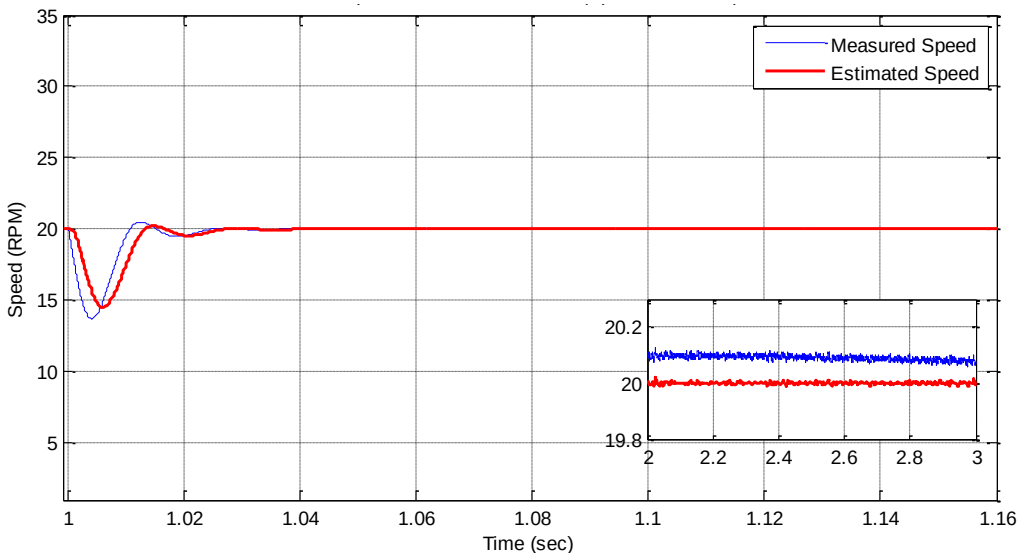

Figure 4. 12 Estimated & measured speed under loaded conditions, adaptation mechanism gains set as K_p= 60 and K_i =600.

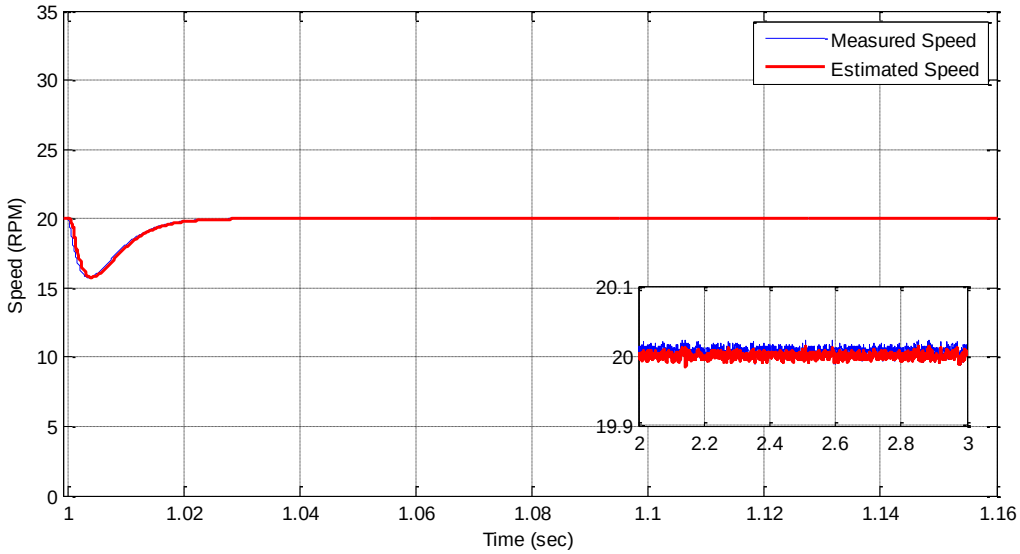

Figure 4. 13 Estimated & measured speed under loaded conditions, adaptation mechanism gains set as K_p= 100 and K_i =1000.

To additionally evaluate the effect of the different PI gains on the performance of the sensorless drives and also clearly demonstrate the advantage of having an adaptation

mechanism with high gains, particularly under post load exertion, the measured speed errors under the three sets of PI gains are compared. The difference in terms of rejecting the mechanical load disturbance is highlighted in figure 4.14. Figure 4.14 shows that when the lowest set of PI gains was selected the measured speed error is approximately 1%. As the adaptation mechanism gains were increased, the measured speed error decreased noticeably. It can also be seen from figure 4.14 that the highest set of PI gains have managed to significantly eliminate the speed error. This confirms that it is desirable to have an adaptation mechanism with high gains to achieve a more superior performance in terms of maintaining fast and robust dynamic response.

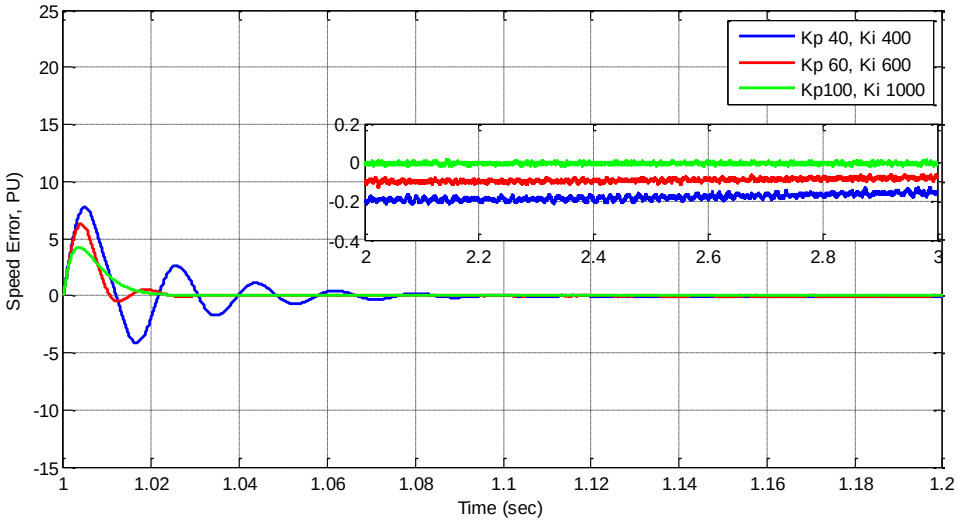

Figure 4. 14 Measured speed error comparison post load exertion.

In contrast to the measured speed error, figure 4.15 demonstrates that the load exertion did not increase the magnitude of the speed estimation error. However, in comparison to the no-load operation, where the estimated speed error is less than 0.25%, the estimated speed error has decreased to well below 0.125%, even though the measured speed error is noticeably affected.

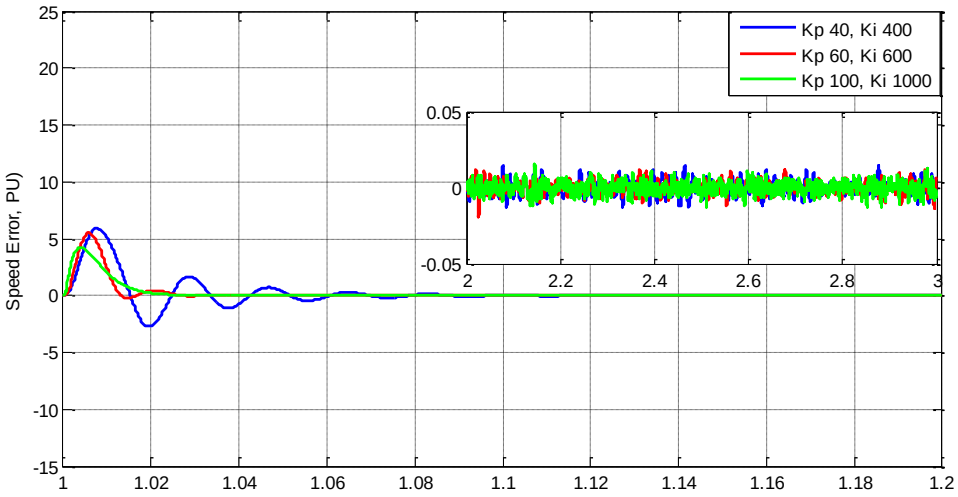

Figure 4. 15 Estimated speed error comparison post load exertion.

4.2.4 The Effect of the Adaptation Mechanism Gains on the Generation of High-Order Harmonic under Loaded Operations

A cross section of the estimated speed signal was analyzed using the FFT tool to examine its frequency composition and whether the adaptation mechanism gains bear a comparable effect on the signal's frequency spectrum, post load exertion. Starting with low PI gains, from the data shown in figure 4.16, it is apparent that the presence of high-order harmonics is rather minute where the highest harmonic component only forms a 0.0261% of fundamental components. In contrast to the no-load operation, it appears that the load has an attenuating effect because the same set of low gains has produced a relatively higher level of harmonics in terms of magnitude.

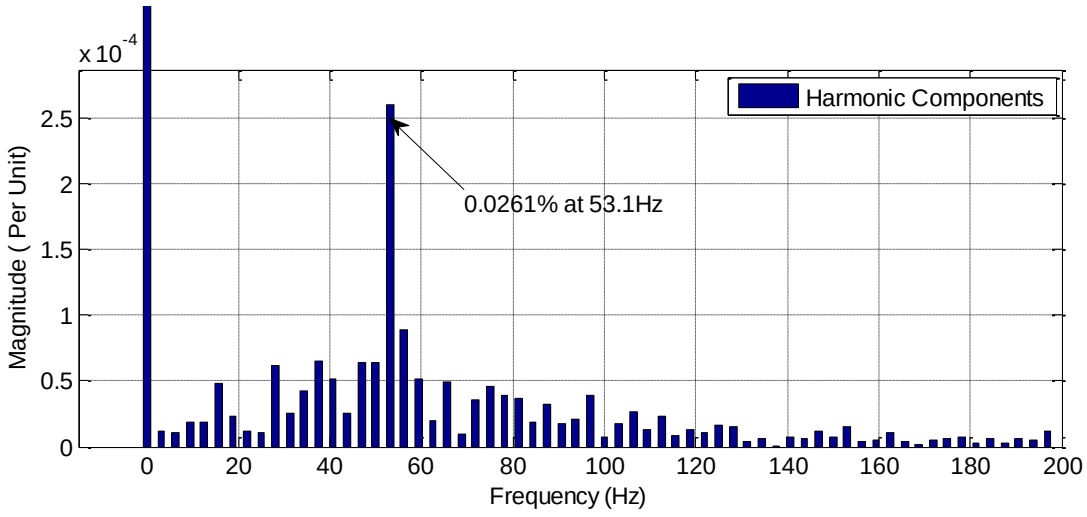

Figure 4. 16 Harmonic components at estimated speed post load exertion, adaptation mechanism gains set as K_p= 40 and K_i =400.

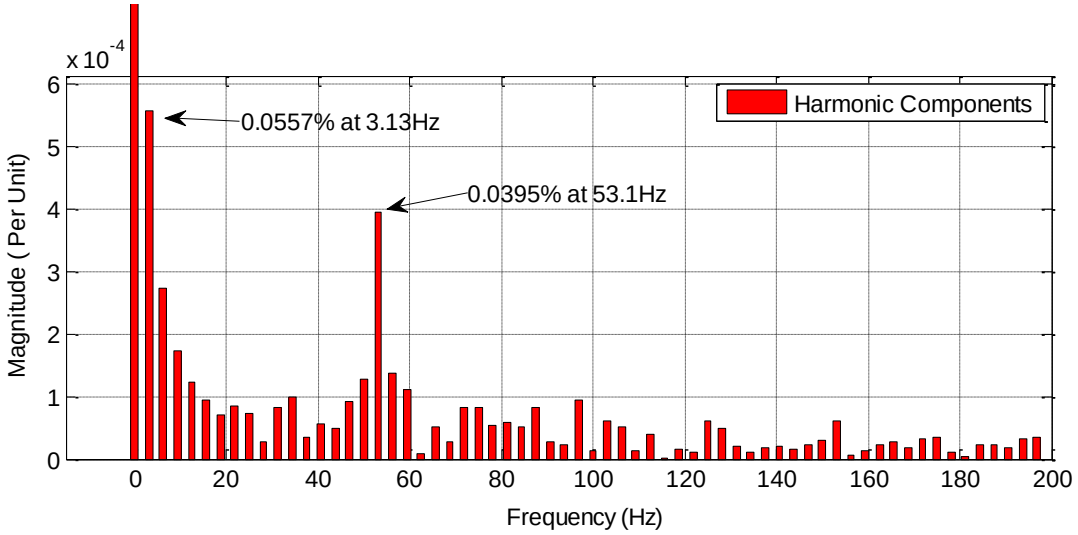

Figure 4. 17 Harmonic components at measured speed post load exertion, adaptation mechanism gains set as K_p= 40 and K_i =400.

The FFT analysis on the measured speed has also shown a reduction in the magnitude of the harmonic content, which has decreased to 0.0557% from 0.0927% in comparison to the no-load operation that was carried out while implementing the same low PI gain sets.

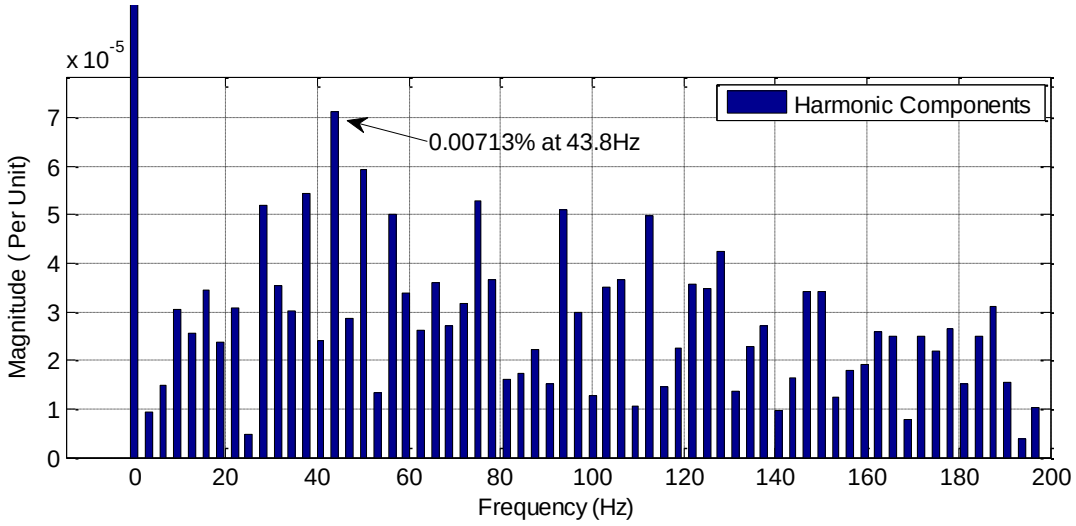

Figure 4. 18 Harmonic components at estimated speed post load exertion, adaptation mechanism gains set as K_p= 100 and K_i =1000.

It appears that increasing the adaptation mechanism gains reduces the magnitude of the harmonic components on both the estimated and the measured speed signals in a similar

way to the no-load operation. From figure 4.18, we can see that the maximum harmonic component has decreased from 0.0169% to 0.00713% during the loaded operation, where this reduction is attributed to both the mechanical load exertion and the increase of adaptation mechanism gains. Figure 4.15 also shows a reduction of 57.54% in magnitude of the previously recorded highest harmonic component during the no-load operations in the measured speed.

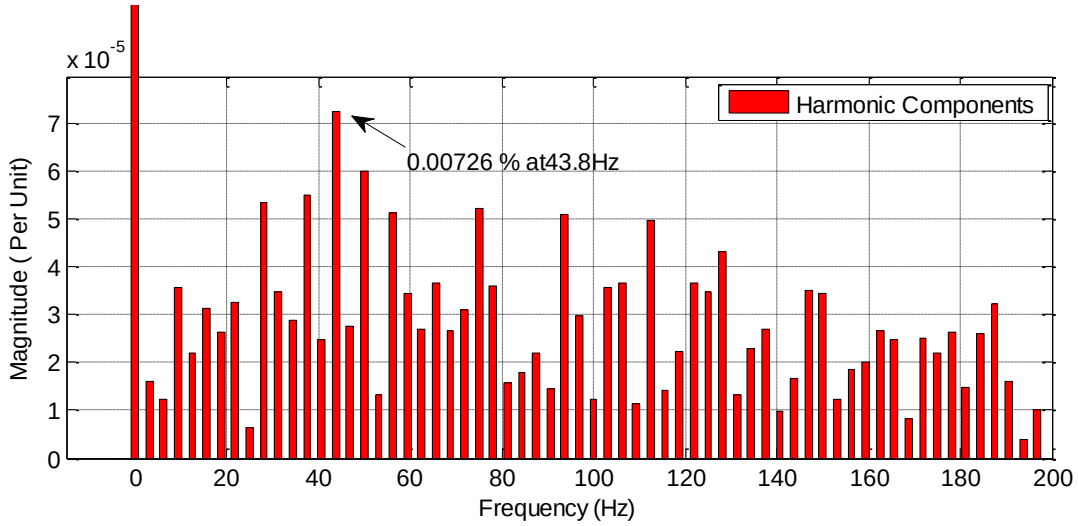

Figure 4. 19 Harmonic components at measured speed post load exertion, adaptation mechanism gains set as K_p= 100 and K_i =1000.

Although the simulation based investigation has shown that the presence of high-order harmonics in both the estimated speed and the measured speed is minuscule and therefore irrelevant, the experimental investigation on the real drive system is likely to reveal harmonic components with a relatively higher magnitude.

4.3 Summary

With respect to simulation, the results presented in this chapter have given an in depth account on the ability of the adaptation mechanism gains to influence the dynamic performance of an MRAS based sensorless speed drive. The acquired simulation results have demonstrated clearly that by increasing the gains of the adaptation mechanism, fast speed convergence has been achieved and a more robust dynamic response is observed mainly during transients as well as under load exertion. Furthermore, the simulation results have also demonstrated that by increasing the adaptation mechanism gains of both the estimated and measured speed, they become less oscillatory and the frequency spectrum exhibits a somewhat negligible presence of harmonic components. Regarding the harmonic analysis, the simulation results appear to disagree with what has previously been acknowledged by [28, 29]. Because it was indicated within their literature that simulation based investigations have shown that utilising an adaptation mechanism with high PI gains maintain a robust dynamic performance, it also causes the estimated speed to display a high level of noise. Furthermore, these results do not appear to support the claims regarding the generation of high-order harmonics in the estimated speed due to high adaptation mechanism gains.

In terms of simulation, the results presented in this chapter are unique because they provide a detailed description that shows how the gains of the adaptation mechanism can affect the performance of the speed estimation process. In addition, even though the harmonic analysis of both the estimated and the measured speed signals have revealed a negligible presence of high-order harmonics, the FFT based harmonic analysis has nonetheless offered an unprecedented insight into the frequency spectrum of both speed signals.

The experimental investigation will not only present a unique and detailed account into how the adaptation mechanism gains can cause the estimated speed within a real drive system to exhibit high level of noise, but will also demonstrate how the generated noise can influence the overall speed estimation process. In addition, the experimental investigation will provide an unprecedented detailed insight on to the spectral composition of the generated noise in the estimated speed, showing how the actual speed is affected by the nature of this spectral content.

Chapter 5 - Experimental Setup

5.1 Introduction

The experimental hardware is built to provide a testing platform for the practical implementation. The hardware is divided into three main units. The first unit is the motor drive unit, which is the unit responsible for delivering power to the induction motor as well as supplying the digital processing unit with the required measurements to establish the control. The second unit consists of a digital signal processing unit based on an **eZdsp™ F28335** development board employing a **TMS320F28335** as a digital signal controller. Finally, the third unit is the motor test rig, consisting of an induction motor coupled with a DC motor and an incremental encoder.

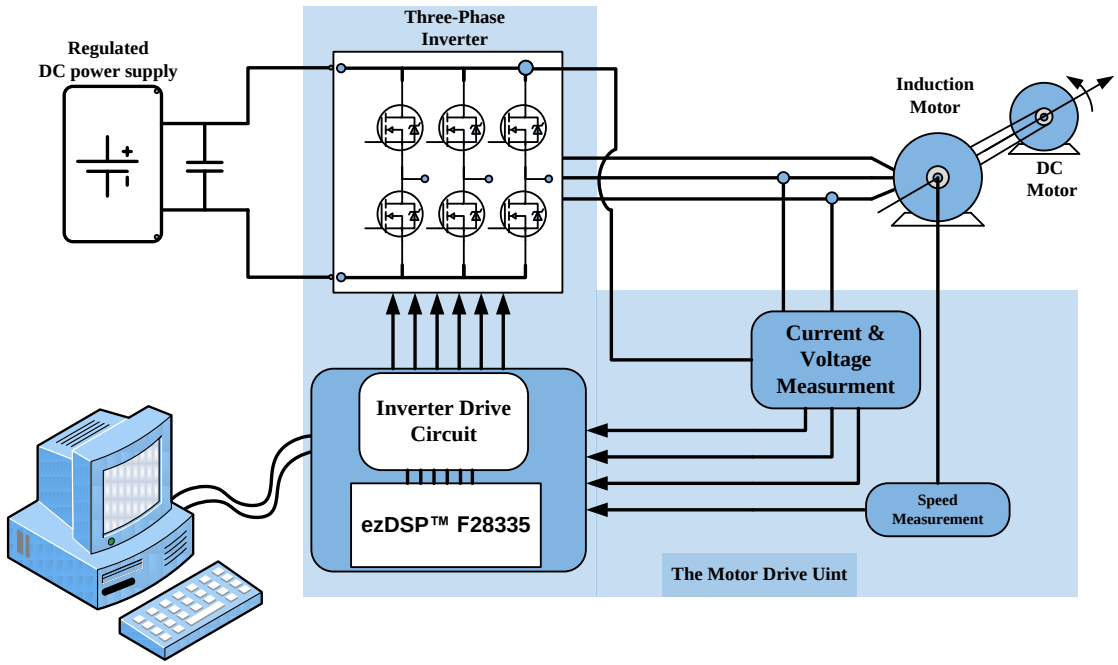

Figure 5. 1 Block diagram of the three-phase VSI used in the research.

5.2 Motor Drive Unit

The motor drive unit is comprised of: the three-phase inverter, the fully-protected gate drive unit, the current measurement unit, the DC bus voltage measurement, the auxiliary power stage and the speed measurement unit.

5.2.1 Three-Phase Inverter

The three-phase inverter is responsible for the delivery of power to the induction machine by transforming direct current to alternating current. The digital processing unit along with the three-phase inverter form a variable frequency drive that manages the operating speed of the induction motor by controlling the frequency and magnitude of the voltage applied to the motor.

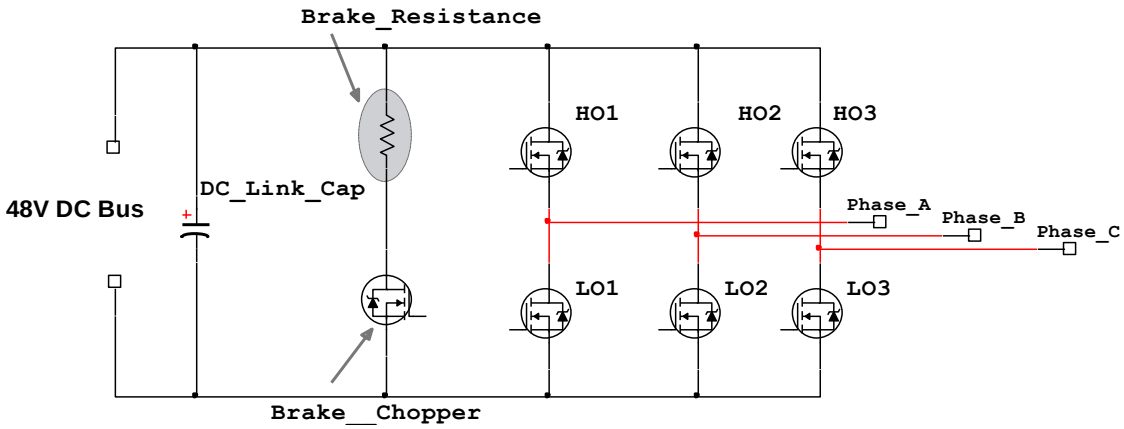

Figure 5. 2 Schematic diagram of the three-phase VSI used in the research.

Figure 5.2 shows the schematic diagram of the developed three-phase inverter used in the experimental implementation. The inverter is comprised of six high-speed power MOSFETs; HO1, HO2 and HO3 are high side devices, where LO1, LO2 and LO3 are low side devices. It also consists of a DC link capacitor, a 48V DC link bus and a brake resistor, which is connected in parallel with the inverter. The DC link capacitor is commonly used in DC to AC inverters in order to decouple the effects of the inductance from the DC voltage source to the power bridge. The DC link capacitor also plays a role in reducing the leakage inductance of the inverter power bridge. In addition, the DC link capacitor smoothes and stabilises the voltage produced by the DC voltage source [80, 81]. Figure 5.2, shows a seventh MOSFET that is connected in series with the brake resistance, which will be activated during dynamic braking to help dissipate the energy generated by the induction motor during deceleration.

5.2.2 Fully-protected Gate Drive Unit

Effectively, the Gate Drive unit is an isolation stage between the digital signal processor and the power inverter. It delivers the switching signal, the PWM, from the DSP where

it acts as an interface between the logic-level output of the PWM module and the switching devices in the inverter.

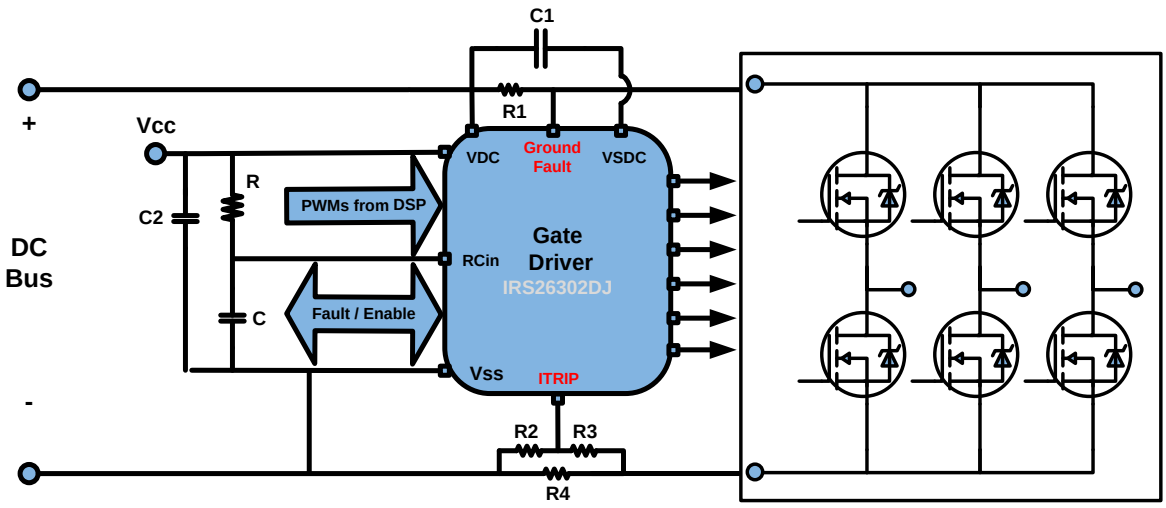

Figure 5. 3 Schematic diagram for the gate drive connection.

A gate driver is a power amplifier that accepts a low-power input from an IC type controller and produces a high-current drive input to the gate of a high-power transistor, such as an IGBT or power MOSFET. Gate drivers can be provided either on-chip or as a discrete module. In essence, a gate driver consists of a level shifter in combination with an amplifier.

The gate drive unit is designed around an IRS26302DJ three-phase bridge driver chip, which is manufactured by *International Rectifier*. It can drive up to seven power switches and features an integrated dead-time protection circuitry.

The dead-time feature inserts a time period referred to as a minimum dead-time, in which both the high- and low-side power switches are held off. This is feature avoids shoot-through by ensuring that the power switch being turned off has fully turned off before the second power switch is turned on exclusively. This minimum dead-time is automatically inserted whenever the external dead-time is shorter than the default minimum dead-time; external dead-times larger than the default minimum dead-time are not modified by the gate driver.

The IRS26302DJ chip facilitates an overall protection against over-current and under-voltage lockout protection. The under-voltage lockout protection guarantees that the IC

drives the external power devices, only when the gate supply voltage is sufficient to fully operate the power devices. Without this feature, the gate of the external power switch could be driven with a low voltage, resulting in the power switch conducting current while the channel impedance is high. This could result in very high conduction losses within the power device and could lead to the power device failure. The IRS26302DJ is equipped with shoot-through protection circuitry, also known as cross-conduction prevention circuitry. This protection circuitry prevents both the high- and low-side switches from conducting at the same time. The IRS26302DJ is also equipped with an advanced input filter that allows an improvement in the input/output pulse symmetry of the high voltage IC (HVIC), which helps to reject noise spikes and short pulses. This is useful for filtering noise on the logic input lines of the IC, for example. The driver chip also guarantees an equal switching time which eliminates any nonlinearity associated with unequal switching periods.

5.2.3 Current Measurement Unit

The current measurement unit is based on a CKSR 6-NP high accuracy current transducer manufactured by *LEM*. The CKSR 6-NP provides an excellent galvanic isolation between the primary and the secondary circuits.

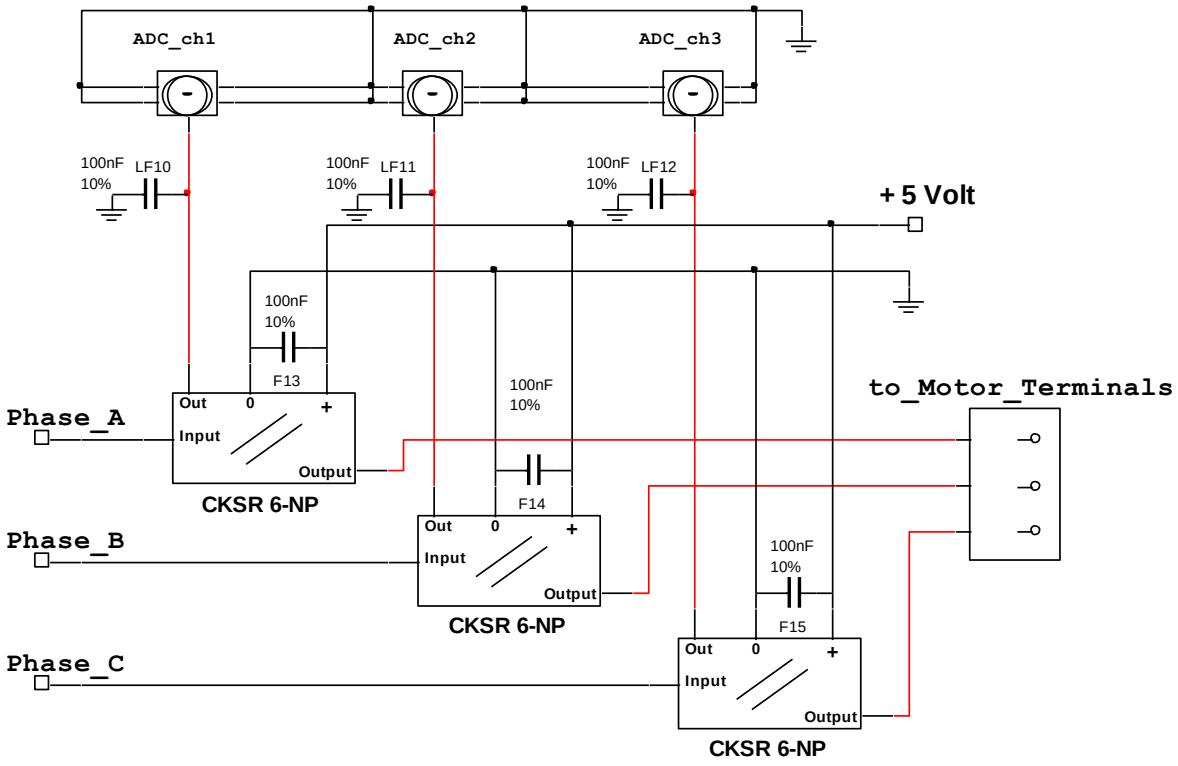

Figure 5. 4 Schematic diagram of the current measurement unit.

The device has the capability of measuring high bandwidth signal from a DC signal up to 300 kHz. This facilitates accurate motor current measurements when applying the control algorithms. The analogue output of the current sensor is converted into a discrete form using a 12-bit analogue to digital converter that is already present on the **eZdsp™ F28335 DSP** board. No filtering of the currents was carried out in order to maintain dynamic performance, due to the natural filtering effect of the induction machine, resulting in sinusoidal motor currents.

5.2.4 DC Bus Voltage Measurement

A potential divider is used to measure the DC link voltage giving an output that is then amplified to an appropriate level before being applied to the analogue to digital convertor (ADC) input channel of the DSP using a TLC2274. This is an operational amplifier from *Texas Instruments*. The gain of the operational amplifier is controlled by the variable resistor, R7.

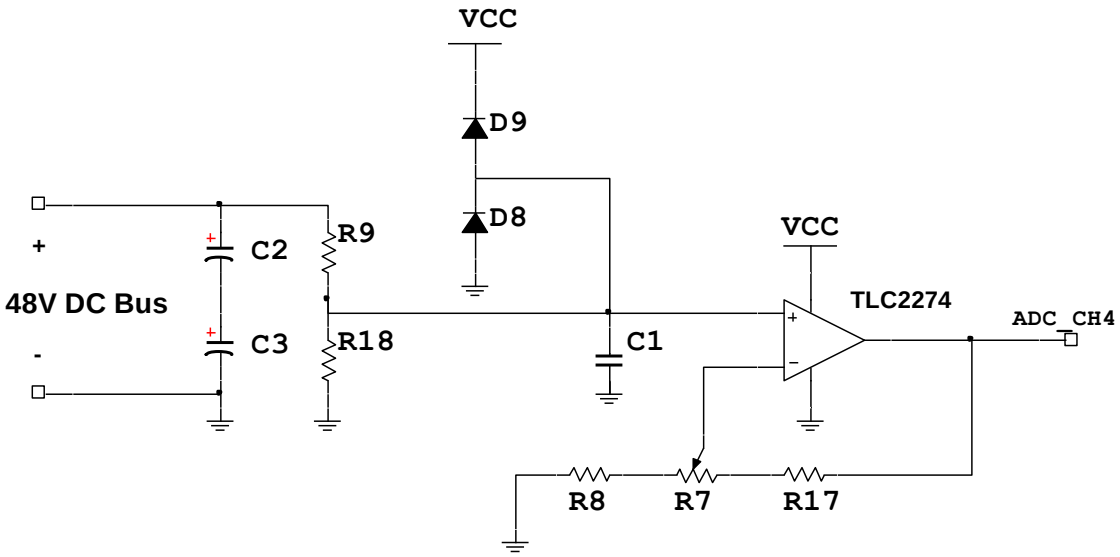

Figure 5. 5 Schematic diagram of DC bus voltage measurement.

5.2.5 Auxiliary Power Stage

The three-phase inverter is supplied by a 48V DC Bus. The other components in the motor drive circuit require lower voltages in order to operate, such as the current sensors, which need ±5V DC and the IRS26302DJ chip, which requires ±15V. As a result, an auxiliary power stage has been incorporated to provide ±5V and ±15V. The

auxiliary power stage is based on the NDY4805C and NDY4815C devices that are manufactured by *Murata Power Solutions*. These two devices are isolated DC/DC converters and both are driven by the main 48V DC Bus, providing ±5V and ±15V respectively to the circuit's components.

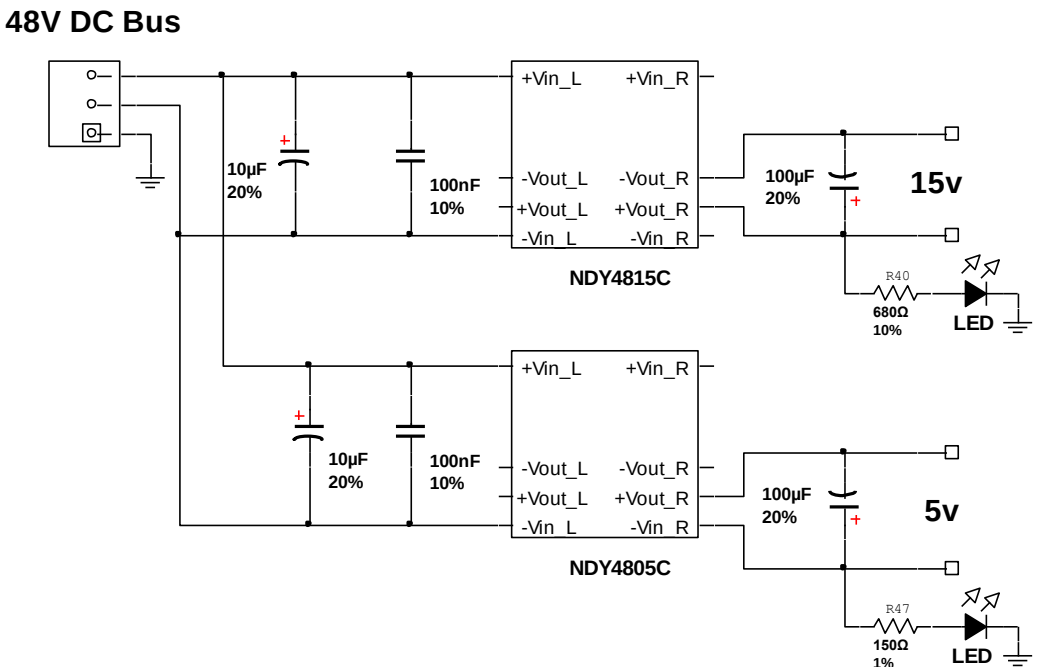

Figure 5. 6 Schematic diagram of the auxiliary power stage.

5.2.6 Speed Measurement Unit

The speed measurement unit is designed to establish an interface between the incremental encoder and the **eZdsp™ F28335**. The incremental encoder generates quadrature output pulses, A, B and Index, enabling the measurement of position, speed and direction. The output of the speed measurement unit is read by the *Enhanced Quadrature Encoder Pulse*, eQEP, on the **eZdsp™ F28335**.

The encoder interface unit converts the voltage levels of the incremental encoder signals to a voltage level that is suitable to be read by the eZdsp™. Figure 5.7 shows the schematic diagram of the speed measurement unit. The interface is established via three high-speed opto-couplers. The speed measurement unit consists of a sub power stage that is based on the NDY2403 and NDY2415 devices, manufactured by *Murata Power Solutions.* These two devices are also isolated DC/DC converters, but they are supplied by 24V DC and respectively, they in turn provide ±3V and ±15V to the unit's components. The 15V is used to power the incremental encoder and the 3V is used as the opto-coupler's VCC. The opto-coupler's logic gate output is 3V, which is compatible with the **eZdsp™ F28335** eQEP's input ports.

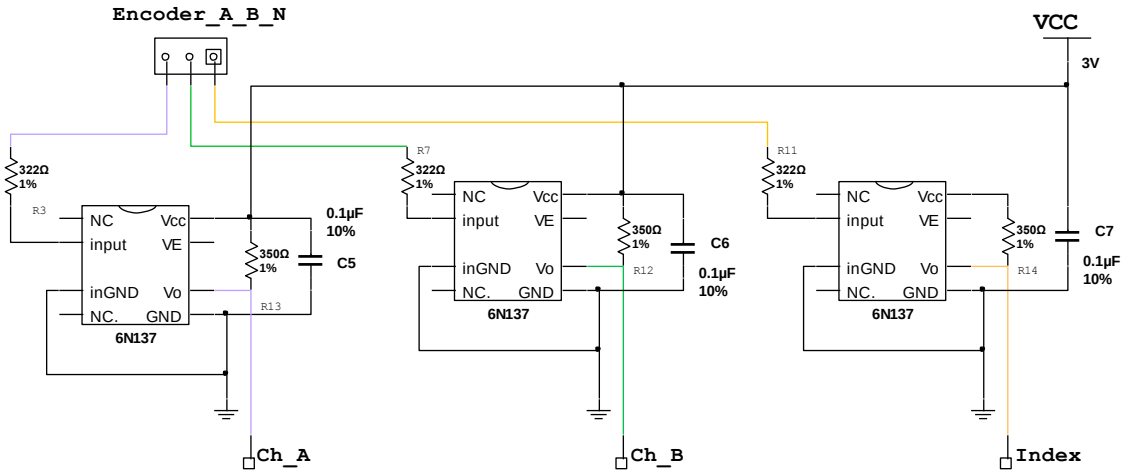

Figure 5. 7 Schematic diagram of the encoder interface.

5.3 Motor Test Rig

The experimental work was carried out using an induction motor based test rig, which was built with the assistance of the School's mechanical workshop staff. The motor test rig is comprised of two motors: a squirrel cage induction motor and a DC generator comprising of a permanent magnet motor with incremental encoder. Tables 5.1 to 5.3 show the specification of each part respectively. The DC machine is used as a load machine, applying a torque load to the induction machine. A photograph of the experimental rig is shown in Figure 5.8.

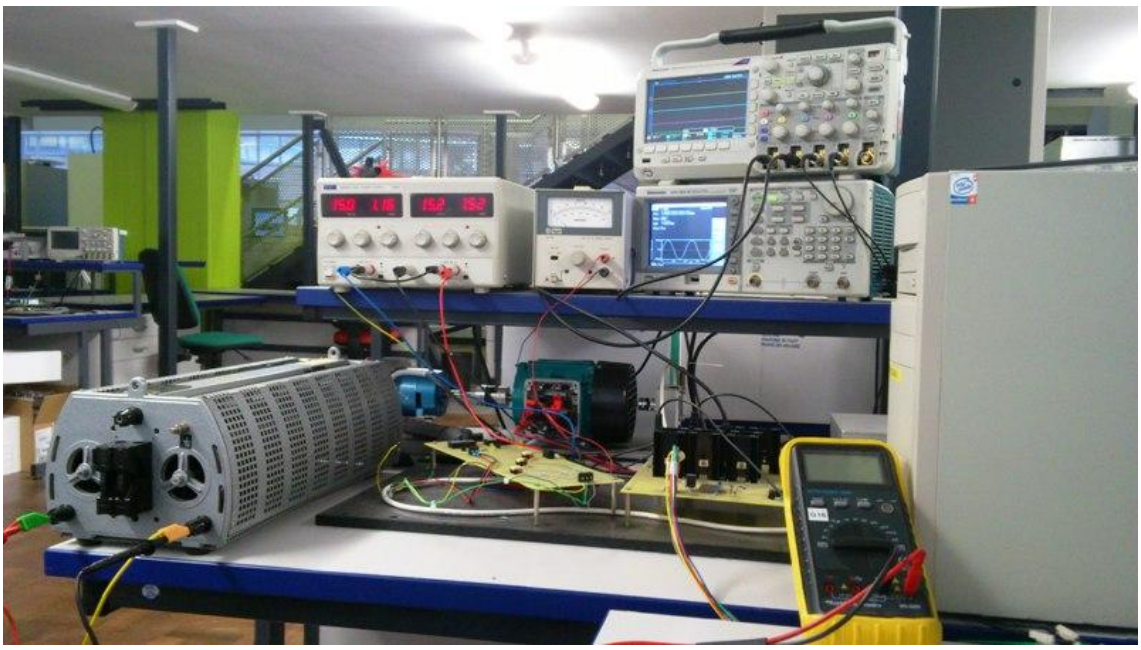

Figure 5. 8 A photograph of the workstation on which the experiments were conducted.

Table 5.1 Induction motor specifications

Manufacturer	***Brook Crompton***
Frame Reference and size	WU-DA63SF
Full Load Speed	1370 RPM
Rated Power	0.12kW (hp 0.166)
Rated Current	3.32 A
Rated Voltage	48V
Pole Pairs	2
Duty Type	Continuous duty
Insulation Class	Class F
Full load torque	0.85 MN Nm
Rotor inertia WK^2	0.0005 J.kgm^2

Table 5.2 DC motor specifications

Manufacturer	***Parvalux***
Full Load Speed	4000 RPM
Rated Power	160W
Rated Current	4.2A
Rated Voltage	50V
Shaft Type	M
Duty Type	Continuous Rating

Table 5.3 Shaft encoder specifications

Manufacturer	***Hengstler***
Maximum Speed	6000 RPM
Resolution	1024 Pulse per Revaluation
Encoder Type	Incremental
Supply Voltage	10-30 Volt
Shaft Type	Soild
Maximum Operating Temperature	+ 60°C
Switching Frequency	200 kHz
Flange Material	Aluminium
Mounting Type	Flange
Protection	Short Circuit Protection
Output Type	Quadrature Output

5.4 Summary

This chapter has described the experimental setup utilised to facilitate the experimental investigation. The hardware was divided into two sections: the motor drive board, which was based on an **eZdsp F28335™** and consists of the current, voltage and the speed measuring units. The motor rig was based on a 120W induction motor coupled with a DC generator and an incremental encoder. The concept behind the design as well as the functionality of each unit was explained.

The next chapter will present the experimental results acquired via the implementation of the built hardware described in this chapter. The experimental results validated the functionality of the hardware and all of the investigative targets were met and the functionality of an original solution was proven.

Chapter 6 - Experimental Investigation

In a sensorless MRAS speed estimator as stated earlier, there have been a number of claims about the generation of high-order harmonics in the estimated speed, particularly as the gains of the adaptation mechanism are increased [28, 29]. Considering the fact that as far as the literature is concerned, the phenomenon regarding the generation of high-order harmonics has only been generally acknowledged and no detailed investigation has yet been carried out to either highlight the phenomenon's attributes or overcome its negative side effects. The purpose of this chapter is to describe the experimental work undertaken with the intention of not only showing that those claims were not exactly correct, but to also draw attention to additional findings. A rotor flux-linkage based MRAS has been implemented in a direct vector controlled induction motor drive. The sensorless scheme is implemented in real-time via an **eZdsp™ F28335**, which is a general purpose digital controller platform. The core of the platform is a *Texas Instruments* **TMS320F28335**.

6.1 The Drive's Sensorless Performance

In these tests, the vector control drive is operating in the closed loop sensorless mode, where the estimated speed is utilised for both speed control and rotor flux orientation. The sensorless performance is verified to be correctly functional and figures 6.1 and 6.2 show this. The correct speed estimation is confirmed by comparing the estimated speed with the actual speed, which is measured via the speed measurement unit that was discussed in chapter 5. Figure 6.1 shows the drives performance when subjected to a speed reference step change from 20% to 70% under no-load conditions. Conversely, figure 6.2 shows the drive's performance when subjected to speed change from 70% rated speed to 20% rated speed. As it can be seen from figures 6.1 and 6.2, correct speed estimation is established and the actual speed measurement corroborates this.

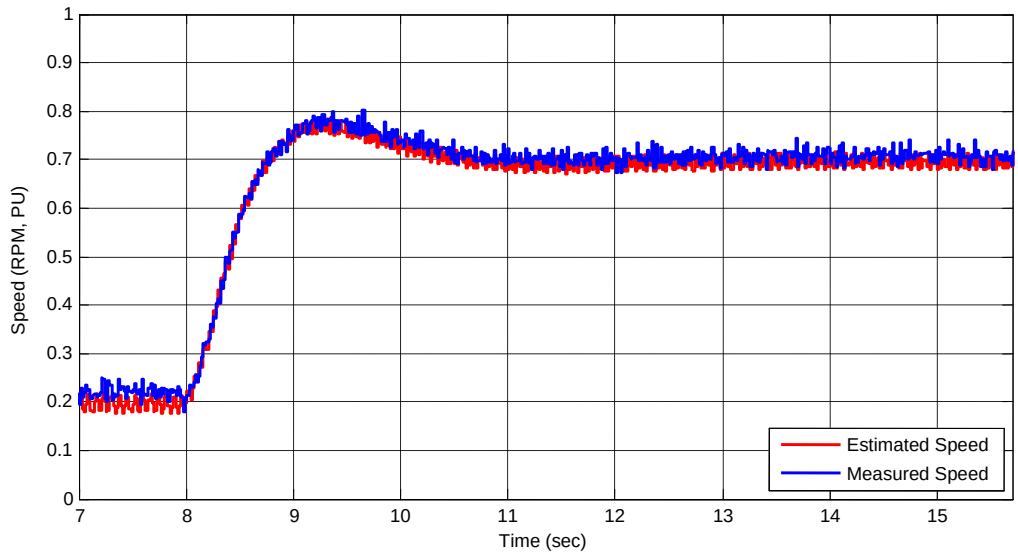

Figure 6. 1 Estimated and actual speed under no-load conditions with a step-up speed change.

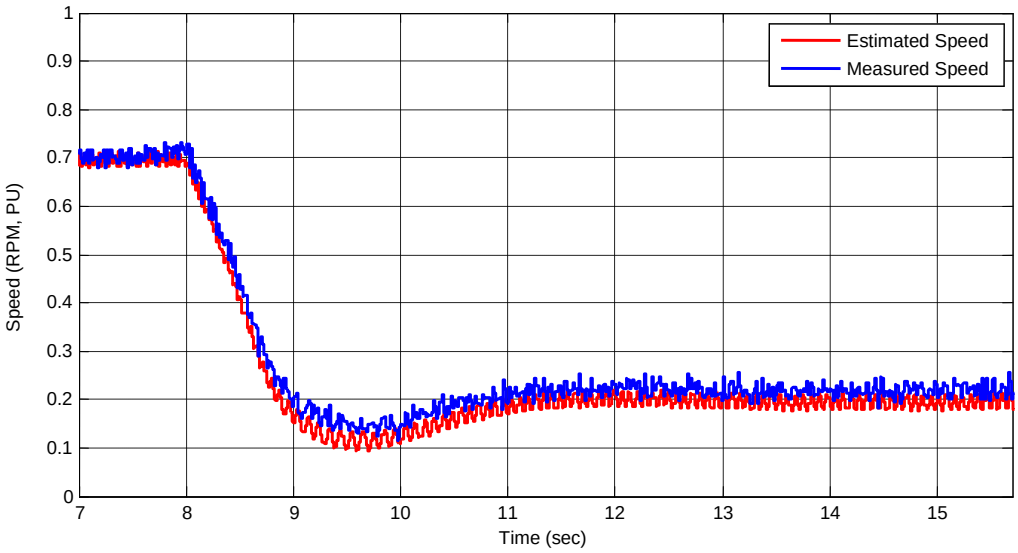

Figure 6. 2 Estimated and Actual Speed under no-load conditions with a step-down speed change.

6.2 Speed Estimation Performance under Different Adaptation Mechanism Gains

As discussed in chapter 2, the roll of the adaptation mechanism, which is basically a PI controller, is to tune the estimated speed, $\hat{\omega}_r$, so that the difference between the state variables is driven to zero. The selection of the correct PI gains K_p and K_i is quite significant because not only can it influence the overall performance of the system in terms of stability but, also ensures that the estimated speed will converge to the desired value with satisfactory dynamic characteristics [3, 31, 40]. It has been observed that with high adaptation gains, a fast speed convergence is achieved and the dynamic performance during the transient state and the load exertion is fast and robust. However,

the estimated speed begins to exhibit a high level of noise as the values of K_p and K_i are increased [3, 20, 31, 33, 40, 41, 82]. This section is set to closely examine the sensorless performance of the drive system under different PI gains, including the implications that these gains bear on the speed control process. The experimental results in this section are captured in real-time during sensorless operation, where the speed signals are sampled at a frequency of 100 Hz. The PI controller is manually tuned by arranging its parameters according to the systems response during transient states, produced by a step change in the reference speed. The gain variables K_p and K_i are tuned while observing the systems response until a satisfactory response is acquired.

The drive's sensorless performance is tested under 4 sets of PI gains, starting from low value gains to high value gains. The test is carried out by subjecting the motor to a step input of 0.4 PU. Initially, a PI with low gains was selected and figure 6.3 shows the performance of the sensorless drive and both of the estimated and the measured speeds are displayed. The PI gains were set as $K_p = 2$ and $K_i = 200$. Figure 6.3 shows a smooth estimated speed and a measured speed that correctly follows the estimated speed.

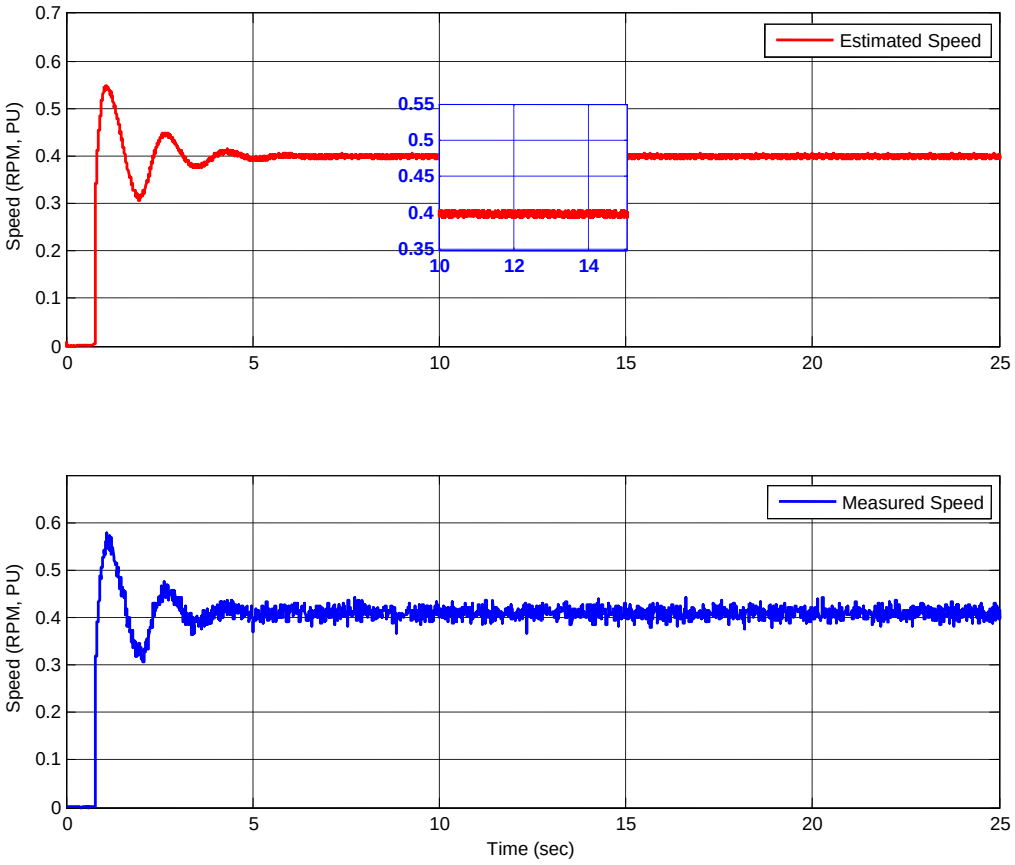

Figure 6. 3 Estimated and measured speed, adaptation mechanism gains set as $K_p = 2$ and $K_i = 200$.

Also shown in figure 6.3 is that the speed signals require a noticeable period of time before they settle and converge to the desired set speed. This is translated into a relatively long settling time of 5.3858 seconds, of which the measured speed requires to settle into the steady state where the steady state error is less than 2.5%. Finally, figure 6.3 also shows a significant overshoot in both the estimated speed and the measured speed. The PO of the estimated speed is 37.090975% and the PO of the measured speed is 44.076%.

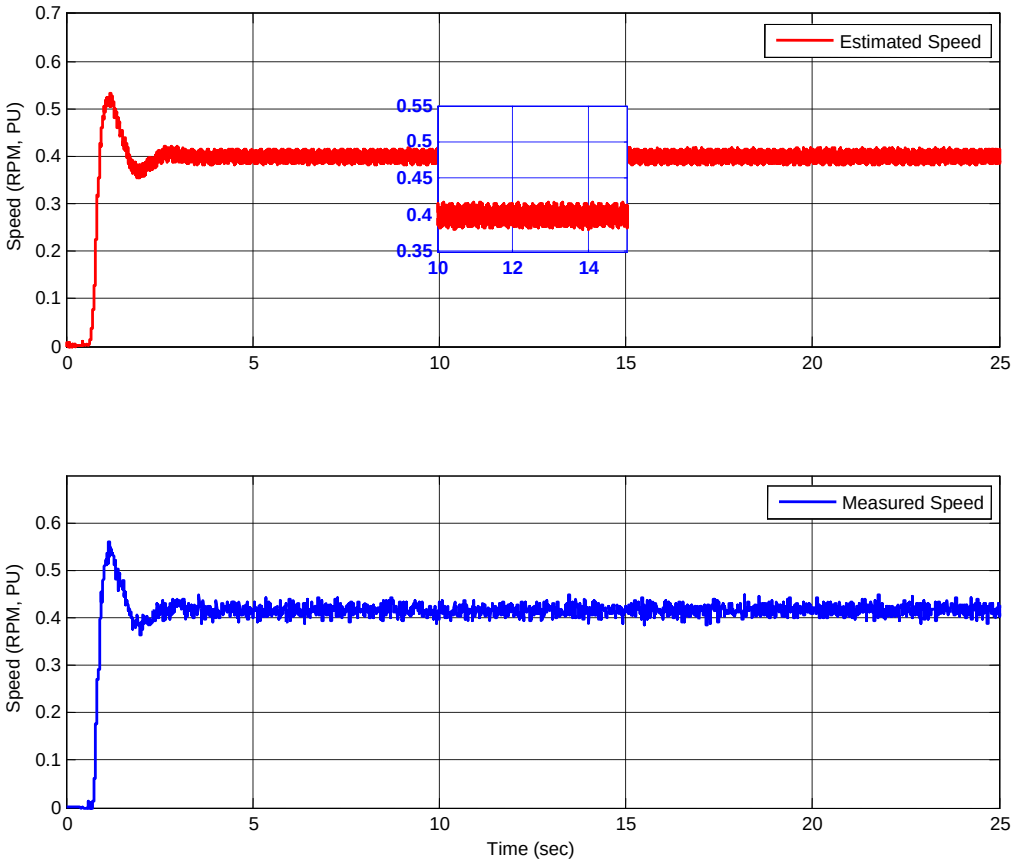

Figure 6. 4 Estimated and measured speed, adaptation mechanism gains set as $K_p = 4$ and $K_i = 400$.

The second set of PI gains were defined as $K_p = 4$ and $K_i = 400$. Figure 6.4 shows that the estimated speed started to exhibit some level of noise while the measured speed reached the steady state considerably faster than before. The settling time has decreased from 5.3858 seconds to 2.9934 seconds. However, even though the PO of the measured speed has dropped to 33.2819%, the measured speed started to deviate from the reference value where the steady state error of the measured speed is 5%.

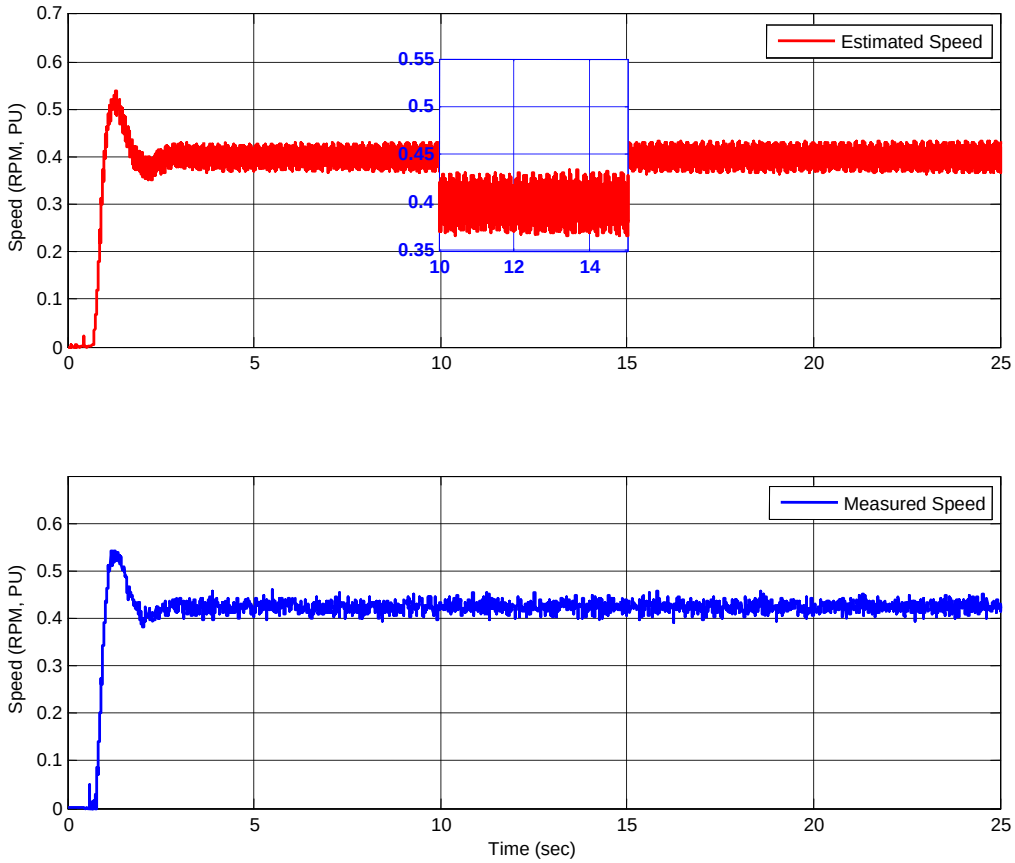

Figure 6. 5 Estimated and measured speed, adaptation mechanism gains set as K_p= 6 and K_i =600.

The third set of PI gains were defined as $K_p = 6$ and $K_i = 600$. Figure 6.5 shows a considerable increase in the magnitude of the displayed noise of the estimated speed, which has resulted in a larger speed deviation in the measured speed. The steady state error of the measured speed has risen from 5% to 7.5%. Similarly, referring to figure 6.4 from figure 6.5 indicates that the increase of the adaptation mechanism gains not only decreases the settling time, but also reduces the peak overshoot of the measured speed. The settling time of the measured speed has dropped from 2.9934 seconds to 2.565 seconds and the PO has dropped from 33.21819% to 26.15093%.

The fourth set of PI gains is configured as $K_p = 8$ and $K_i = 800$. Figure 6.6 displays a considerable increase of the exhibited noise in the estimated speed. This increase of PI gains has not only caused these oscillations to become more visible at the measured speed, but also caused the measured speed to greatly deviate from the reference speed, where the steady state error has increased to 17.5%. However, the increase of PI gains

has caused the settling time to drop to 1.8518 seconds and the PO to drop to 20.00621%.

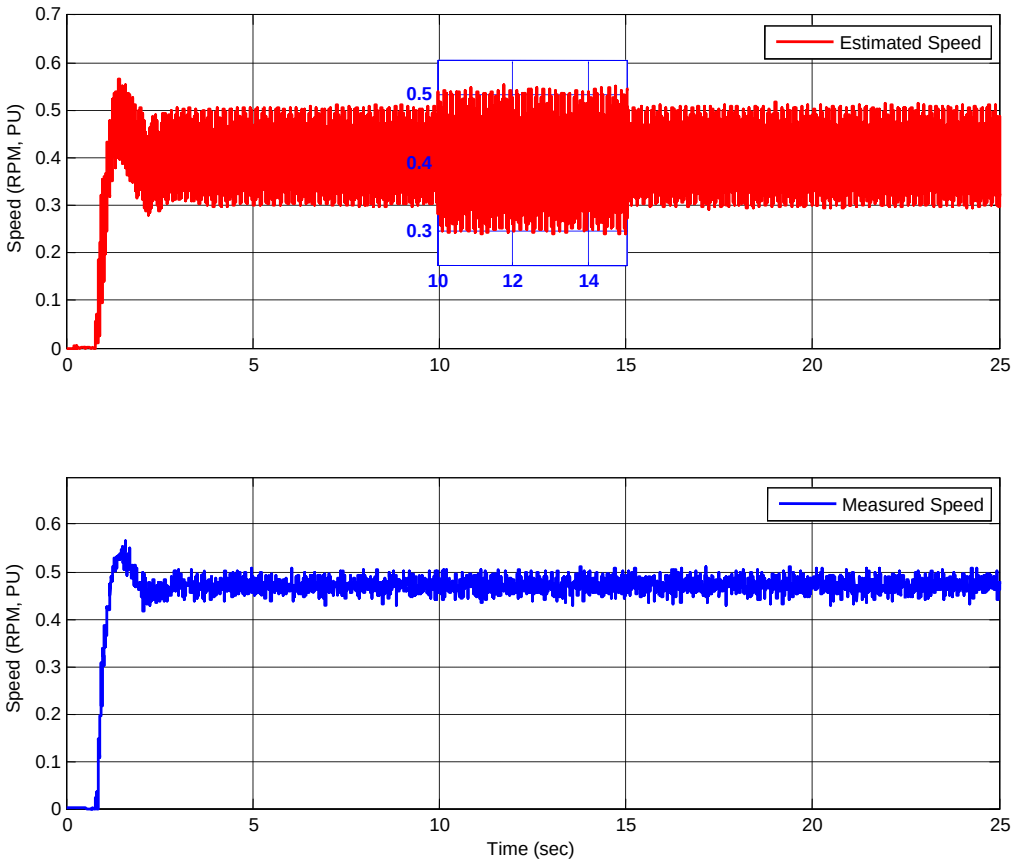

Figure 6. 6 Estimated and measured speed, adaptation mechanism gains set as $K_p = 8$ and $K_i = 800$.

The previous test has provided a distinct and detailed insight on how the value of the PI gains of the adaptation mechanism can radically influence the performance of the sensorless speed drive. This test revealed that while low PI gains enable the drive system to estimate the speed with a minute steady-state error, they increase the settling time, induce undesired oscillation during transient states and contain a relatively large peak overshoot. Furthermore, the step input speed test has also shown the ability of the high PI gains to improve the systems dynamic performance in terms of having a fast response, moderate peak overshoot, short settling time and no unnecessary oscillations. However, all of the aforementioned improvements are accompanied with a speed estimate that exhibits a high level of noise, which is amplified as the gain values are increased. Consequently, the generated noise forces the actual speed to deviate from the desired set speed and this deviation is translated into a significant steady state error.

6.3 Harmonic Analysis Using Fast Fourier Transforms

The FFT tool is utilised to display the frequency spectrum of the estimated and actual speed. These signals are captured in real-time during operation and then stored in Matlab's workspace as a structure with time variable. Since the drive system is discretised, the signals saved within this structure are sampled at a fixed-step and consequently satisfies the FFT tool requirements [67][78]. The FFT analysis is applied to investigate how the PI gains of the adaptation mechanism can influence the frequency components of the estimated and the measured speed. The frequency spectrum of both the estimated speed and the measured speed is analysed over the whole speed range. However, due to hardware limitation, speeds below 3% of the rated speed were excluded. The FFT related results are arranged as follows: figures 6.7, 6.10, 6.13 and 6.16 show a segment of the sampled speed signals, figures 6.8, 6.11, 6.14 and 6.17 display the frequency spectrum of the estimated speed, $\hat{\omega}_r$, and figures 6.9, 6.12, 6.15 and 6.18 display the frequency spectrum of the measured speed ω_r. These sampled speed signals were sampled during the steady state at a frequency of 10 kHz.

Four sets of PI gains have been selected to primarily demonstrate how the estimated speed is affected by the nature of these gains and secondarily to assess how the effects are translated within the measured speed.

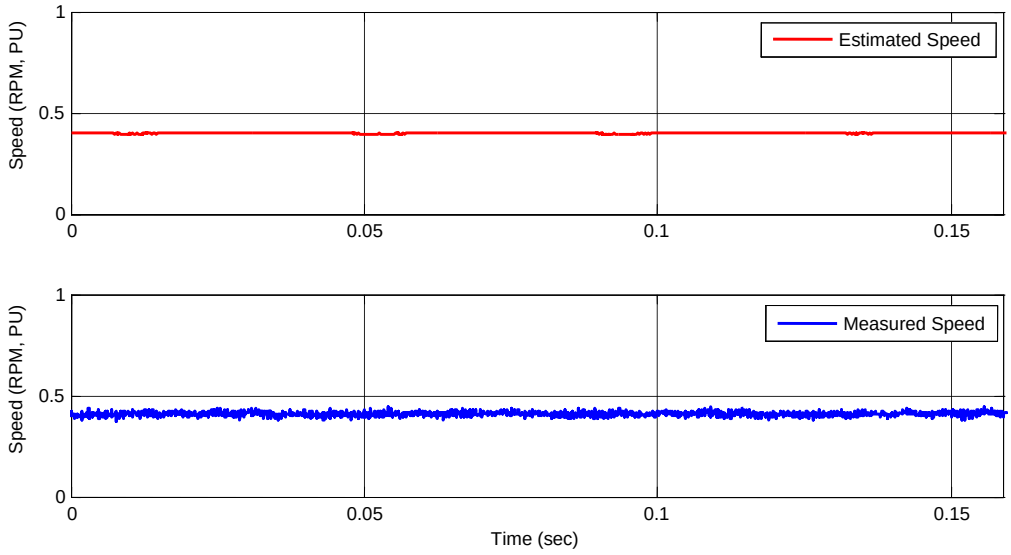

Figure 6. 7, Estimated and measured speed cross section, adaptation mechanism gains set as $K_p = 2$ and $K_i = 200$.

Starting with low PI gains, figure 6.7 shows a cross section of both the estimated speed and the measured speed when the PI gains were set to $K_p = 2$ and $K_i = 200$. Figure 6.7 also shows a smooth estimated speed and a measured speed that correctly follows the estimated speed.

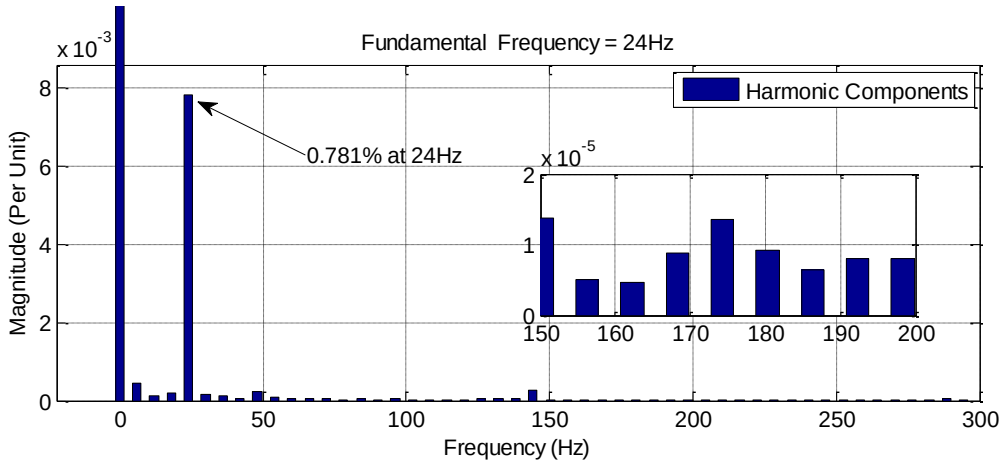

Figure 6. 8 Frequency spectrum of the estimated speed, adaptation mechanism gains set as $K_p = 2$ and $K_i = 200$.

The FFT analysis in figure 6.8 demonstrates that the presence of high-order harmonic components is insignificant when the content of the highest harmonic component is less than 0.002%, which is relative to fundamental component. However, there is a noticeable presence of components that oscillate with the fundamental frequency of operation.

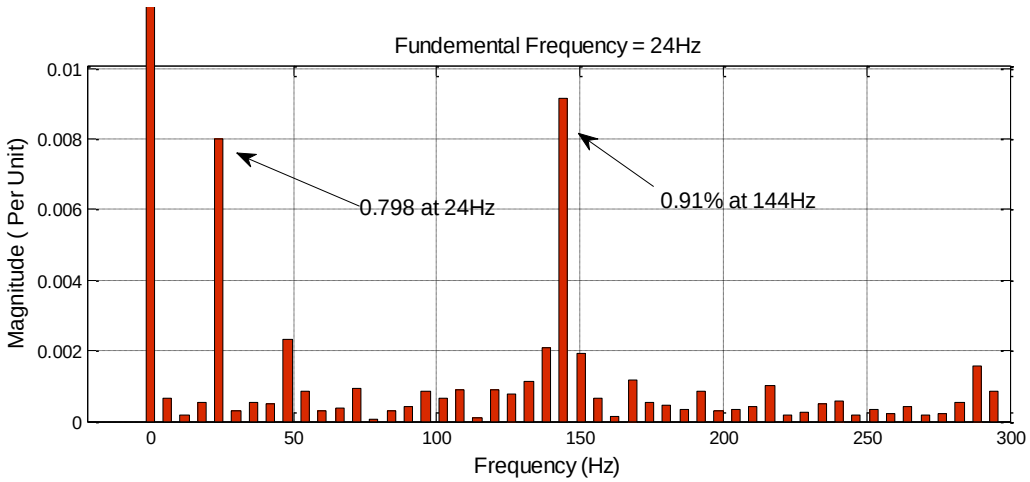

Figure 6. 9 Frequency spectrum of the measured speed, adaptation mechanism gains set as $K_p = 2$ and $K_i = 200$.

Likewise, figure 6.9 not only demonstrates that the presence of high-order harmonics is also negligible when the highest harmonic component is less than 0.3%, but also it shows that the presence of components that oscillate with the fundamental frequency with an almost equal magnitude to those components found in the estimated speed.

Figure 6.9 shows the presence of some frequency components that oscillate around the frequency of 144 Hz. Further investigation indicated that these were actually noise components generated by the encoder interface. The cause of these noise components can be attributed to the speed measurement circuits and the electrical noise associated with the use of an incremental encoder and its interface circuit [83]. This is also the reason why the harmonic components at the measured speed might seem to be comparatively higher than those found in the estimated speed.

The second set of PI gains were set as $K_p = 4$ and $K_i = 400$. Figure 6.10 shows that the estimated speed started to exhibit a slight oscillation, which is less visible in the measured speed. As it can be seen in figure 6.11, the magnitude of the frequency components oscillating with the fundamental frequency of 24 Hz, has noticeably increased from 0.781% to 1.47%, hence the semi-visible oscillations in the estimated speed. Nevertheless, the presence of high-order harmonic components is still insignificant when the highest harmonic component is less than 0.02%.

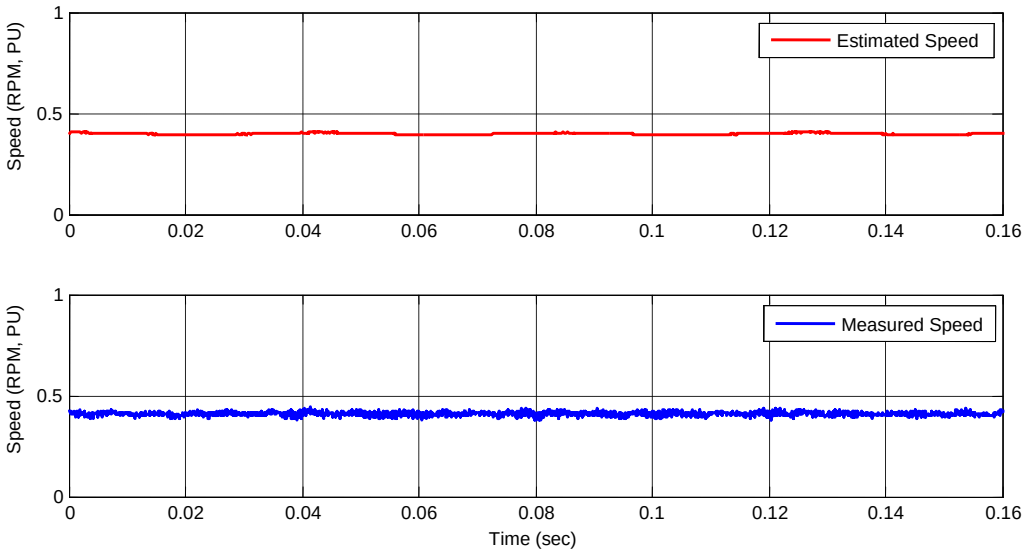

Figure 6. 10 Estimated and measured speed cross section, adaptation mechanism gains set as $K_p = 4$ and $K_i = 400$.

Even though Figure 6.12 demonstrates a slight increase in the magnitude of the high-order harmonics, their presence is still negligible when the highest harmonic component is less than 0.3%. Figure 6.12 shows a decrease in the frequency components at 24 Hz in the measured speed, which has decreased from 0.786% to 0.398%. This is inconsistent because the frequency components that oscillate with 24 Hz in the estimated speed has increased and is expected to have a comparative impact on the measured speed.

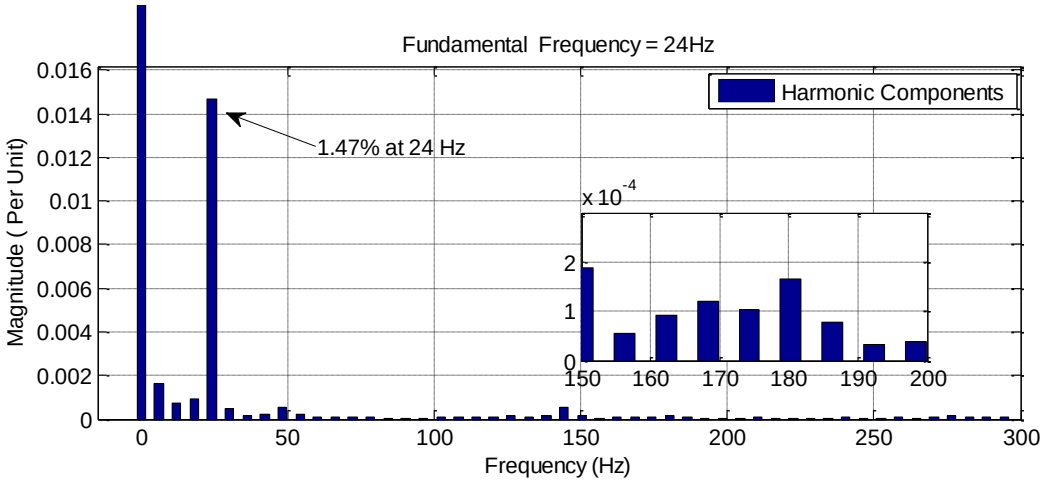

Figure 6. 11 Frequency spectrum of the estimated speed, adaptation mechanism gains set as $K_p = 4$ and $K_i = 400$.

Again, figure 6.12 shows the presence of the same noise components that oscillate around the frequency of 144 Hz with the same magnitude of the 0.91%, as with the previous set of PI gains.

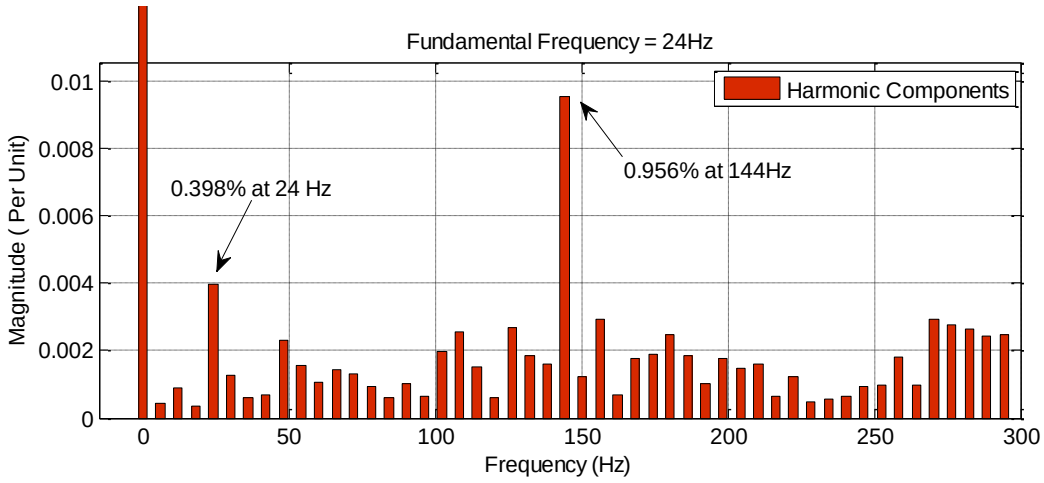

Figure 6. 12 Frequency spectrum of the measured speed, adaptation mechanism gains set as $K_p = 4$ and $K_i = 400$.

The third set of PI gains were set to $K_p = 6$ and $K_i = 600$. Figure 6.13 shows a considerable increase in the exhibited oscillation in the estimated speed, which is less visible in the measured speed. However, the measured speed has noticeably begun to deviate from the desired reference value, which constitutes a speed error.

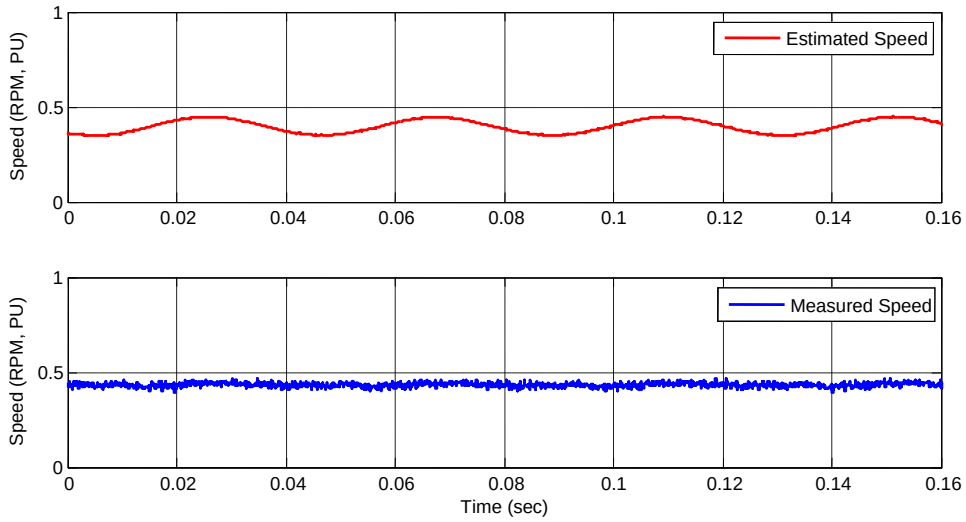

Figure 6. 13 Estimated and measured speed cross section, adaptation mechanism gains set as $K_p = 6$ and $K_i = 600$.

Figure 6.14 shows that the magnitude of the frequency components oscillating with the fundamental frequency 24 Hz, has substantially increased from 1.47% to 12.1%, which is the reason why the oscillations became more visible at the estimated speed. Yet, the presence of high-order harmonic components is still insignificant when the highest harmonics component is less than 0.04%.

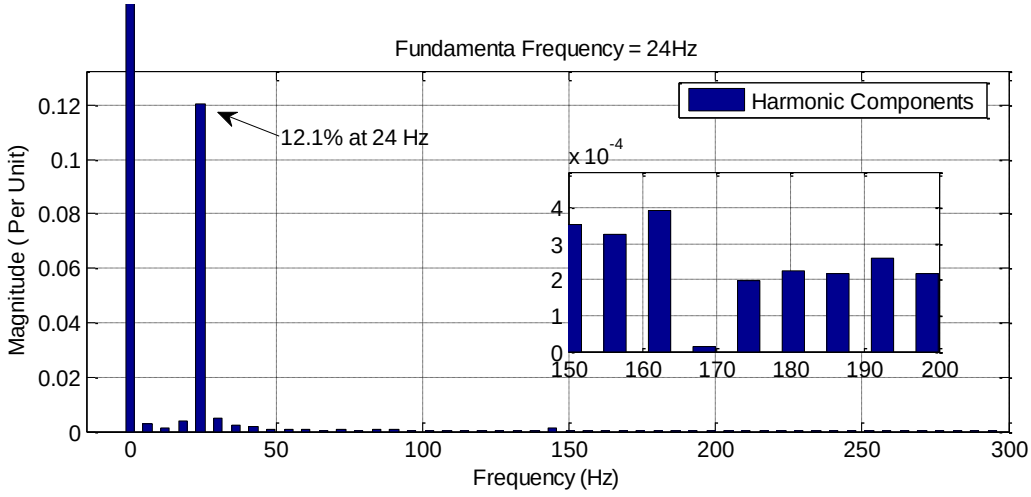

Figure 6. 14 Frequency spectrum of the estimated speed, adaptation mechanism gains set as $K_p = 6$ and $K_i = 600$.

Similar to figure 6.12, figure 6.15 demonstrates a slight increase in the magnitude of the high-order harmonics. However, their presence is still negligible when most of the harmonic components are under 0.5%. Figure 6.17 also shows an increase of the 24 Hz frequency components in the measured speed, which have increased from 0.398% to 1.4%.

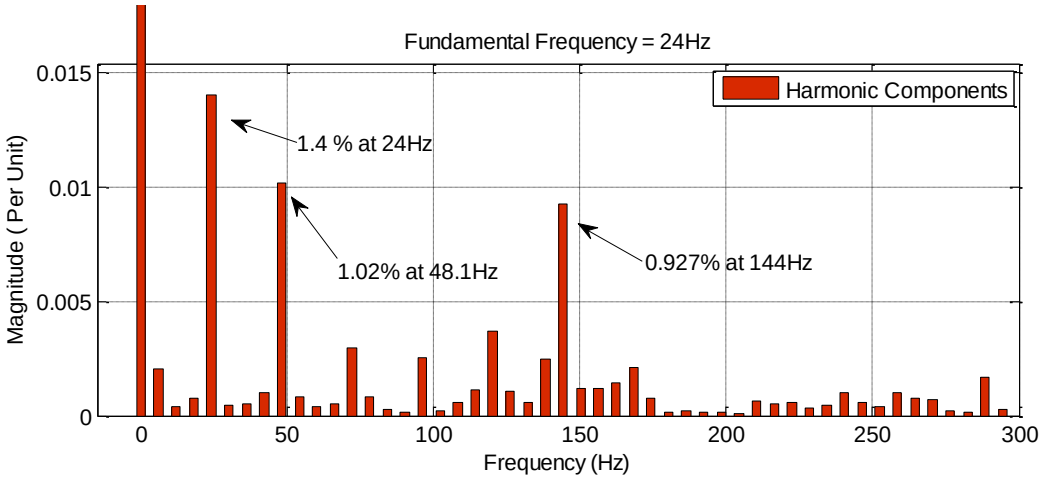

Figure 6. 15 Frequency spectrum of the measured speed, adaptation mechanism gains set as K_p= 6 and K_i =600.

Figure 6.15 shows the presence of the same noise components that oscillate around the frequency of 144 Hz with almost the same magnitude of the 0.927% characteristic as observed with the previous set of PI gains. Additionally, figure 6.17 shows some other noise components at a magnitude of 1.02% and a frequency of 48.1 Hz, which can also be attributed to electrical noise associate to the encoder interface.

The fourth set of PI gains were configured to be $K_p = 8$ and $K_i = 800$. Figure 6.16 displays a considerable increase in the exhibited oscillation in the estimated speed, which now clearly oscillate with a frequency of 24 Hz. This increase of PI gains has not only caused these oscillations to become more visible at the measured speed, but also caused the measured speed to greatly deviate from the reference speed.

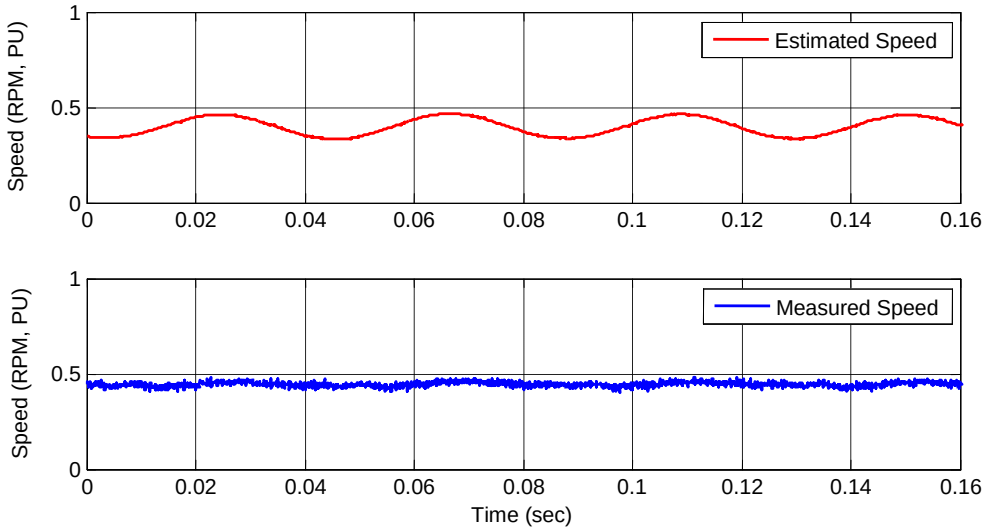

Figure 6. 16 Estimated and measured speed cross section, adaptation mechanism gains set as $K_p = 8$ and $K_i = 800$.

With respect to the harmonics components, even though it was observed in the previous section that the high gains cause the estimated speed to exhibit high level of noise, figure 6.17 shows only a significant increase in the magnitude of the 24 Hz fundamental frequency components. Moreover, it shows almost no increase in the magnitude of the high-order harmonics from the last set of PI gains.

Likewise, figure 6.18 demonstrates a slight increase in the magnitude of the high-order harmonics. However, their presence is still negligible when most of the harmonic components are under 0.05%. Figure 6.18 also shows an increase of the 24 Hz frequency components in the measured speed, which has increased from 1.4% to 2.23%.

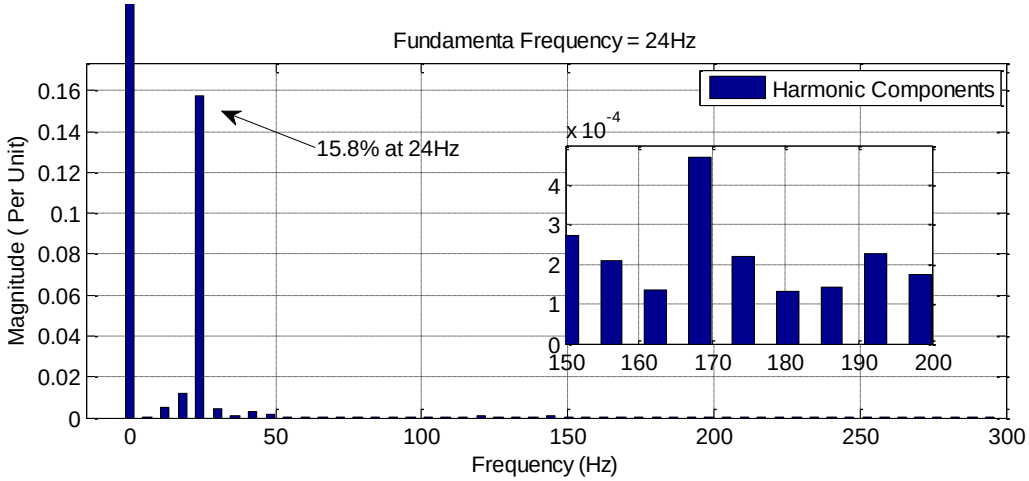

Figure 6. 17 Frequency spectrum of the estimated speed, adaptation mechanism gains set as $K_p = 8$ and $K_i = 800$.

Figure 6.18 shows the presence of the same noise components that oscillate around the frequency of 144 Hz with almost the same magnitude of the 0.794% as with the previous set of PI gains. Figure 6, 18 also shows some other noise components with a magnitude of 1.26% and a frequency of 48.1 Hz that can also be attributed to electrical noise associated to the encoder interface.

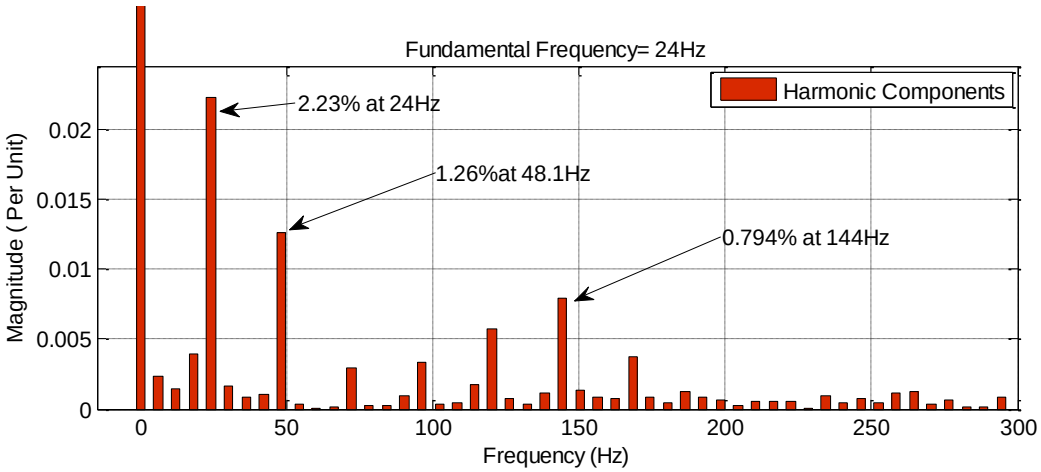

Figure 6. 18 Frequency spectrum of the measured speed, adaptation mechanism gains set as $K_p = 8$ and $K_i = 800$.

In the context of sensorless speed control, particularly in an MRAS based system, the novel harmonic analysis achieved by performing the fast Fourier transform is proven to be exceptionally beneficial. This has provided a unique overview into the relationship between the PI gains of the adaptation mechanism and the generation of ripple in the estimated speed. The harmonic analysis has not only shown that increasing the value of the PI gains also increases the magnitude of the generated ripple in the estimated speed, but has also revealed that the frequency of the generated ripple is synchronised with the stator frequency. More importantly, analysing the frequency spectrum of the estimated speed has unequivocally shown that the presence of high-order harmonics in the estimated speed is insignificant.

The results obtained from the harmonic analysis, combined with the results obtained in section 6.2, have revealed that the selection of PI gains bears an inherent compromise between achieving a robust dynamic response and achieving correct speed estimation. Selecting low PI gains avoids the excessive generation of ripple in the estimated speed and minimises the deviation of the measured speed from the reference speed. However,

it causes the speed response to become oscillatory during transient states and increases the time in which the speed signal settles. In contrast, while selecting high PI gains has shown to achieve fast speed convergence, the speed estimate will inadvertently contain a high level of noise that consequently compels the measured speed to deviate from the reference speed.

In practice, it is essential for the sensorless speed drive to not only be capable of estimating the actual speed effectively, but to be also capable of achieving a fast speed convergence as well as being dynamically robust. The appeal of encompassing the positive attributes of both the low PI gains and the high PI gains, while avoiding their negative side effects, validates the need for creating a PI based adaptive scheme that achieves the best balance between the abovementioned attributes.

6.4 Summary

This chapter has presented and discussed the results that were acquired during the experimental investigation into the performance of the MRAS based sensorlees drive. The experimental investigation was divided into two parts. The first part of the investigation was dedicated to explore the correlation between the PI gains of the adaptation mechanism and the generation of noise in the estimated speed. The second part of the investigation was dedicated to looking at the frequency spectrum of the generated noise through performing detailed harmonic analysis. To detail this investigation further, it has been shown that that the values of the PI gains in the adaptation mechanism are increased, the presence of ripple in the estimated speed becomes more potent. As a result of the gains increase, the ripple magnitude will amplify and in turn causes the actual speed to further deviate from the reference value. It has also been shown that the ripple components are sinusoidal in nature and oscillate with the stator frequency. Moreover, harmonic analysis has shown that an adaptation mechanism with neither low PI gains nor high PI gains causes the presence of high-order harmonics in the estimated speed to become significant.

Chapter 7 - Implementation of the Proposed "adaptive" Adaptation Mechanism

In order to generate the estimated speed $\hat{\omega}_r$, the adaptation mechanism is essentially driven by the states error (ε_ψ), which is essentially the difference between the states of the reference model and the adaptive model as described in chapter 3. The correct design of the adaptation mechanism not only ensures the overall stability of the estimation system, but also ensures that the estimated quantity will converge to the desired value with suitable dynamic characteristics. As discussed in chapter 3, the application of Popov's hyperstability criterion yields an MRAS system that contains a PI controller based adaptation mechanism. According to this criterion, the states error equations of the MRAS are guaranteed to be globally and asymptotically stable [53] [55] [56] [68].

The dynamic performance of the MRAS speed identification has been extensively analysed and tested. Moreover, it has been observed that the PI based adaptation mechanism helps the speed estimation system to track the actual motor speed with an achievable bandwidth, which can only be limited by noise, meaning that the PI gains should be as high as possible [10] [11] [12]. As a result, while the high PI gains help in achieving an excellent dynamic performance and fast response, they also cause the estimated speed to exhibit a high level of noise.

It has been established in section 6.2 that by increasing K_p and K_i, the estimated speed became noisier, plus the generated noise caused the actual speed to deviate from the desired reference speed. In addition, section 6.3 demonstrated that even though the presence of high-order harmonics components was insignificant, as the gains of the PI controller are increased the amplitude of the noise components oscillating with the fundamental frequency is also increased. In an attempt to remove some of the noise components in the estimated speed, the authors in [34] and [45] resorted to using a low pass filter in order to remove some of the noise components. The author in [34] was

testing an MRAS based speed estimator that employed a conventional PI as an adaptation mechanism. The author in [45] was testing an MRAS based speed estimator that employed an adaptation mechanism that was based on a sliding mode control. As one might expect, the use of filters in general has an inherent drawback, which is the imposition of time delay and its effect on the time response of the system. By implementing a low pass filter, a compromise has to be made between obtaining a smooth speed estimate and a delayed response. In most cases, the time-constant of the low pass filter is chosen in such a way that the estimated speed is smooth and the time delay is reasonably small.

As it was shown in sections 6.2 and 6.3, on the one hand, the benefit of having low PI gains is that the estimated speed will be free of high levels of noise and the actual speed follows the desired value set by the reference speed. On the other hand, the dynamic response during transient states is compromised. The benefit of having high PI gains is that the system's response will be fast and the dynamic performance will be robust. However, as stated and verified, the estimated speed will carry high level of noise that will cause the actual speed to deviate from the desired reference speed.

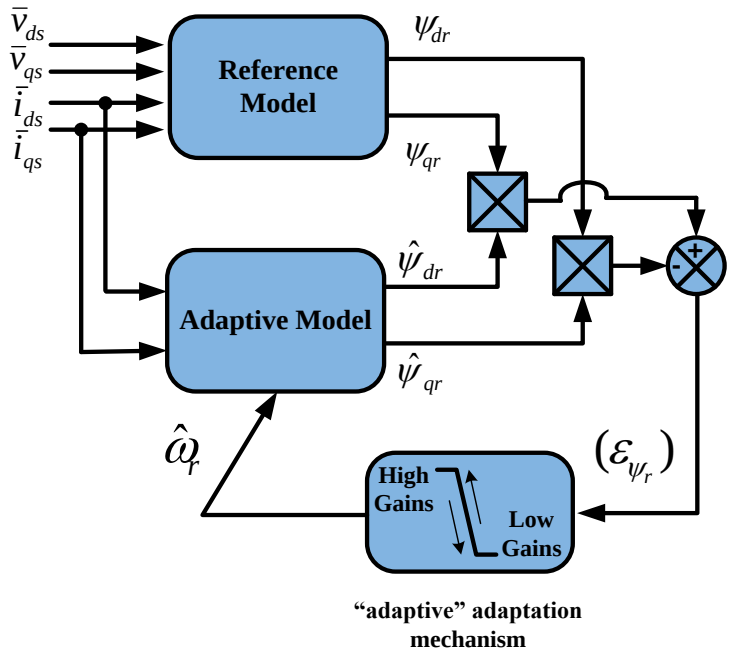

Figure 7. 1 MRAS with the proposed "adaptive" adaptation mechanism.

The proposed adaptive algorithm for the adaptation mechanism takes advantage of those aforementioned positive features and overcomes the shortcomings of having low PI gains and the noise that is the by-product of selecting a high PI gain. Figure 7.2 shows the algorithm's flow chart, which explains how it functions.

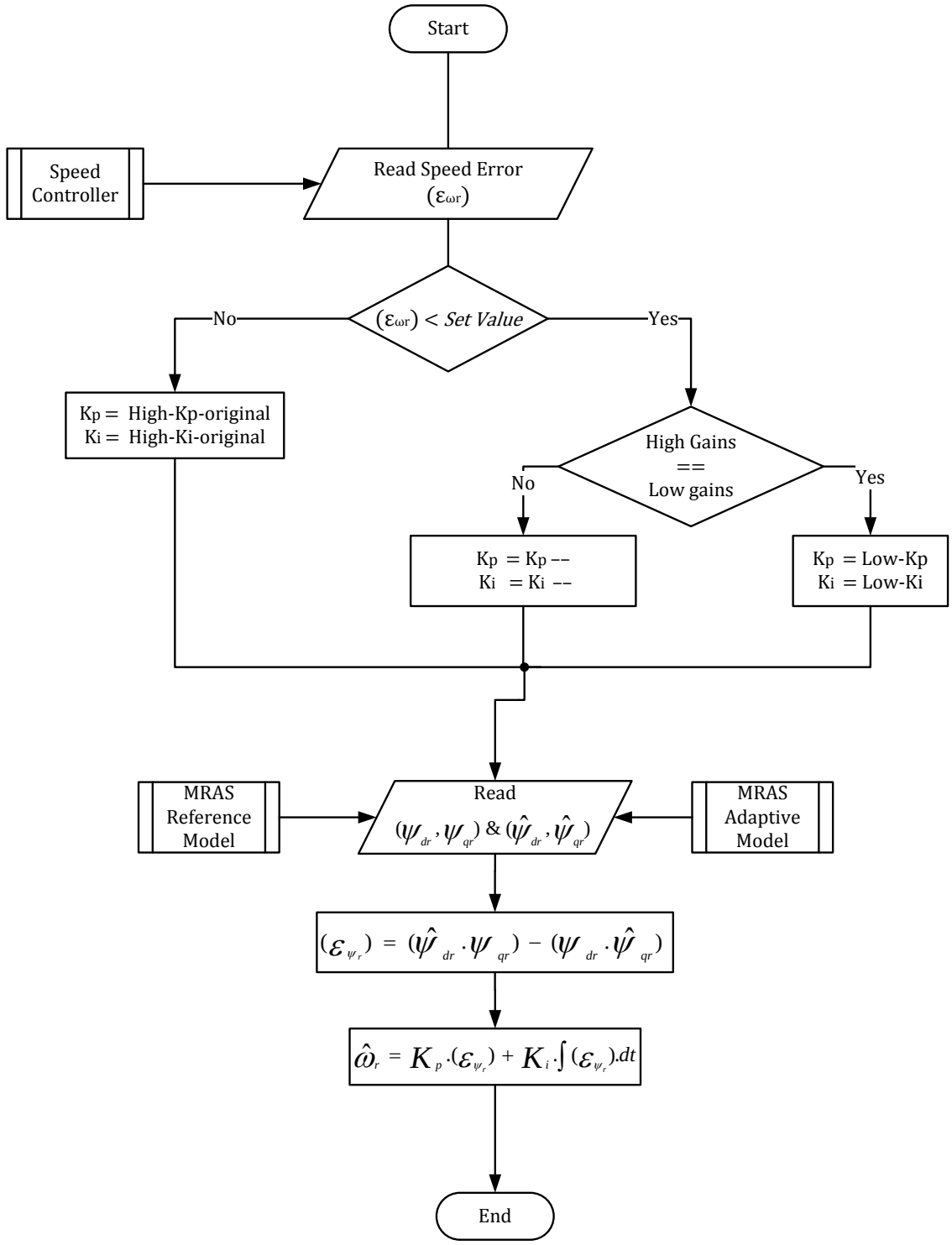

Figure 7. 2 Flow chart of the proposed adaptive algorithm.

The developed algorithm enables the PI controller in the adaptation mechanism to switch between high and low gains according to the operational conditions. The algorithm utilises the speed error ($\varepsilon_{\omega r}$) as an indicator to whether or not the estimated speed is starting to converge to the desired value of the reference speed. Once the estimated speed starts to converge, the algorithm starts to gradually decrease the high PI gains until they reach the low PI set values. It was observed during the experimental testing that changing from high to low gains need to be gradual otherwise the systems becomes unstable. However, an instantaneous change from low gains to high gains doesn't seem to cause any issues in respect to the systems performance. Hence, only the high gains are changed gradually to low gains when required. It can be seen from the flow chart in figure 7.2 that the algorithm begins by evaluating the speed error ($\varepsilon_{\omega r}$) and then it decides accordingly when to change the gains of the adaptation mechanism from high to low and vice versa. Once the appropriate gains selection has been achieved, the algorithm continues by reading the state variables in order to calculate the states error(ε_{ψ}), executing the PI code to generate the estimated speed ($\widehat{\omega}_r$). Figures 7.3 to 7.10 show the developed algorithm in action and they demonstrate how an improved speed control is attained.

For illustrative purposes, the lowest and the highest sets of PI gains tested in section 6.2 are used in the proposed adaptive algorithm in order to demonstrate independently, how the same low PI and high PI gains can respectively increase the settling time and the steady state error. However, when combined, they can overcome their negative traits and achieve a fast response with the smallest steady state error possible.

7.1 Implementation of the Proposed Modification under No-load Operations

The modified sensorless drive's performance that utilises the proposed adaptive algorithm as an adaptation mechanism was compared against the unmodified sensorless drive's performance, which essentially implements a conventional PI as an adaptation mechanism. Respectively, figure 7.3 compares the estimated speeds of the senseless drive acquired while applying adaption mechanisms with a low PI gains, high PI gains and an adaptive algorithm based PI.

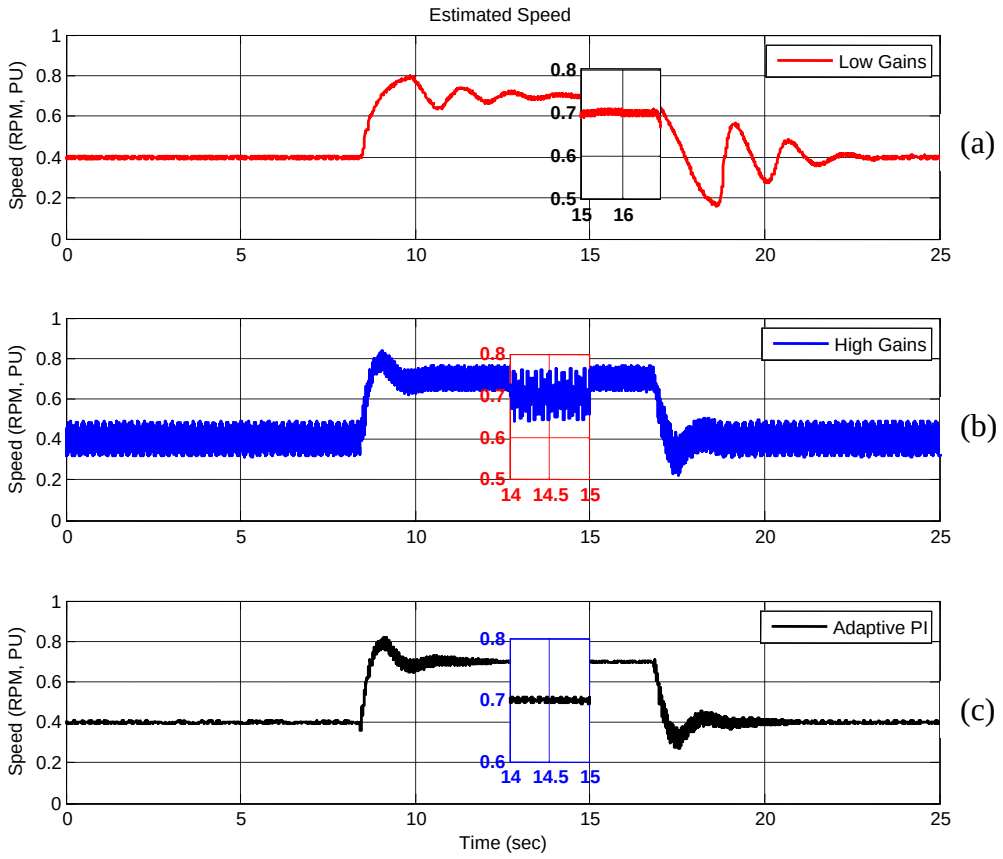

Figure 7. 3 Proposed algorithm's performance during a step-up speed change, no-load operation, estimated speed ($\hat{\omega}_r$).

Initially, the comparison was carried out while imposing a step-up speed change to demonstrate the system's behaviour during transient operations under no-load conditions. Figure 7.3 reiterates what was established in section 6.2 showing that low PI gains do not cause the estimated speed to exhibit high level of noise but instead, causes it to converge comparatively slowly to the desired speed value. It also shows how the high PI gains cause the estimated speed to exhibit a high level of noise while achieving fast convergence. Figure 7.3 clearly shows how the adaptive algorithm makes the estimated speed rapidly converge to the desired value without generating a high level of noise, particularly after the full convergence speed has been obtained. The advantage of this scheme can be observed by looking on how the actual speed is affected. Figure7.4 shows how the adaptive algorithm compels the actual speed to closely follow the reference value with almost no steady state-error, while still maintaining a fast dynamic response.

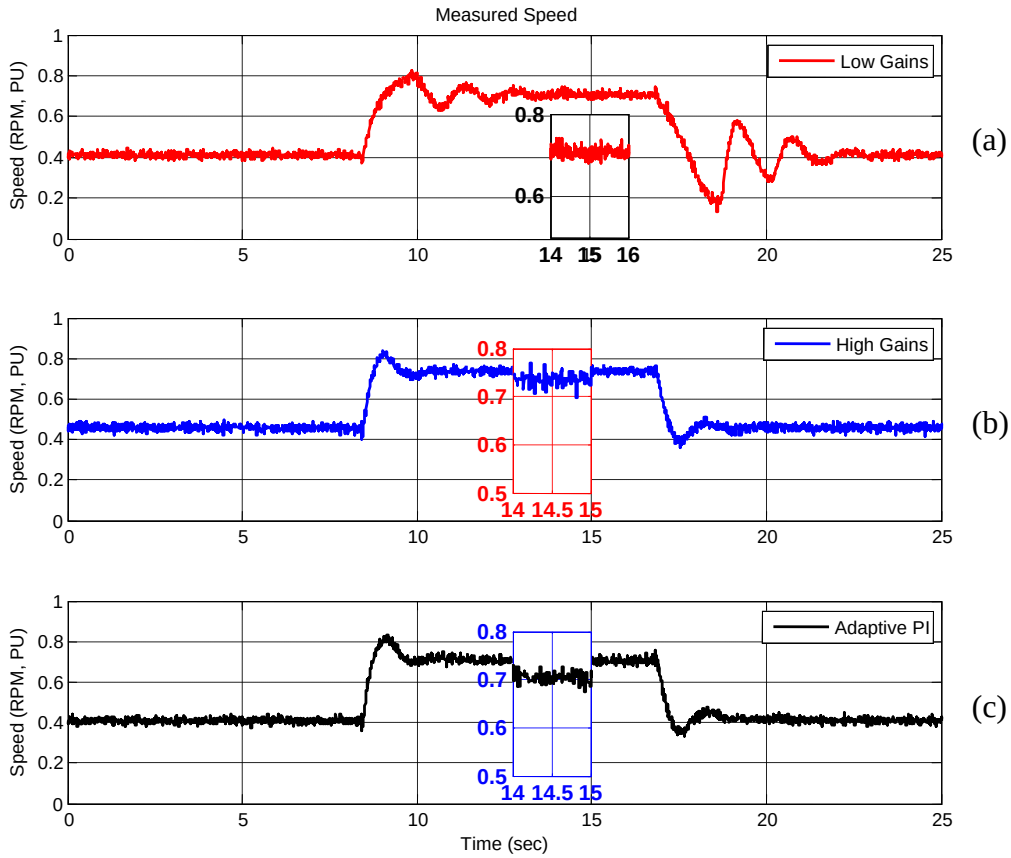

Figure7. 4 Proposed Algorithm's Performance during a Step-up Speed Change, no-load Operation, Measured Speed

The advantage of the proposed adaptive scheme is also verified by comparing its performance against the performance of the static adaptation mechanism. The performance comparison is established by comparing the response characteristics of the measured speed in terms of speed of convergence and the extent of speed deviation from the reference speed. The speed of convergence is assessed by measuring the settling time of the speed signal, and the speed deviation is assessed by measuring the steady state error.

Table 7.1 Performance comparison during a step-up speed change

Measured Speed Characteristics No-load Operation	Low Gains Adaptation Mechanism	High Gains Adaptation Mechanism	Proposed Adaptive Adaptation Mechanism
Settling Time ts (s)	3.71 (s)	2.10 (s)	1.83 (s)
Steady-state Error	2.02%	5.71%	2.02%

From Table 7.1 it can be seen that the proposed adaptive scheme has managed to cut the settling time by almost 50% in comparison to the low gains adaptation mechanism, while successfully avoiding the increase of the steady-state error in the measured speed.

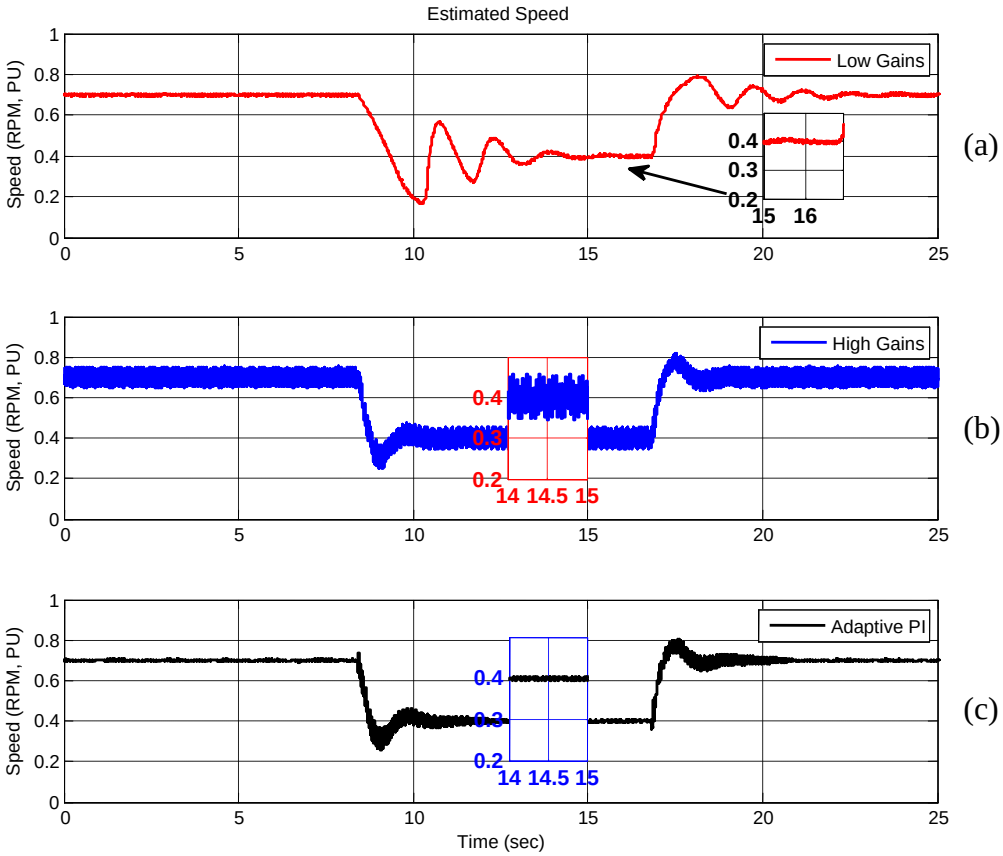

Figure 7. 5 Proposed algorithm's performance during a step-down speed change, no-load operation, estimated speed ($\hat{\omega}_r$).

Similarly to figures 7.3 and 7.4, figures 7.5 and 7.6 also validate the performance of the proposed adaptive algorithm. The only difference is that the performance of the drives response is tested during a step-down speed change. Again figure 7.5 and 7.6 demonstrate the advantage of utilising the proposed algorithm.

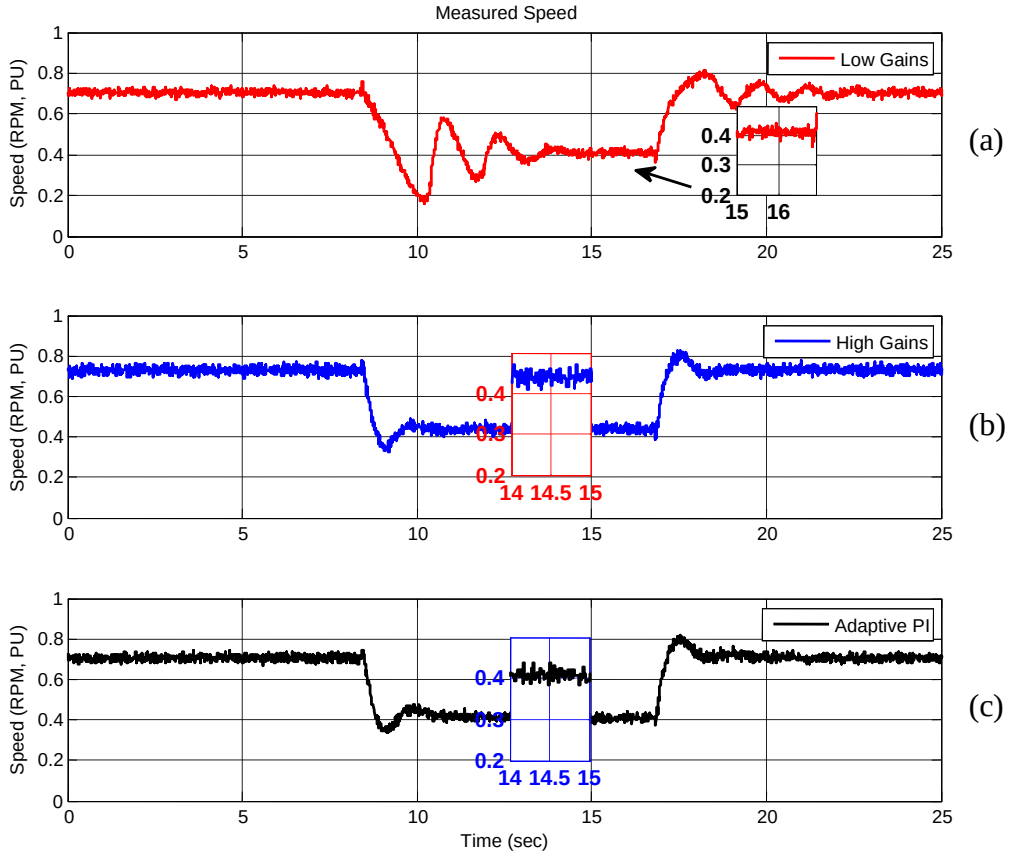

Figure 7. 6 Proposed algorithm's performance during a step-down speed change, no-load operation, measured speed.

Table 7.2 shows that during step-down speed change the proposed adaptive scheme has managed to cut the settling time by almost 43.77% in comparison to the low gains adaptation mechanism while again, successfully avoiding the increase of the steady state error of the measured speed.

Table 7.2 Performance comparison during a step-down speed change.

Measured Speed Characteristics No-load Operation	Low Gains Adaptation Mechanism	High Gains Adaptation Mechanism	Proposed Adaptive Adaptation Mechanism
Settling Time ts (s)	5.62 (s)	2.92 (s)	3.16 (s)
Steady-state Error	2.15%	9.18%	1.23%

7.2 Implementation of the Proposed Modification under Loaded Operations

The functionality of the proposed algorithm was also validated under loaded conditions where 50% of the rated load was continuously exerted onto the induction motor. Similar to the no-load conditions, the performance of the modified sensorless drive was tested against the unmodified one. Figures 7.7 to 7.10 show how the developed algorithm improves the speed estimation and also enhanced dynamic performance of the speed control.

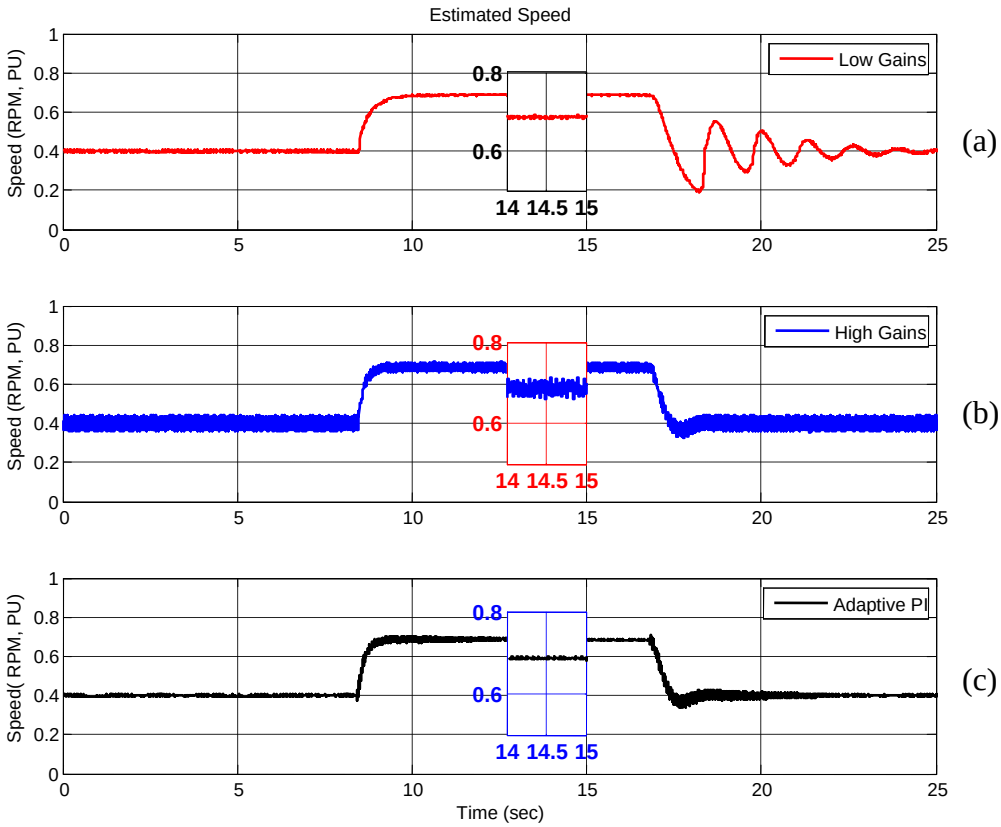

Figure 7. 7 Proposed algorithm's performance during a step-up speed change, loaded operation, estimated speed ($\hat{\omega}_r$).

Figure 7.7 shows that during a step-up speed change, the adaptation mechanism with low PI gains will achieve a correct speed estimate with a relatively fast convergence, where the settling time is 0.73 seconds. The speed estimate is smooth and it doesn't exhibit any high level of noise. Also indicated in figure 7.7 is how the speed estimate converges comparatively faster as a result of the high PI gains, where the settling time is approximately 0.49 seconds. Additionally, we can observe that due to the mechanical exertion of load on the induction motor, the magnitude of the exhibited noise is attenuated slightly in comparison to the noise level observed during the no-load operation in figure 7.3.

Figure 7.7 further validates the superiority of the modified adaptation mechanism; even when a mechanical load is exerted, a fast converging speed is clearly shown. The modified adaptation mechanism also demonstrates that it can generate a speed estimate that is free of high level noise, especially after full convergence is realised.

The advantage of implementing the modified adaptation mechanism can also be observed during the loaded operation by monitoring how an improved speed control is accomplished. Figure7.8 shows how the adaptive algorithm makes the actual speed closely follow the reference value while maintaining fast dynamic response.

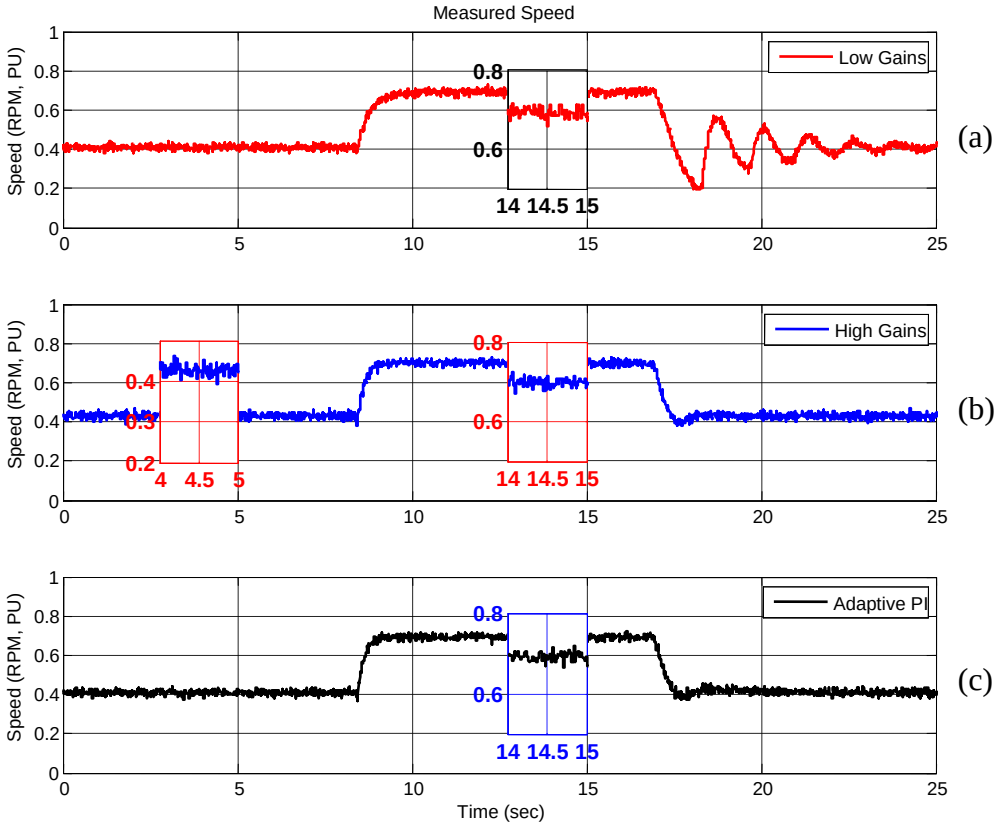

Figure 7. 8 Proposed algorithm's performance during a step-up speed change, loaded operation, measured speed.

Table 7.3 Performance comparison during a step-up speed change.

Measured Speed Characteristics Loaded Operation	Low Gains Adaptation Mechanism	High Gains Adaptation Mechanism	Proposed Adaptive Adaptation Mechanism
Settling Time ts (s)	0.83 (s)	0.58 (s)	0.55 (s)
Steady-state Error	1.43%	0.71%	0.86%

In the step-up speed change and during the loaded operation, Table 7.3 Show that when the low gains adaptation mechanism was employed, the measured speed reached the steady state region rather fast with a settling time of 0.83 seconds, which is relatively fast in comparison to the 3.71 seconds that was achieved during the no-load operation. Likewise, table 7.3 not only shows that even when the high gains adaptation mechanism was employed that the settling time was also fast, but also the steady state error has dropped by 29.13% compared to the no-load operation.

The decrease in the settling time and the reduction in the steady state error are attributed to the mechanical damping imposed by the load exertion, which suppresses any excessive oscillation in the speed signal during transit and also acts like a filter that minimises the current ripple. This in turn reduces the ripple transfer to the estimated speed. Table 7.3 also demonstrates that when the proposed adaptive scheme is implemented, a faster settling time is achieved with a steady state error, which is less than 1%.

The implementation of the modified PI algorithm becomes particularly advantageous during a step-down speed change during load exertion; because when a sudden reduction in speed demand occurs, this will cause the speed to oscillate for a relatively long period of time before it settles and converges to the desired value. The low gain aspect of figure 7.9 demonstrates this aforementioned condition. While it can be observed that the high PI gains assist in overcoming this oscillation condition, the consequent cost is a noisy speed estimate that forces the actual speed to deviate from the desired value as it can be observed in the corresponding part of figure 7.10.

The modified adaptation mechanism consistently improves the drives performance during a loaded operation when an unexpected step-down speed change is imposed. The adaptive PI in figure 7.9 corroborates the functionality of the proposed modification, by not only generating an enhanced speed estimate, but also by assisting the sensorless drive to fulfil its purpose through achieving a correct speed control, which can be observed in figure 7.10.

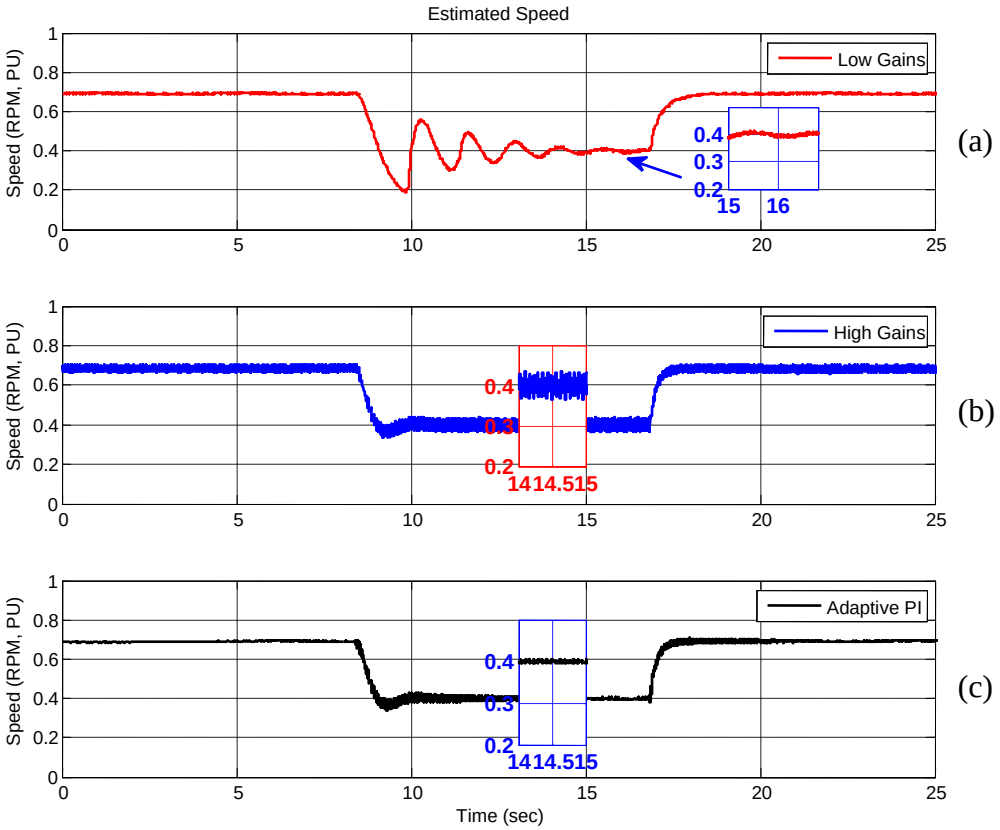

Figure 7. 9 Proposed algorithm's performance during a step-down speed change, loaded operation, estimated speed ($\hat{\omega}_r$).

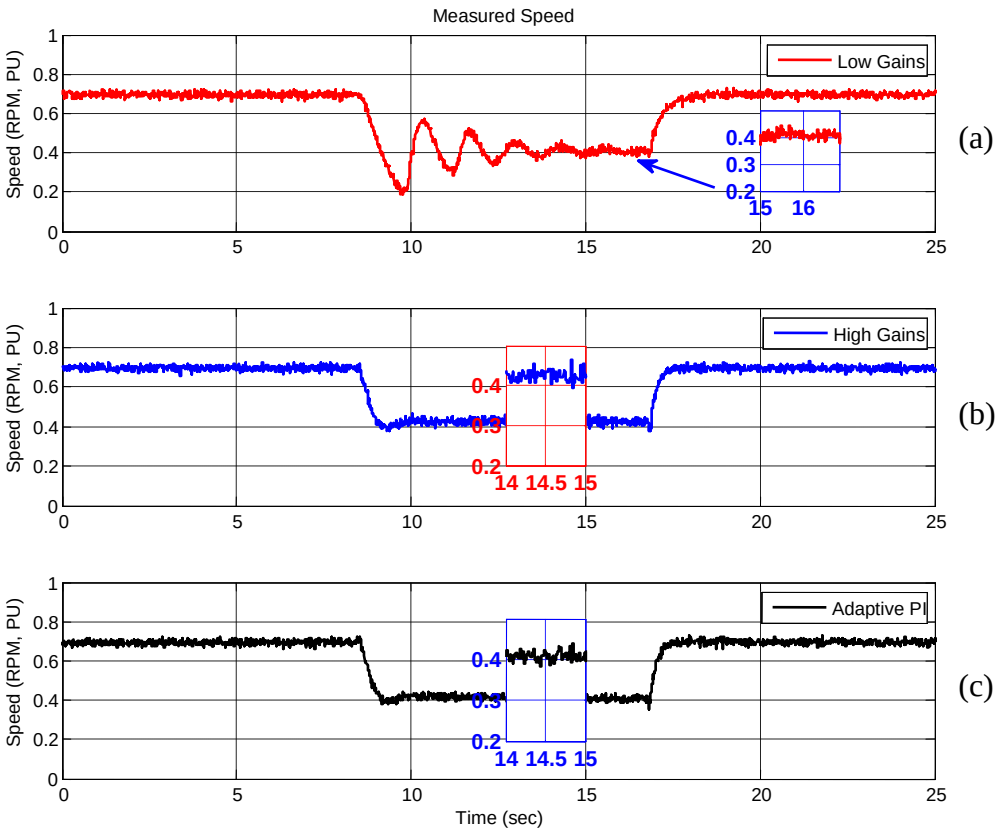

Figure 7. 10 Proposed algorithm's performance during a step-down speed Change, loaded operation, measured speed.

Table 7.4 illustrates that by implementing the proposed adaptive scheme the settling time of the measured speed is 2.28 seconds which is 61.3% less than the settling time achieved by implementing the low gains adaptation mechanism. It can also be seen from the data in Table 7.4 that the proposed adaptive scheme offers the best performance in terms of achieving a fast convergence with minimum deviation. Furthermore, a 60.86% reduction is shown in the adaptive steady state error in comparison to the steady state error that was achieved by implementing the high gains adaptation mechanism.

Table 7.4 Performance comparison during a step-down speed change.

Measured Speed Characteristics Loaded Operation	Low Gains Adaptation Mechanism	High Gains Adaptation Mechanism	Proposed Adaptive Adaptation Mechanism
Settling Time ts (s)	5.89 (s)	1.845 (s)	2.28 (s)
Steady-state Error	2.5%	5.75%	2.25%

7.3 Summary

This chapter has presented a novel adaptation mechanism for an MRAS based speed estimator. The proposed adaptation mechanism replaces the fixed gains PI controller with an adaptive PI controller that adapts to the operational conditions, in order to achieve a robust response with fast and correct speed convergence. A thorough experimental comparison between the two adaptation schemes have been carried out using a direct vector control induction motor drive. The application of the new scheme shows an improved transient performance and steady state performance. The performance of the proposed adaptive scheme is verified under both no-load and loaded conditions.

Chapter 8 - Conclusion and Further Work

The research presented in this thesis has examined the performance of a sensorless vector control drive built on a rotor flux-linkage based MRAS, particularly with respect to noise in the estimated speed. The main objective was twofold: firstly, to investigate how the PI controller gains of the adaptation mechanism can induce noise in the estimated speed, in addition to providing a detailed description that shows the ability of the adaptation mechanism gains to affect the speed estimation process and the drive's dynamic response; and secondly, to examine the harmonic spectrum of the generated noise in order to highlight its characteristics, conclusively revealing that the presence of high-order harmonics in the generated noise is insignificant. An adaptive algorithm has been developed and proven to be a suitable alternative to overcome the noise problem, while maintaining a robust dynamic response without the use of filters. The purpose of this chapter is to summarise the investigations and findings of this study, presenting conclusions and recommending various possibilities for future studies.

8.1 Conclusions

As depicted in chapter 1, the appeal of saving energy has led to the wide implementation of high-performance speed drives in applications where an accurate speed and position is not essential. Hence the relatively new found reliance on sensroless speed drives that facilitate a reduction of hardware complexity and cost. MRAS based sensorless schemes are the most common strategies in use due to their relative simplicity and ease of implementation. In the last two decades, an extensive amount of research has been carried out to improve the performance of MRAS based speed estimators, practically at low and near zero speed operations, during which various algorithms and solutions have been proposed. However, there is an issue that appears to have been acknowledged by significantly few research articles regarding the generation of high-order harmonics phenomenon in the estimated speed, which is caused by the gains of the adaptation mechanism that is based on a conventional PI controller. While this phenomenon has been identified many years previously, until now there has been neither a detailed description that neither gives credence to the existence

of such phenomenon nor an assessment of their influence on the drives sensorless performance.

Different types of MRAS based speed estimators have been developed and are categorised as conventional MRAS and AI based MRAS. In the category of conventional MRAS, the estimation techniques mainly differ with respect to what quantity is selected for adaptation purposes. While in the category of AI based MRAS, the estimation techniques vary based on the type of AI method used for estimation. The major issues associated with MRAS based speed estimators range from basic pure integration problems to variations of motor parameters. Different techniques presented in the literature to tackle these issues have been extensively reviewed in chapter 2.

The transformation of the three-phase induction machine into an equivalent two-phase machine based on the (d, q) transformation was explained in chapter 3. Chapter 3 also presents a step-by-step illustration of all of the axes transformations implemented in transforming a three-phase induction machine into a two-phase induction machine, with variables represented in the stationary reference. A conventional rotor flux-linkage based MRAS has been derived according to the induction machine (d, q) dynamic model. This scheme was originally developed by *Schauder* and is the most commonly used type of MRAS in speed estimation. An appropriate adaptation mechanism for rotor speed estimation was derived based on Popov's hyperstability criterion. This criterion produces a system with a stable and quick response, where the differences between the state variables are manipulated into a speed tuning signal, which in turn fed into a PI controller that generates the estimated rotor speed. Chapter 3 also presents the discrete-time representation of the modelled MRAS based system.

A Simulink® based investigative simulation was carried out on a sensorless vector control system that was built on rotor flux-linkage based MRAS. The purpose of the simulation was to clearly demonstrate how the PI gains of the adaptation mechanism can influence the dynamic performance of the drive system and speed estimation, while also applying a unique harmonic analysis to probe for any generation of noise and high-order harmonics. This noise and subsequent high-order harmonics may occur in the estimated speed as a result of the implementation of high adaptation gains. The simulation results have verified that high PI gains can help in achieving a better dynamic performance in terms of being fast and robust against load disturbance. The

harmonic analysis has revealed that there is neither a generation of noise nor high-order harmonics in either the estimated speed or the actual measured speed.

The hardware and the experimental setup designed to provide a robust testing platform for the practical implementation that was described in chapter 5. The experimental setup consists of a drive unit based on a three-phase inverter, a digital signal processing unit base on the **eZdsp™ F28335** development board and a motor test rig, consisting of a 120 Watt induction motor coupled with a DC motor and an incremental encoder.

Despite some limitations in the region of zero speed operations, conventional MRAS based speed estimators that normally use a fixed-gain PI controller in the adaptation mechanism, can deliver an excellent performance with ease of implementation. In spite of the considerable amount of research that has been carried out to improve the performance of conventional MRAS at low and zero speed, far little attention has been paid to either tackle the generation of ripples in the estimated speed, or even quantify their effect on the drives performance. Furthermore, it has been acknowledged that the generated ripples in the estimated speed consist of high-order harmonics. The purpose of chapter 6 was to firstly provide a detailed account showing in the real drive system that while a high PI gain in the adaptation mechanism can improve the drives dynamic performance, it can also cause the estimated speed to exhibit a high level of noise. Secondly, this investigation has illustrated how the generated noise ripples can cause the actual speed to deviate from the desired reference speed. Finally, conduct an examination into the harmonic spectrum of the generated noise to reveal its characteristics and essentially provide tangible evidence showing the insignificant presence of high-order harmonics in the generated noise.

In the experimental system, the discrete model of the rotor flux-linkage based MRAS was programmed in C language and implemented in real-time on the **eZdsp™ F28335** processing platform. The experimental testing was initiated by validating the sensorlesss performance of the drives by comparing the estimated speed against the actual measured speed provided by the speed measurement unit. The introductory test was performed on the vector control drive while operating in the closed-loop sensorless mode. The results have verified that the seonsorles drive is properly functional and accurate speed estimates were confirmed.

The second experimental test was conducted under no-load conditions and carried out by subjecting the motor to a step input while varying the PI gains of the adaptation mechanism. This was to observe the speed estimation performance of the sensorless drive under different PI gains. The results of this test have clearly shown that on the one hand, an adaptation mechanism with low PI gains can make the drive system achieve correct speed estimation with a minute steady state error. While on the other hand, these low gains prolong the settling time of the drives response, induce undesired oscillation during transient states and a relatively large peak overshoot. Furthermore, the test has also demonstrated the ability of the high PI gains to improve the systems dynamic performance in terms of reducing the settling time and comparatively minimising the peak overshoot with no unnecessary oscillations. However, all of the aforementioned improvements are accompanied with a speed estimate that exhibits a high level of noise that is amplified as the gain values are increased. Consequently, the generated noise ripples forces the actual speed to deviate from the desired set speed and the deviation is translated in a significant steady state error.

The third experimental test was to examine the harmonic spectrum of both the estimated and actual measured speed by applying the FFT in order to understand the nature of the generated noise and probe for any transfer of noise components from the estimated speed to the actual speed. The harmonic analysis results have shown that the magnitude of the generated noise ripples increases as the gains of the adaptation mechanism are also increased. Moreover, the harmonic analysis results have also revealed that the frequency of generated noise ripples are synchronised with the stator frequency. While there is evidence showing that there is a transfer of this noise from the estimated speed to the actual speed, this transfer is marginal. Furthermore and more importantly, analysing the frequency spectrum of the estimated speed has unequivocally shown that the presence of high-order harmonics in the estimated speed is insignificant.

A novel adaptive algorithm was successfully developed to replace the fixed-gains adaptation mechanism to overcome the generation of noise in the estimated speed without the use of filters. Chapter 7 explains the functionality of the developed algorithm. The developed algorithm take advantage of the positive attributes of the implementation of both low and high PI gains by shifting smoothly between low and high gains as the operational conditions dictate. Experimental tests were conducted to

test the drive's performance while implementing the new proposed adaptive scheme in real- time and compare it to the drive's performance while implementing an adaptation mechanism with a fixed-low gains PI and a fixed-high gains PI.

Under no-load conditions the new adaptive algorithm has displayed the best transient state performance during the step-up speed change, achieving the fastest settling time with a moderate peak overshoot, while achieving an improved steady state performance that is comparable to the steady state performance of the fixed-low gains PI. Similarly, during the step-down speed change, the new adaptive algorithm has displayed an excellent transient performance that is comparable to the transient performance of the fixed-high gains PI, while achieving the best steady state performance by exhibiting the smallest steady state error.

In loaded conditions, the new adaptive algorithm has displayed the best transient and steady state performance during the step-up speed change, achieving the fastest settling time and the smallest steady state error. Similar to the no-load operation during the step-down speed change, the new adaptive algorithm has displayed an excellent transient performance that is comparable to the transient performance of the fixed-high gains PI, while achieving the best steady state performance by again exhibiting the smallest steady state error.

In conclusion, the work published in this thesis has contributed to the existing knowledge by providing a distinct account, showing not only how the estimated speed in a real MRAS based sensorless drive can be affected by the adaptation mechanism gains, in terms of noise generation, but also demonstrates how the noise ripples influences the performance of the drive systems by forcing the actual speed to deviate from the reference speed. The study has also contributed to the existing knowledge by introducing an unprecedented harmonic analysis that revealed the nature of the generated noise within the estimated speed. More importantly, it has been clearly ascertained that the presence of high-order harmonics in the estimated speed is negligible. Furthermore, the study has also presented a new adaptive algorithm for the adaptation mechanism, which succeeds in avoiding the excessive generation of noise and simultaneously assists in achieving a fast and robust dynamic response.

8.2 Recommendations for further work

The work described in this thesis has investigated the performance of a rotor flux-linkage based MRAS in a sensorless speed drive. It has been demonstrated that an adaptation mechanism based on a PI controller can affect the response of a drive and also induce undesired noise ripples in the estimated speed. Thus, it will be noteworthy if a study is carried out to examine whether the more elaborate adaptation mechanisms that are based on fuzzy logic and neural networks can also induce noise ripples in the estimated speed. It will also be beneficial to integrate the harmonic analysis as a part of future research into MRAS based speed estimation, which will allow the tracking of any generation of noise and also understand its characteristics. With respect to testing the harmonic content of the estimated speed at very low speeds, there is neither a theoretical nor a technical reason to suggest that the PI gains of the adaptation mechanism will affect the frequency composition of the estimated speed any differently than what has been established with the experimental investigation. However, in order to be conclusive one might consider probing for high-order harmonics in the estimated speed at speeds lower than 3% rated speed.

References

[1] A. M. Trzynadlowski, *Control of Induction Motors*, 1 ed. Reno, Nevada: Academic Press, 2000.

[2] B. Jeftenić, M. Bebić, and S. Statkić, "Controlled multi-motor drives," in *International Symposium on Power Electronics*, 2006.

[3] P. Vas, *Sensorless Vector and Direct Torque Control*. New York: Oxford University Press, 1998.

[4] M. Yano and S. Abe, "History of Power Electronics for Motor Drives in Japan," in *IEEE Conference on the History of Electronics* Rutgers University, 2004.

[5] B. Drury, *The Control Techniques Drives and Controls Handbook* 2ed. London: The Institution of Engineering and Technology, 2009.

[6] B. K. Bose, *Power Electronics And Motor Drives: Advances and Trends*. London: Academic Press, 2006.

[7] M. H. Rashid, *Power Electronics Handbook* 3ed. Oxford: Butterworth-Heinemann Ltd, 2011.

[8] L. C. H. Madadi Kojabadi, and R. Doriaswami, "Recent progress in sensorless vector-controlled induction motor drives," in *2002 Large Engineering Systems Conference* Halifax Canada, 2002.

[9] J. W. Finch and D. Giaouris, "Controlled AC electrical drives," *IEEE Transactions on Industrial Electronics*, vol. 55, pp. 481-491, 2008.

[10] K. D. Hurst, T. G. Habetler, G. Griva, and F. Profumo, "Zero-speed tacholess IM torque control: simply a matter of stator voltage integration," *IEEE Transactions on Industry Applications*, vol. 34, pp. 790-795, 1998.

[11] J. Holtz and Q. Juntao, "Drift- and parameter-compensated flux estimator for persistent zero-stator-frequency operation of sensorless-controlled induction motors," *IEEE Transactions on Industry Applications*, vol. 39, pp. 1052-1060, 2003.

[12] M. S. Rashed, A. F., "A stable back-emf MRAS-based sensorless low-speed induction motor drive insensitive to stator resistance variation," *Electric Power Applications, IEE Proceedings*, vol. 151, pp. 685-693, 2004.

[13] B. K. Bose, *Modern Power Electronics and AC Drives*, 1 ed. New Jersey: Prentice Hall 2001.

[14] M. F. Moussa, Y. Gaber, and M. El Attar, "Vector control drive of permanent magnet motor without a shaft encoder," in *Power System Conference, MEPCON 2008. 12th International Middle-East*, 2008, pp. 249-254.

[15] Elektromaschinen, und, and Antriebe, "High Speed Drive," available at http://www.highspeeddrive.org/#Introduction Retrieved: March 2013.

[16] J. Holtz, "Sensorless Control of Induction Machines With or Without Signal Injection?," *IEEE Transactions on Industrial Electronics*, vol. 53, pp. 7-30, 2005.

[17] S. M. Gadoue, D. Giaouris, and J. W. Finch, "Performance Evaluation of a Sensorless Induction Motor Drive at Very Low and Zero Speed Using a MRAS Speed Observer," in *The Third international Conference on Industrial and Information Systems*, Kharagpur, INDIA, 2008, pp. 1-6.

[18] K. Akatsu and A. Kawamura, "Sensorless very low-speed and zero-speed estimations with online rotor resistance estimation of induction motor without signal injection," *IEEE Transactions on Industry Applications*, vol. 36, pp. 764-771, 2000.

[19] H. Kubota, K. Matsuse, and T. Nakano, "New adaptive flux observer of induction motor for wide speed range motor drives," in *Industrial Electronics Society, 1990. IECON '90., 16th Annual Conference of IEEE*, 1990, pp. 921-926 vol.2.

[20] R. Blasco-Gimenez, G. M. Asher, M. Sumner, and K. J. Bradley, "Dynamic performance limitations for MRAS based sensorless induction motor drives. 2. Online parameter tuning and dynamic performance studies," *Electric Power Applications, IEE Proceedings*, vol. 143, pp. 123-134, 1996.

[21] V. Vasic and S. Vukosavic, "Robust MRAS-based algorithm for stator resistance and rotor speed identification," *IEEE Power Engineering Review*, vol. 21, pp. 39-41, 2001.

[22] S. M. Gadoue, D. Giaouris, and J. W. Finch, "A new fuzzy logic based adaptation mechanism for MRAS sensorless vector control induction motor drives," in *IET Conference Publications*, York, 2008, pp. 179-183.

[23] C. Lascu, I. Boldea, and F. Blaabjerg, "A modified direct torque control for induction motor sensorless drive," *IEEE Transactions on Industry Applications*, vol. 36, pp. 122-130, 2000.

[24] C. Lascu and G. Andreescu, "Sliding-mode observer and improved integrator with DC-offset compensation for flux estimation in sensorless-controlled induction motors," *IEEE Transactions on Industrial Electronics*, vol. 53, pp. 785-794, 2006.

[25] S. M. Gadoue, D. Giaouris, and J. W. Finch, "Low speed operation improvement of MRAS sensorless vector control induction motor drive using neural network flux observers," in *32nd Annual Conference on IEEE Industrial Electronics*, Paris, 2006, pp. 1212-1217.

[26] K. Szabat, "Robust control of electrical drives using adaptive control structures - a comparison," in *Proceedings of the IEEE International Conference on Industrial Technology*, Chengdu, 2008.

[27] S. Villazana, C. Seijas, A. Caralli, C. Villanueva, and F. Arteaga, "SVM-based and Classical MRAS for On-line Rotor Resistance Estimation: A Comparative Study," in *Intelligent Signal Processing, 2007. WISP 2007. IEEE International Symposium on*, 2007, pp. 1-6.

[28] P. Santhosh, R. H. Chile, A. B. Patil, and D. R. Patil, "Model reference adaptive technique for sensorless speed control of induction motor," in *1st International Conference on Emerging Trends in Engineering and Technology*, Nagpur, Maharashtra, 2008, pp. 893-898.

[29] H. Madadi Kojabadi, L. Chang, and R. Doraiswami, "Effects of Adaptive PI Controller Gains on Speed Estimation Convergence and Noises at Sensorless Induction Motor Drives," in *Canadian Conference on Electrical and Computer Engineering*, Montreal, 2003, pp. 263-266.

[30] C. Schauder, "Adaptive speed identification for vector control of induction motors without rotational transducers," in *Industry Applications Society Annual Meeting, 1989., Conference Record of the 1989 IEEE*, 1989, pp. 493-499 vol.1.

[31] F. Peng and T. Fukao, "Robust speed identification for speed-sensorless vector control of induction motors," *IEEE Transactions on Industry Applications*, vol. 30, pp. 1234-1240, 1994.

[32] M. N. Marwali and A. Keyhani, "Comparative study of rotor flux based MRAS and back EMF based MRAS speed estimators for speed sensorless vector control of induction machines," in *Conference Record - IAS Annual Meeting (IEEE Industry Applications Society)*, New Orleans, LA, USA, 1997, pp. 160-166.

[33] M. Wang, "Parameter Variation Effects in Sensorless Vector Controlled Induction Machines," in *School of Engineering.*: PhD Thesis, Liverpool John Moores University, 1999.

[34] A. M. Trzynadlowski, *The Field Orientation Principle in Control of Induction Motors*. Norwell, Massachusetts: Springer 1993.

[35] W. Leonhard, *Control of Electrical Drives* 3ed. New York: Springer, 2001.

[36] A. Hughes, *Electric Motors and Drives: Fundamentals, Types and Applications*, 3 ed. Jordan Hill, Oxford: Newnes, 2005.

[37] H. Wang, S. Pekarek, and B. Fahimi, "Elimination of position and current sensors in high performance adjustable speed AC drives," in *2005 IEEE International Conference on Electric Machines and Drives*, San Antonio, TX, 2005, pp. 1902-1911.

[38] Y. D. Landau, *Adaptive Control: The Model Reference Approach*: Marcel Dekker Inc, 1979.

[39] M. Sackmann and V. Krebs, "Nonlinear Control of a Continuously Variable Transmission using Hyperstability Theory," in *Proceedings of the European Control Conference*, 1999.

[40] C. Schauder, "Adaptive speed identification for vector control of induction motors without rotational transducers," *IEEE Transactions on Industry Applications*, vol. 28, pp. 1054-1061, 1992.

[41] R. Blasco-Gimenez, G. M. Asher, M. Sumner, and K. J. Bradley, "Dynamic performance limitations for MRAS based sensorless induction motor drives. I. Stability analysis for the closed loop drive," *Electric Power Applications, IEEE Proceedings*, vol. 143, pp. 113-122, 1996.

[42] K. J. Astrom and B. Wittenmark, *Adaptive Control*, 2 ed. Mineola, New York: Addison Wesley 1989.

[43] J. Holtz, "Sensorless control of induction motor drives," *Proceedings of the IEEE*, vol. 90, pp. 1359-1394, 2002.

[44] W. Zhigan, Z. Dawei, and Y. Jianping, "Research on speed estimation algorithm for induction motor drive," in *Power Electronics and Motion Control Conference, 2004. IPEMC 2004. The 4th International*, 2004, pp. 1387-1392 Vol.3.

[45] M. Tsuji, S. Chen, K. Izumi, and E. Yamada, "A sensorless vector control system for induction motors using q-axis flux with stator resistance identification," *IEEE Transactions on Industrial Electronics*, vol. 48, pp. 185-194, 2001.

[46] K. Young Ahn and J. Dae Won, "A novel MRAS based speed sensorless control of induction motor," in *Industrial Electronics Society, The 25th Annual Conference of the IEEE*. vol. 2 San Jose, CA, 1999, pp. 933-938.

[47] B. Karanayil, M. F. Rahman, and C. Grantham, "An implementation of a programmable cascaded low-pass filter for a rotor flux synthesizer for an induction motor drive," *IEEE Transactions on Power Electronics*, vol. 19, pp. 257-263, 2004.

[48] M. Hinkkanen and J. Luomi, "Modified integrator for voltage model flux estimation of induction motors," *IEEE Transactions on Industrial Electronics*, vol. 50, pp. 818-820, 2003.

[49] G. Qiang, C. S. Spiteri, G. M. Asher, and M. Sumner, "Sensorless speed operation of cage induction motor using zero drift feedback integration with MRAS observer," in *Power Electronics and Applications, 2005 European Conference on*, 2005, pp. 1-9.

[50] M. Barut, S. Bogosyan, and M. Gokasan, "Speed-sensorless estimation for induction motors sing extended Kalman filters," *IEEE Transactions on Industrial Electronics,* vol. 54, pp. 272-280, 2007.

[51] K. L. Shi, T. F. Chan, Y. K. Wong, and S. L. Ho, "Speed estimation of an induction motor drive using an optimized extended Kalman filter," *IEEE Transactions on Industrial Electronics,* vol. 49, pp. 124-133, 2002.

[52] M. Cirrincione and M. Pucci, "An MRAS-based sensorless high-performance induction motor drive with a predictive adaptive model," *IEEE Transactions on Industrial Electronics,* vol. 52, pp. 532-551, 2005.

[53] L. Zhen and L. Xu, "Sensorless field orientation control of induction machines based on a mutual MRAS scheme," *IEEE Transactions on Industrial Electronics,* vol. 45, pp. 824-831, 1998.

[54] V. Vasic, S. N. Vukosavic, and E. Levi, "A Stator Resistance Estimation Scheme for Speed Sensorless Rotor Flux Oriented Induction Motor Drives," *IEEE Transactions on Energy Conversion,* vol. 18, pp. 476-483, 2003.

[55] R. Blasco-Gimenez., "High Performance Sensorless Vector Control of Induction Motor Drives," PhD Thesis, Nottingham: University of Nottingham, 1995.

[56] K. H and M. K, "Speed sensorless field-oriented control of induction motor with rotor resistance adaptation," *IEEE Transactions on Industry Applications,* vol. 30, pp. 1219-1224, 1994.

[57] K. Kubota and K. Matsuse, "Speed sensorless field-oriented control of induction motor with rotor resistance adaptation," *IEEE Transactions on Industry Applications,* vol. 30, pp. 1219-1224, 1994.

[58] G. Yang and T. H. Chin, "Adaptive-speed identification scheme for a vector-controlled speed sensorless inverter-induction motor drive," *IEEE Transactions on Industry Applications,* vol. 29, pp. 820-825, 1993.

[59] X. Xingyi and D. W. Novotny, "Implementation of direct stator flux orientation control on a versatile DSP based system," *IEEE Transactions on Industry Applications,* vol. 27, pp. 694-700, 1991.

[60] S. I. N. Kumara, "Speed sensorless field orientation control of induction motor drive," in *School of Electrical, Electronic and Computer Engineering*. vol. PhD Newcastle upon Tyne: Newcastle University, 2006.

[61] M. N. Cirstea, J. G. K. A. Dinu, and M. McCormick, *Neural and Fuzzy Logic Control of Drives and Power Systems*. Oxford: Newnes, 2002.

[62] P. Vas, *Artificial-Intelligence-Based Electrical Machines and Drives-Application of Fuzzy, Neural, Fuzzy-Neural and Genetic Algorithm Based Techniques*. NewYork: Oxford University Press, 1999.

[63] P.Vas, A. F. Stronach, and M. Neuroth, "A Fuzzy-controlled Speed-sensorless Induction Motor Drive with Flux Estimators " in *Electrical Machines and Drives*, University of Aberdeen, Scotland, UK, 1995.

[64] J. C. Lopez, L. Romeral, A. Arias, and E. Aldabas, "Novel Fuzzy Adaptive Sensorless Induction Motor Drive," *IEEE Transactions on Industrial Electronics*, vol. 53, pp. 1170-1178, 2006.

[65] C. Chen and T. Chen, "Speed Sensorless of an Induction Motor Using Self-tuning Fuzzy Identification," in *Second International Conference on Innovative Computing, Information and Control*, 2007, pp. 398-398.

[66] M. Zerikat, S. Chekroun, and A. Mechernene, "Fuzzy-neural networks controller-based adapatation mechanism for MRAS sensorless induction motor drives," in *8th International Symposium on Advanced Electromechanical Motion Systems & Electric Drives Joint Symposium*, 2009, pp. 1-7.

[67] L. Ben-Brahim, "Motor speed identification via neural networks," in *IEEE Industry Applications Magazine*. vol. 1, 1995, pp. 28-32.

[68] L. Ben-Brahim, S. Tadakuma, and A. Akdag, "Speed control of induction motor without rotational transducers," *IEEE Transactions on Industry Applications*, vol. 35, pp. 844-850, 1999.

[69] S. H. Kim, T. S. Park, J. Y. Yoo, and G. T. Park, "Speed-Sensorless Vector Control of an Induction Motor Using Neural Network Speed Estimation," *IEEE Transactions on Industrial Electronics*, vol. 48, pp. 609-614, June 2001.

[70] J. Campbell and M. Sumner, "Practical sensorless induction motor drive employing an artificial neural network for online parameter adaptation," *Electric Power Applications, IEE Proceedings*, vol. 149, pp. 255-260, 2002.

[71] B. Karanayil, M. F. Rahman, and C. Grantham, "Online Stator and rotor resistance estimation scheme using artificial neural networks for vector controlled speed sensorless induction motor drives," *IEEE Transactions on Industrial Electronics*, vol. 54, pp. 167-176, February 2007.

[72] M. Cirrincione, M. Pucci, G. Cirrincione, and G. A. Capolino, "Sensorless control of induction machines by a new neural algorithm: The TLS EXIN neuron," *IEEE Transactions on Industrial Electronics*, vol. 54, pp. 127-149, 2007.

[73] M. Cirrincione, M. Pucci, G. Cirrincione, and G. A. Capolino, "A new adaptive integration methodology for estimating flux in induction machine drives," *IEEE Transactions on Power Electronics*, vol. 19, pp. 25-34, 2004.

[74] A. R. Haron and N. R. N. Idris, "Simulation of MRAS-based speed sensorless estimation of induction motor drives using MATLAB/SIMULINK," in *1st International Power and Energy Conference, (PECon 2006) Proceedings*, Putrajaya, 2006, pp. 411-415.

[75] L. Yingshun and X. Dingyu, "A novel fuzzy model-reference adaptive control," in *Proceedings of the World Congress on Intelligent Control and Automation (WCICA)*, Dalian, 2006, pp. 2204-2208.

[76] L. Han, X. Wen, and G. Chen, "A novel adaptive scheme for stator resistance estimation in sensorless induction motor drives," in *Conference Proceedings - IPEMC 2006: CES/IEEE 5th International Power Electronics and Motion Control Conference*, Shanghai, 2007, pp. 1049-1053.

[77] M. Hrasko, J. Vittek, R. Havrila, and I. Lokseninec, "Rotor flux observer in Pseudo - Sliding mode for vector controlled induction motor drives," in *EPE-PEMC 2006: 12th International Power Electronics and Motion Control Conference, Proceedings*, Portoroz, 2007, pp. 1133-1136.

[78] F. Giri, *AC Electric Motors Control: Advanced Design Techniques and Applications*, 1 ed. Chichester, West Sussex: Wiley, 2013.

[79] D. Schneider, "A faster fast fourier transform," *Spectrum, IEEE*, vol. 49, pp. 12-13.

[80] M. Salcone and J. Bond, "Selecting film bus link capacitors for high performance inverter applications," in *IEEE International Electric Machines and Drives Conference*, 2009, pp. 1692-1699.

[81] T. M. U. Ned Mohan , William P. Robbins *Power Electronics: Converters, Applications, and Design*, 3 ed.: ohn Wiley & Sons, 2003.

[82] M. Rashed, F. Stronach, and P. Vas, "A new stable MRAS-based speed and stator resistance estimators for sensorless vector control induction motor drive at low speeds," in *Industry Applications Conference, 38th IAS Annual Meeting, Conference Record of the IEEE*, 2003, pp. 1181-1188 vol.2.

[83] G. Armstrong, "Encoderless Vector Controlled Induction Motor Drives," PhD Thesis, Newcastle upon Tyne: Newcastle University 1998.

Appendix A - Space Vector Control Theory

A.1 Field Orientated Control

The Field Orientated Control (FOC) consists of controlling the stator currents represented by a vector. This control is based on projections which transform a three phase time and speed dependent system into a two co-ordinate (d,q) time invariant system. These projections lead to a structure similar to that of a DC machine control. Field orientated controlled machines need two constants as input references: where the torque component is aligned with the q co-ordinate and the flux component is aligned with d co-ordinate. As Field Orientated Control is simply based on projections the control structure handles instantaneous electrical quantities. This makes the control accurate in both steady state and transient operation and independent of the limited bandwidth mathematical model. The FOC thus solves the classic scheme problems, in the following ways:

- The ease of reaching constant reference torque component and flux component of the stator current.
- The ease of applying direct torque control because in the (d, q) reference frame the expression of the torque is:

$$\boldsymbol{m \propto \psi_R i_{qs}}$$

By maintaining the amplitude of the rotor flux (ψ_R) at a fixed value we have a linear relationship between torque and torque component (i_{qs}). We can then control the motor torque by controlling the torque component of stator current vector.

A.1.1 Space Vector Definition & Projection

The three-phase voltages, currents and fluxes of AC-motors can be analyzed in terms of complex space vectors. In regard to the currents, assuming that ia_s, ib_s and ic are the instantaneous currents in the stator phases, the current space vector $\overline{i_s}$ is defined by:

$$\overline{i_s} = \frac{2}{3}(\overline{ia_s} + \boldsymbol{a}\overline{ib_s} + \boldsymbol{a}^2\overline{ic_s}) \qquad \text{(A.1)}$$

Where:

$$\boldsymbol{a} = e^{j\frac{2\pi}{3}} = -\frac{1}{2} + j\frac{\sqrt{3}}{2}$$

$$\boldsymbol{a}^2 = e^{j\frac{4\pi}{3}} = -\frac{1}{2} - j\frac{\sqrt{3}}{2}$$

$\boldsymbol{a}^2$ *and* $\boldsymbol{a}$ Represent the spatial operators. The following diagram shows the stator current complex space vector:

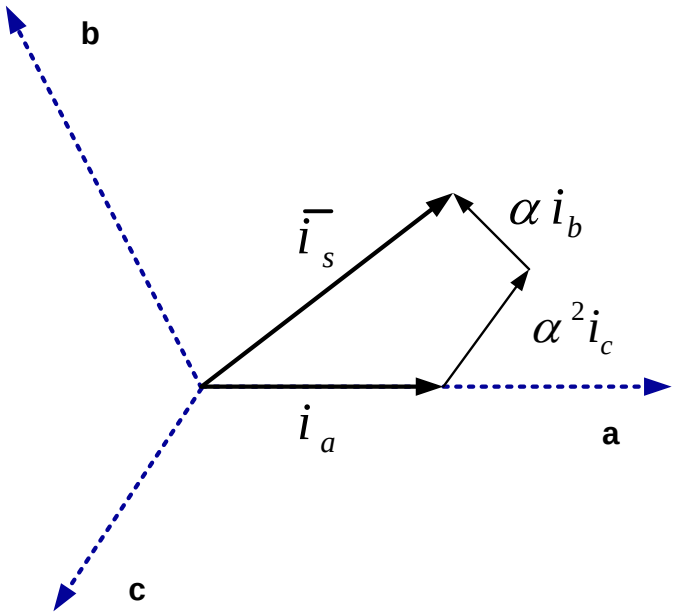

Figure A. 1 Stator current space vector and its component in (a, b, c).

In (A.1), $ia_s, ib_s \; and \; ic_s$ are three phase currents that flow in three phase windings displaced by 120◦ from each other and producing sinusoidal distributing magneto-motive force (mmf) and (a, b, c) are the three phase system axes.

The $\bar{i_s}$ space vector current depicts the three phase sinusoidal system and it can to be transformed into a two time invariant co-ordinate system. This transformation can be achieved in two steps:

- $(a, b, c) \Rightarrow (\alpha, \beta)$ 3 phase to 2 phase transformation. This is known as the ***Clarke*** transformation and produces a two co-ordinate time variant system.

- $(\alpha, \beta) \Rightarrow (d, q)$ Transformation from rotating reference to the stator reference frame. This is known as the **Park** transformation that produces a two co-ordinate time invariant system.

A.1.1.1 Clarke Transformation (The $(\boldsymbol{a}, \boldsymbol{b}, \boldsymbol{c}) \Rightarrow (\boldsymbol{\alpha}, \boldsymbol{\beta})$ projection)

The space vector can be represented in another reference frame with only two orthogonal axes called (α, β). Assuming that the axis α and the axis β are in the same direction we have the following vector diagram:

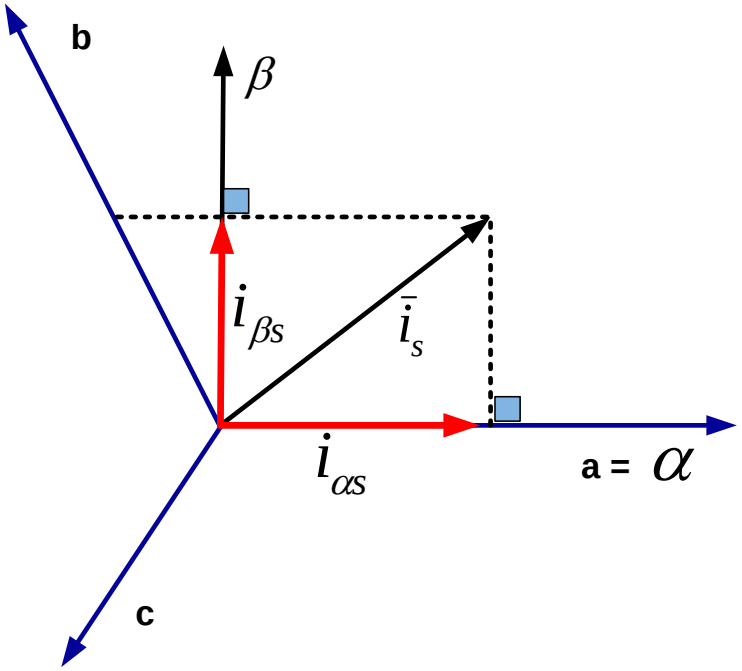

Figure A. 2 Stator current space vector and its components in (α,β).

The projection that modifies the three phase system into the (α, β) two dimensions orthogonal system is presented below. Resolving the stator current space vector in (A.1) into real and imaginary parts yields the two axis components of the stator current vector in the stator reference frame as shown in figure A.2[13].

$$i_{\alpha s} = \frac{2}{3} ia_s - \frac{1}{3} ib_s - \frac{1}{3} ic_s \quad \text{(A.2)}$$

$$i_{\beta s} = \frac{1}{\sqrt{3}} ib_s - \frac{1}{\sqrt{3}} ic_s \quad \text{(A.3)}$$

The currents $i_{s\alpha}$ *and* $i_{s\beta}$ are the actual currents that flow in the two phase stator windings s_D *and* s_Q which are quadrature in space. The stator current space vector can be written in polar and rectangular form as:

$$\overline{i_s} = \left|\overline{i_s}\right| e^{j\Theta_s} = i_{\alpha s} + j\, i_{\beta s} \quad \text{(A.4)}$$

$$\begin{bmatrix} i_{\alpha s} \\ i_{\beta s} \end{bmatrix} = \frac{2}{3} \begin{bmatrix} 1 & -\frac{1}{2} & -\frac{1}{2} \\ 0 & \frac{\sqrt{3}}{2} & -\frac{\sqrt{3}}{2} \end{bmatrix} \quad \text{(A.5)}$$

A.1.1.2 Inverse Clarke Transformation (The $(\alpha, \beta) \Rightarrow (a, b, c)$ projection)

The transformation from two phase quantities into three phase quantities can be written as:

$$i_{sa} = i_{s\alpha}$$

$$i_{bs} = -\frac{1}{2} i_{\alpha s} + \frac{\sqrt{3}}{2} i_{\beta s}$$

$$i_{cs} = -\frac{1}{2} i_{\alpha s} - \frac{\sqrt{3}}{2} i_{\beta s}$$

The above transformation can be expressed in a matrix form as:

$$\begin{bmatrix} i_{as} \\ i_{bs} \\ i_{cs} \end{bmatrix} = \begin{bmatrix} 1 & 0 \\ -\frac{1}{2} & \frac{\sqrt{3}}{2} \\ -\frac{1}{2} & -\frac{\sqrt{3}}{2} \end{bmatrix} \begin{bmatrix} i_{\alpha s} \\ i_{\beta s} \end{bmatrix} \quad (A.6)$$

A.1.1.3 Park Transformation (The $(\alpha, \beta) \Rightarrow (d, q)$)

This is the most important transformation in the FOC. In fact, this projection modifies a two phase orthogonal system (α, β) in the (d, q) rotating reference frame. If we consider the d axis aligned with the rotor flux, the next diagram shows, for the current vector, the relationship from the two reference frame:

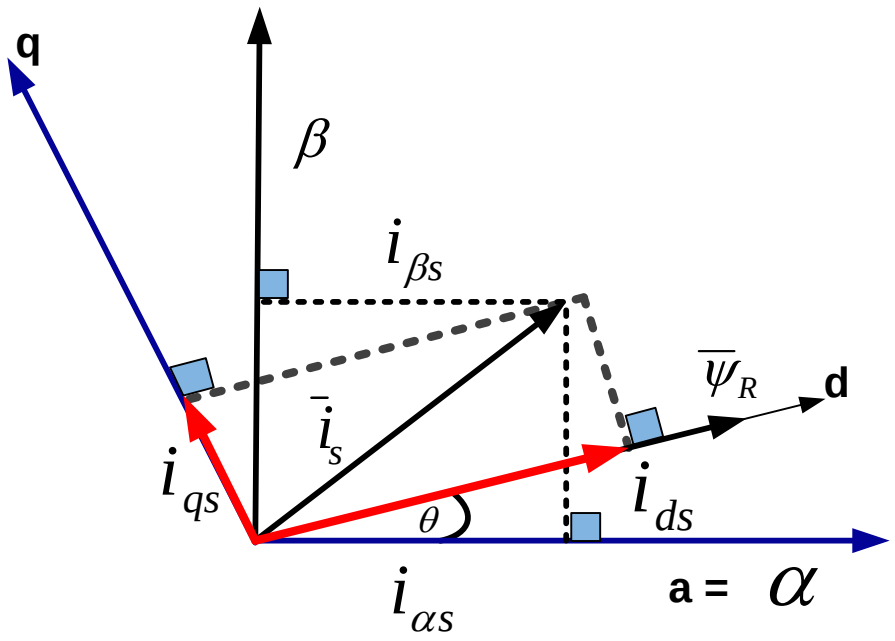

Figure A. 3 Stator current space vector and its component in (α, β) and in the (d, q).

The flux and torque components of the current vector are determined by the following equations:

$$\overline{i_s^e} = i_{ds} + i_{qs} = \overline{i_s^s} e^{-j\theta_r} = \left(i_{\boldsymbol{\alpha s}} + i_{\boldsymbol{\beta s}}\right) e^{-j\theta_r} \qquad \text{(A.7)}$$

θ_r is the Rotor Flux Angle, $\theta_r = \tan^{-1} \frac{\Psi_{qr}}{\Psi_{dr}}$.

The superscripts *s* and *r* stand for the stator and the rotor reference frames while the subscript *s* stands for the stator quantities. The transformation defined in (A.7) can be written in matrix form as:

$$\begin{bmatrix} i_{ds} \\ i_{qs} \end{bmatrix} = \begin{bmatrix} \cos\theta_r & \sin\theta_r \\ -\sin\theta_r & \cos\theta_r \end{bmatrix} \begin{bmatrix} i_{\boldsymbol{\alpha s}} \\ i_{\boldsymbol{\beta s}} \end{bmatrix} \qquad \text{(A.8)}$$

These components depend on the current vector (α, β) components and on the rotor flux position; if we know the right rotor flux position then, by this projection, the (d, q) component becomes a constant. We obtain a two co-ordinate system $\begin{pmatrix} i_{ds} \\ i_{qs} \end{pmatrix}$ with the following characteristics:

- Two co-ordinate time invariant system
- Direct torque control is possible and straightforward by regulating i_{sd} , which stands for the flux component, and i_{sq}, which stands for the torque component.

For vector control implementation, a transformation between (d, q)rotor and the stator (α, β) reference frames is required. Figure 2.5 shows the relationship between the two reference frames where $\theta = \theta_r$ and it is the rotor flux position. The stator coordinates are fixed to the stator and therefore are stationary while the rotor (synchronous) frame coordinates rotates synchronously with the stator magnetic field.

The transformation from the stator frame to the synchronous rotor frame is given by:

$$\overline{i_s^r} = i_{ds} + i_{qs} = \overline{i_s^s} e^{-j\theta_r} = \left(i_{\alpha s} + i_{\beta s}\right) e^{-j\theta_r} \qquad \text{(A.9)}$$

The superscripts *s* and *r* stand for the stator and the rotor reference frames while the subscript *s* stands for the stator quantities. The transformation defined in (A.9) can be written in matrix form as:

$$\begin{bmatrix} i_{\alpha s} \\ i_{\beta s} \end{bmatrix} = \begin{bmatrix} \cos\theta_r & -\sin\theta_r \\ \sin\theta_r & \cos\theta_r \end{bmatrix} \begin{bmatrix} i_{\boldsymbol{ds}} \\ i_{qs} \end{bmatrix}$$

A.1.1.4 Inverse Park Transformation (The $(\boldsymbol{d}, \boldsymbol{q}) => (\boldsymbol{\alpha}, \boldsymbol{\beta})$)

This transformation transforms the electrical quantities from the rotating reference frame (d, q) into a two phase orthogonal system:

The transformation from the Rotor, synchronous, frame to stator reference frame is given by:

$$\overline{i_s^s} = i_{\boldsymbol{\alpha s}} + j i_{\boldsymbol{\beta s}} = \overline{i_s^r} e^{j\theta_r} = \left(i_{ds} + j i_{sq}\right) e^{j\theta_r} \quad \text{(A.10)}$$

In matrix form:

$$\begin{bmatrix} i_{\boldsymbol{\alpha s}} \\ i_{\boldsymbol{\beta s}} \end{bmatrix} = \begin{bmatrix} \cos\theta_r & -\sin\theta_r \\ \sin\theta_r & \cos\theta_r \end{bmatrix} \begin{bmatrix} i_{ds} \\ i_{qs} \end{bmatrix} \quad \text{(A.11)}$$

Similarly, the stator voltages and the flux space vectors expressed at the stator reference frame are:

$$\overline{v_s} = \frac{2}{3}(vb_{\mathrm{s}} + avb_{\mathrm{s}} + a^2 vc_{\mathrm{s}}) \quad \text{(A.12)}$$

$$= v_{\boldsymbol{\alpha s}} + j v_{\boldsymbol{\beta s}}$$

$$\overline{\Psi_s} = \frac{2}{3}(\Psi a_{\mathrm{s}} + a\Psi b_{\mathrm{s}} + a^2 \Psi c_{\mathrm{s}}) \quad \text{(A.13)}$$

$$= \Psi_{\boldsymbol{\alpha s}} + j\Psi_{\boldsymbol{\beta s}}$$

By following a similar approach, the space vector of the rotor current in a fixed rotor reference frame can be expressed as:

$$\overline{i_r} = \frac{2}{3}(\overline{ia_r} + a\overline{ib_r} + a^2\overline{ic_r}) \quad \text{(A.14)}$$

$$\overline{i_r} = \left|\overline{i_r}\right| e^{j\theta_r} = i_{\alpha r} + j\, i_{\beta r}$$

The currents $\left(i_{\alpha r},\ j i_{\beta r}\right)$ are the actual currents that flow in the two phase rotor windings $(\alpha r,\ \beta r)$ which are quadrature in space. And θ_r is the rotor position.

A.1.2 Basic scheme for the Vector Control

The following diagram summarises the basic scheme of torque control with Field Oriented Control:

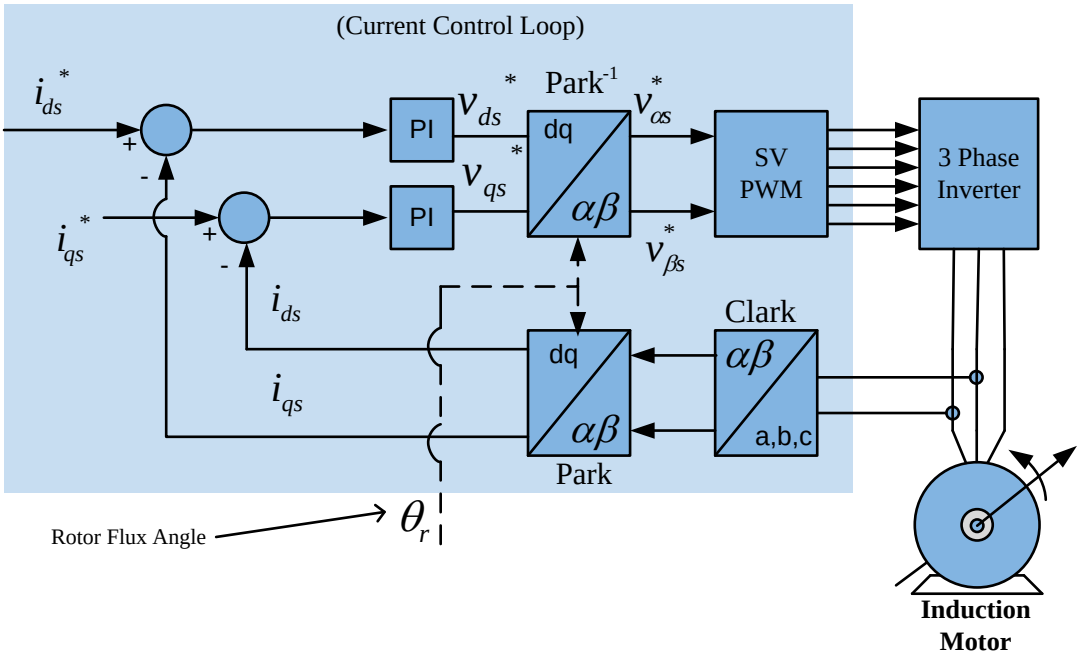

Figure A. 4 Basic scheme of FOC for induction motor.

Two motor phase currents are measured. These measurements feed the Clarke transformation module. The outputs of this projection are designated $i_{\alpha s}$ and$i_{\beta s}$. These two components of the current are the inputs of the Park transformation that gives the current in the (α, β)rotating reference frame. The (i_{ds}, i_{qs}) components are compared to the references $i_{ds}{}^*$, the flux reference and $i_{qs}{}^*$, the torque reference. At this point, this control structure shows an interesting advantage: it can be used to control synchronous or induction machines by simply changing the flux reference and obtaining rotor flux position. As in synchronous permanent magnet motors, the rotor flux is fixed which can be determined by the magnets, there is no need to create one. Hence, when controlling a Permanent Magnet Synchronous Machine, $i_{ds}{}^*$ should be set to zero. As induction motors need rotor flux to be created in order to operate, the flux reference must not be zero. This conveniently solves one of the major drawbacks of the "classic" control structures: the portability from asynchronous to synchronous drives. The torque command $i_{qs}{}^*$could be the output of the speed regulator when implementing speed control via means of field orientation. The outputs of the current regulators are $V_{ds}{}^*$ and $V_{qs}{}^*$; they are applied to the inverse Park transformation. The outputs of this projection are $V_{\alpha s}{}^*$ and $V_{\beta s}{}^*$ which are the components of the stator vector voltage in

the (α, β)stationary orthogonal reference frame. These are the inputs of the Space Vector PWM. The outputs of this block are the signals that drive the inverter. Note that both Park and inverse Park transformations need the rotor flux position. Obtaining this rotor flux position depends on the AC machine type being synchronous or asynchronous machine. Fundamental requirements for the FOC are a knowledge of two phase currents, as the motor is star-connected, the third phase current is also known, since $ia_s + ib_s + ic_s = 0$, and the rotor flux position.

A.1.2.1 Rotor Flux Position

Knowledge of the rotor flux position is the core of Field Oriented Control. In effect, if there is an error in this variable the rotor flux is not aligned with the d-axis and the flux and torque components of the stator current, i_{ds} and i_{qs} will be incorrect. Figure A. 5 shows the $(\mathrm{a}, \mathrm{b}, \mathrm{c}), (\alpha, \beta)$ and (d, q) reference frames, and the correct position of the rotor flux, the stator current and stator voltage space vector that rotates with (d, q) reference at synchronous speed.

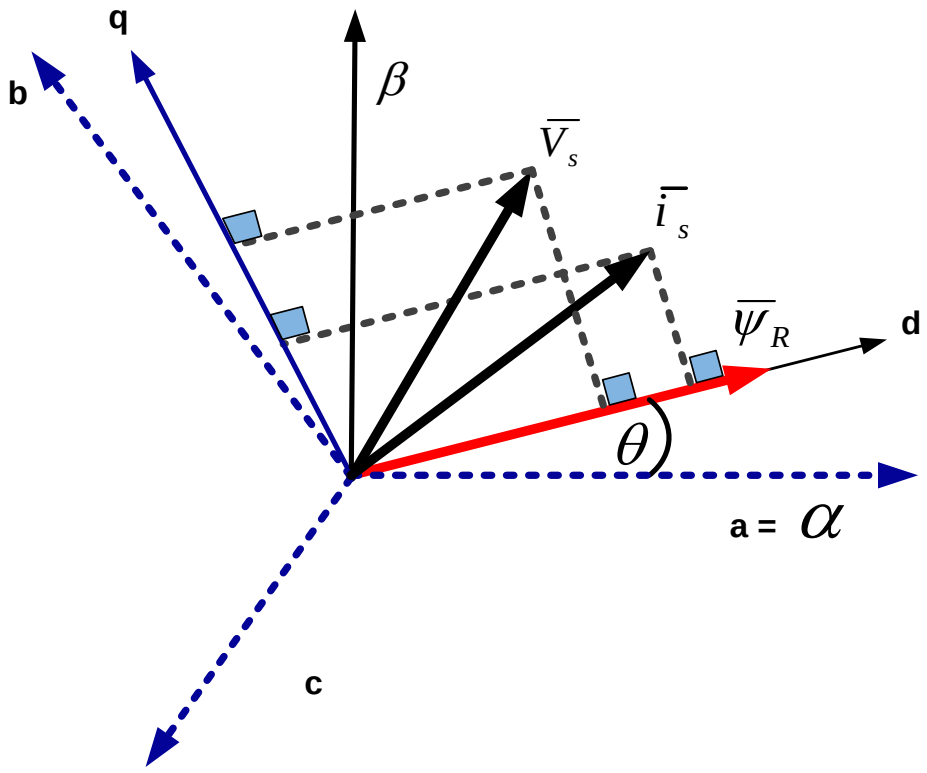

Figure A. 5 Current, voltage & rotor flux space vectors in the (d, q) rotating reference frame and their relationship with (a, b, c) and (α, β) stationary reference frame.

The rotor flux position measurement is different if synchronous or induction motor is considered.

- In the synchronous machine the rotor speed is equal to the rotor flux speed. Then q (rotor flux position) is directly measured by position sensor or by integration of rotor speed.
- In the induction machine the rotor speed is not equal to the rotor flux speed (there is a slip speed), then it needs a particular method to calculate q. The basic method is the use of the current model which needs two equations of the motor model in (d, q) reference frame.

Implementing Field Orientated Control has made it possible to directly and separately control the torque and flux of AC machines. Field Orientated Controlled AC machines thus obtain every DC machine advantage: instantaneous control of the separate quantities which allows accurate transient and steady state management. In addition, FOC solves the mechanical commutation problems inherent with DC machines. And by providing high CPU power and highly versatile motor control dedicated peripherals, makes the use of DC machines obsolete in terms of power conversion efficiency and system reliability, when compared with FOC AC machines.

A.1.3 **Space Vector Modulation**

The Space Vector Pulse Width Modulation, SVPWM, refers to a special switching sequence of the upper three power devices of a three-phase voltage source inverters (VSI) used in application such as AC induction and permanent magnet synchronous motor drives. This special switching scheme for the power devices results in 3 pseudo-sinusoidal currents in the stator phases.

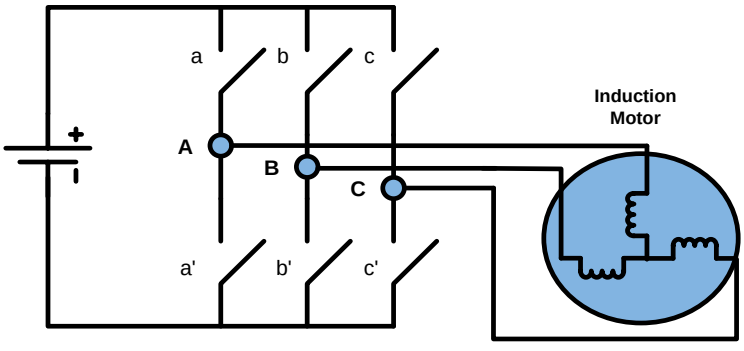

Figure A. 6 Power bridge for a three-phase VSI.

It has been shown that SVPWM generates less harmonic distortion in the output voltages or currents in the windings of the motor load and provides more efficient use of DC supply voltage, in comparison to direct sinusoidal modulation technique. For the three-phase power inverter configurations shown in Figure A.6, there are eight possible combinations of on and off states of the upper power transistors. These combinations and the resulting instantaneous output line-to-line and phase voltages, for a DC bus voltage of VDC, are shown in Table A. 1.

Table1 A. 1 Device on/off patterns and resulting instantaneous voltages of a three-phase power inverter.

c	b	a	v_{AN}	v_{BN}	v_{CN}	v_{AB}	v_{ABC}	v_{CA}
0	0	0	0	0	0	0	0	0
0	0	1	2VDC/3	-VDC/3	-VDC/3	VDC	0	-VDC
0	1	0	-VDC/3	2VDC/3	-VDC/3	-VDC	VDC	0
0	1	1	VDC/3	VDC/3	-2VDC/3	0	VDC	-VDC
1	0	0	- VDC/3	-VDC/3	2VDC/3	0	-VDC	-VDC
1	0	1	VDC/3	-2VDC/3	VDC/3	VDC	-VDC	0
1	1	0	-2VDC/3	VDC/3	VDC/3	-VDC	0	VDC
1	1	1	0	0	0	0	0	0

The quadrature quantities in the (α, β) frame corresponding to these 3 phase voltages are given by the general Clarke transform equation:

$$v_{\alpha s} = v_{AN}$$

$$v_{\beta s} = {(2v_{BN} + v_{AN})}/{\sqrt{3}}$$

In matrix from the above equation is also expressed as,

$$\begin{bmatrix} v_{\alpha s} \\ v_{\beta s} \end{bmatrix} = \frac{2}{3}\begin{bmatrix} 1 & \frac{-1}{2} & \frac{-1}{2} \\ 0 & \frac{\sqrt{3}}{2} & \frac{-\sqrt{3}}{2} \end{bmatrix}\begin{bmatrix} v_{AN} \\ v_{BN} \\ v_{CN} \end{bmatrix}$$

Due to the fact that only 8 combinations are possible for the power switches, $V_{\alpha s}$ and $V_{\beta s}$ can also take only a finite number of values in the (α, β) frame according to the status of the transistor command signals (c, b, a). These values of $v_{\alpha s}$ and $v_{\beta s}$ for the corresponding instantaneous values of the phase voltages (v_{AN} , v_{BN} , v_{CN}) are listed in Table A.2.

Table A. 2 Switching patterns, corresponding space vectors and their (α, β) components.

c	b	a	$v_{\alpha s}$	$v_{\beta s}$	vector
0	**0**	**0**	**0**	**0**	**0**
0	**0**	**1**	$\frac{2\mathrm{VDC}}{3}$	**0**	**U0**
0	**1**	**0**	$-\frac{\mathrm{VDC}}{3}$	$\frac{\mathrm{VDC}}{\sqrt{3}}$	**U120**
0	**1**	**1**	$\frac{\mathrm{VDC}}{3}$	$\frac{\mathrm{VDC}}{\sqrt{3}}$	**U60**
1	**0**	**0**	$-\frac{\mathrm{VDC}}{3}$	$-\frac{\mathrm{VDC}}{\sqrt{3}}$	**U240**
1	**0**	**1**	$-\frac{\mathrm{VDC}}{3}$	$-\frac{\mathrm{VDC}}{\sqrt{3}}$	**U300**
1	**1**	**0**	$-\frac{2\mathrm{VDC}}{3}$	**0**	**U180**
1	**1**	**1**	**0**	**0**	**O111**

These values of $V_{S\alpha}$ and $V_{S\beta}$, listed in Table 2, are called the (α, β) components of the basic space vectors corresponding to the appropriate transistor command signal (c, b, a). The space vectors corresponding to the signal (c, b, a) are listed in the last column in

Table 2. For example, (c, b, a) = 001 indicates that the space vector is $U0$.The eight basic space vectors defined by the combination of the switches are also shown in Figure 3.

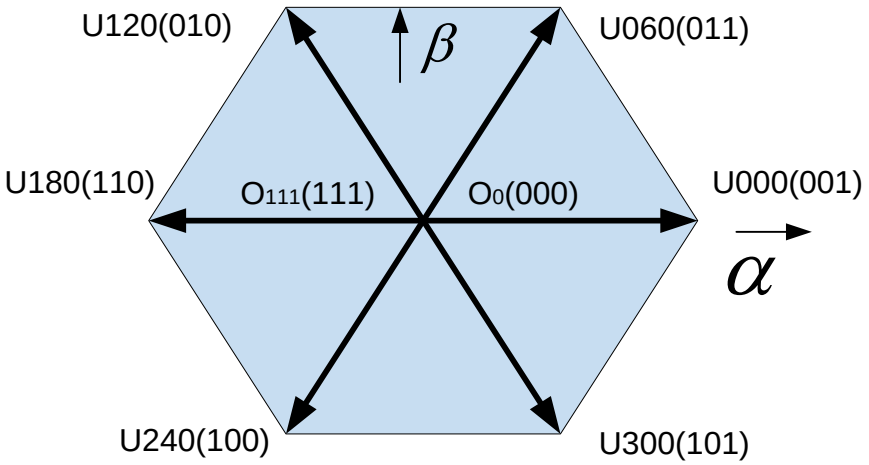

Figure A. 7 Basic space vectors.

Projection of the stator reference voltage vector U_{out}

The objective of Space Vector PWM technique is to approximate a given stator reference voltage vector U_{out} by combination of the switching pattern corresponding to the basic space vectors. The reference vector U_{out} is represented by its (α, β) components, $U_{\alpha}$and U_{β}. Figure 4 shows the reference voltage vector, it's (α, β) components and two of the basic space vectors, *U0* and *U60*. The figure also indicates the resultant α and β components for the space vectors *U0* and *U60*. $\sum V_{\beta s}$ represents the sum of the α components of *U0* and *U60*, while $\sum V_{\alpha s}$ represents the sum of the β components of *U0* and *U60*. Therefore,

$$\sum V_{\beta s} = 0 + \frac{V_{DC}}{\sqrt{3}} = \frac{V_{DC}}{\sqrt{3}}$$

$$\sum V_{\alpha s} = \frac{2V_{DC}}{3} + \frac{V_{DC}}{3} = V_{DC}$$

For the case in Figure A.8, the reference vector $U_{out}$is in the sector contained by $U0$ and $U60$. Therefore U_{out} is represented by $U0$ and $U60$. So we can write,

$$T = T_1 + T_3 + T_0$$

$$U_{out} = \frac{T_1}{T} U_0 + \frac{T_3}{T} U_{60}$$

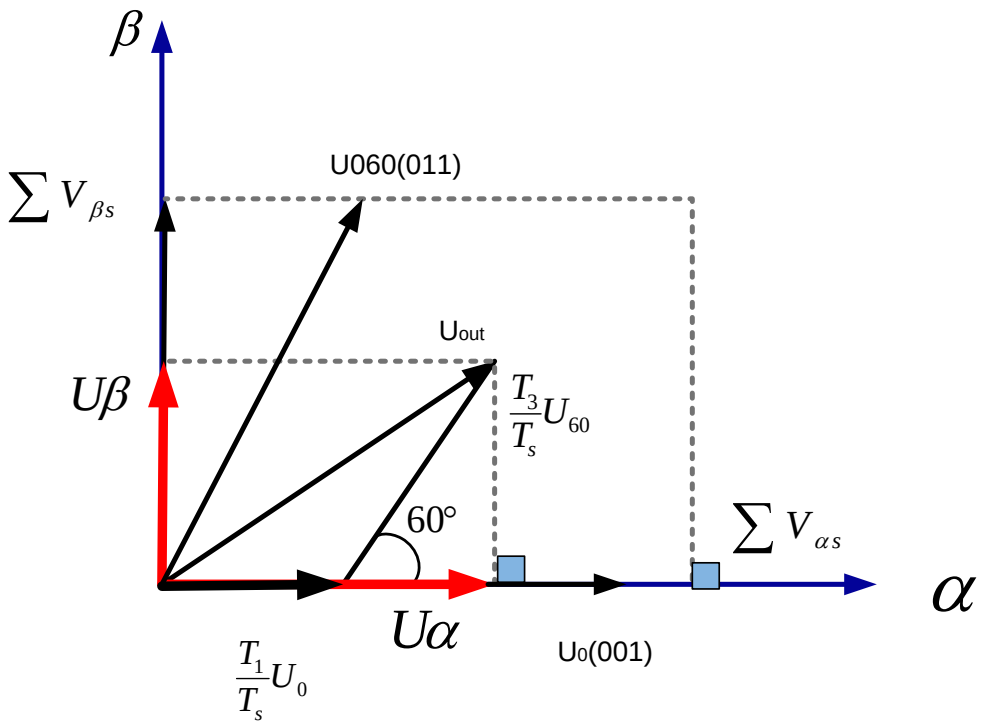

Figure A. 8 Projection of the reference voltage vector.

Where $T1$ and $T3$ are the respective durations in time for which $U0$ and $U60$ are applied within period T. $T0$ is the time duration for which the null vector is applied. These time durations can be calculated as follows:

$$U_{\beta=} \frac{T_3}{T} |U_{60}| \sin 60^{\circ}$$

$$U_{\alpha=} \frac{T_1}{T} |U_0| + \frac{T_3}{T} |U_{60}| \cos 60^{\circ}$$

From Table 2 and Figure 4 it is evident that the magnitude of all the space vectors is $2VDC/3$. When this is normalized by the maximum phase voltage (line to neutral), $VDC/\sqrt{3}$, the magnitude of the space vectors become $2/\sqrt{3}$ i.e., the normalized magnitudes are $|U0| = |U60| = 2/\sqrt{3}$. Therefore, from the last two equations the time durations are calculated as,

$$T_1 = \frac{T}{2}\left(\sqrt{3}U_\alpha - U_\beta\right)$$

$$T_3 = TU_\beta$$

U_α and U_β also represent the normalized (α, β) components of U_{out} with respect to the maximum phase voltage $(VDC/\sqrt{3})$. The rest of the period is spent in applying the null vector $T0$. The time durations, as a fraction of the total T, are given by,

$$t_1 = \frac{T_1}{T} = \frac{1}{2}\left(\sqrt{3}U_\alpha - U_\beta\right)$$

$$t_2 = \frac{T_3}{T} = U_\beta$$

In a similar manner, if U_{out} is in sector contained by $U60$ and $U120$, then by knowing

$|U60| = |U120| = 2/\sqrt{3}$ (normalized with respect to $VDC/\sqrt{3}$), the time durations can be derived as,

$$t_1 = \frac{T_2}{T} = \frac{1}{2}\left(-\sqrt{3}U_\alpha + U_\beta\right)$$

$$t_2 = \frac{T_3}{T} = \frac{1}{2}\left(\sqrt{3}U_\alpha + U_\beta\right)$$

where, $T2$ is the duration in time for which $U120$ is applied within period T

Now, if we define 3 variables X, Y and Z according to the following equations,

$$X = U_\beta$$

$$Y = \frac{1}{2}\left(\sqrt{3}\,U_\alpha + U_\beta\right)$$

$$Z = \frac{1}{2}\left(-\sqrt{3}\,U_\alpha + U_\beta\right)$$

Then for the first example, when U_{out} is in sector contained by $U0$ and $U60$, $t1 = -Z$, $t2 = X$.

For the second example, when U_{out} is in sector contained by $U60$ and $U120$, $t1 = Z$, $t2 = Y$.

In a similar manner $t1$ and $t2$ can be calculated for the cases when U_{out} is in sectors contained by other space vectors. For different sectors the expressions for $t1$ and $t2$ in terms of X, Y and Z are listed in Table A.3.

Table A .3 t1 and t2 definitions for different sector in terms of X, Y, Z variables.

Sector	U_0, U_{60}	U_{60}, U_{120}	U_{120}, U_{180}	U_{180}, U_{240}	U_{240}, U_{300}	U_{300}, U_0
t_1	-Z	Z	X	-X	-Y	Y
t_2	X	Y	Y	Z	-Z	-X

In order to know which of the above variables apply, the knowledge of the sector containing the reference voltage vector is needed. This is achieved by first converting the (α, β) components of the reference vector U_{out} into a balanced three phase quantities. That is, U_α and U_β are converted to a balanced three phase quantities V_{ref1} , V_{ref2} and V_{ref3} according to the following inverse Clarke transformation:

$$V_{ref1} = U_\beta$$

$$V_{ref2} = \frac{-U_\beta + U_\alpha \times \sqrt{3}}{2}$$

$$V_{ref3} = \frac{-U_\beta - U_\alpha \times \sqrt{3}}{2}$$

Note that, this transformation projects the quadrature or β component, U_β , into V_{ref1}. This means that the voltages V_{ref1} , V_{ref2} and V_{ref3} are all phase advanced by 90^0 when compared to the corresponding voltages generated by the conventional inverse Clarke transformation which projects the α component, U_α, into phase voltage v_{AN}. The following equations describe the (α, β) components and the reference voltages:

$V_{ref1} = \cos \omega t$

$V_{ref2} = \cos(\omega t - 120^\circ)$

$V_{ref3} = \cos(\omega t + 120^\circ)$

$U_{alfa} = \sin \omega t$

U_{beta} =cos ωt

Note that, the above voltages are all normalized by the maximum phase voltage ($VDC/\sqrt{3}$).

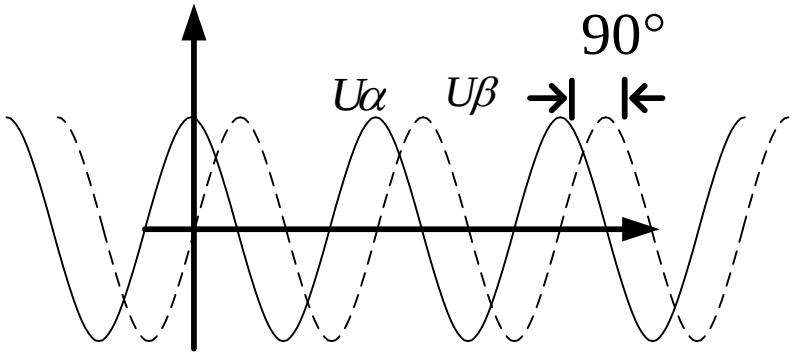

Figure A. 9 (α, β) components stator reference voltage

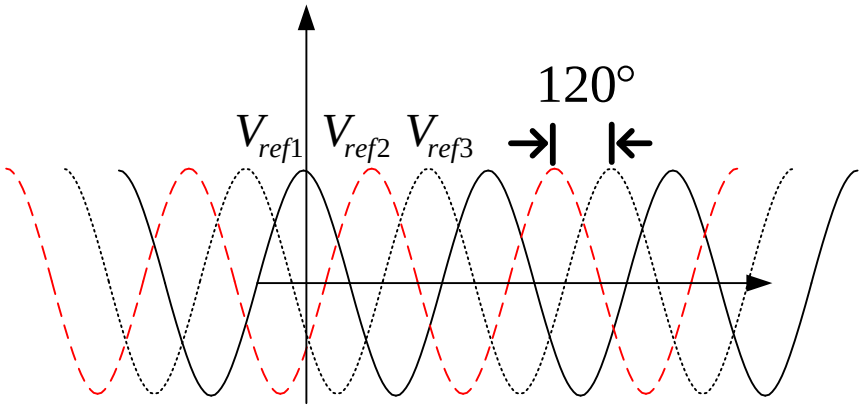

Figure A. 10 Voltages V_{ref1}, V_{ref2} & V_{ref3}.

$if\ V_{ref1} > 0\ then\ a = 1, else\ a = 0;$

$if\ V_{ref2} > 0\ then\ b = 1, else\ b = 0;$

$if\ V_{ref3} > 0\ then\ c = 1, else\ c = 0;$

The variable sector in the code is defined as, sector = $4c\ +\ 2b\ +\ a$

For example, in figure A.7 a=1 for the vectors $U300, U0$ and $U60$. For these vectors the phase of V_{ref1} are $\omega t = 300^{\circ}$, $\omega t = 0^{\circ}$ and $\omega t = 60^{\circ}$ respectively. Therefore, $V_{ref1} > 0$ when a $= 1$.

The (α, β) components, U_α and U_β , defined above represent the output phase voltages v_{AN}, v_{BN} and v_{CN}. The following equations describe these phase voltages:

$v_{AN} = \sin \omega t$

$v_{BN} = \sin(\omega t + 120^\circ)$

$v_{CN} = \sin(\omega t - 120^\circ)$

The space vector PWM module is divided in several parts:

- Determination of the sector
- Calculation of X, Y and Z
- Calculation of $t1$ and $t2$
- Determination of the duty cycle t_{a-on}, t_{b-on} and t_{c-on}
- Assignment of the duty cycles to Ta, Tb and Tc
- The variables t_{a-on}, t_{b-on} and t_{c-on} are calculated using the following equations:

$$t_{a-on} = \frac{PWM\ Period - t_1 - t_2}{2}$$

$$t_{b-on} = t_{a-on} + t_1$$

$$t_{c-on} = t_{b-on} + t_2$$

Then the right duty cycle $(t_{a-on}, t_{b-on}\ or\ t_{c-on})$ is assigned to the right motor phase, in other words, to Ta, Tb, Tc, according to the sector. Table A.4 depicts this determination.

Table A.4 Table assigning the right duty cycle to the right motor phase.

Sectors	$U0, U60$	$U0, U60$	$U0, U180$	$U180, U240$	$U240, U300$	$U300, U0$
Ta	t_{a-on}	t_{b-on}	t_{c-on}	t_{c-on}	t_{b-on}	t_{a-on}
Tb	t_{b-on}	t_{a-on}	t_{a-on}	t_{b-on}	t_{c-on}	t_{c-on}
Tc	t_{c-on}	t_{c-on}	t_{b-on}	t_{a-on}	t_{a-on}	t_{b-on}

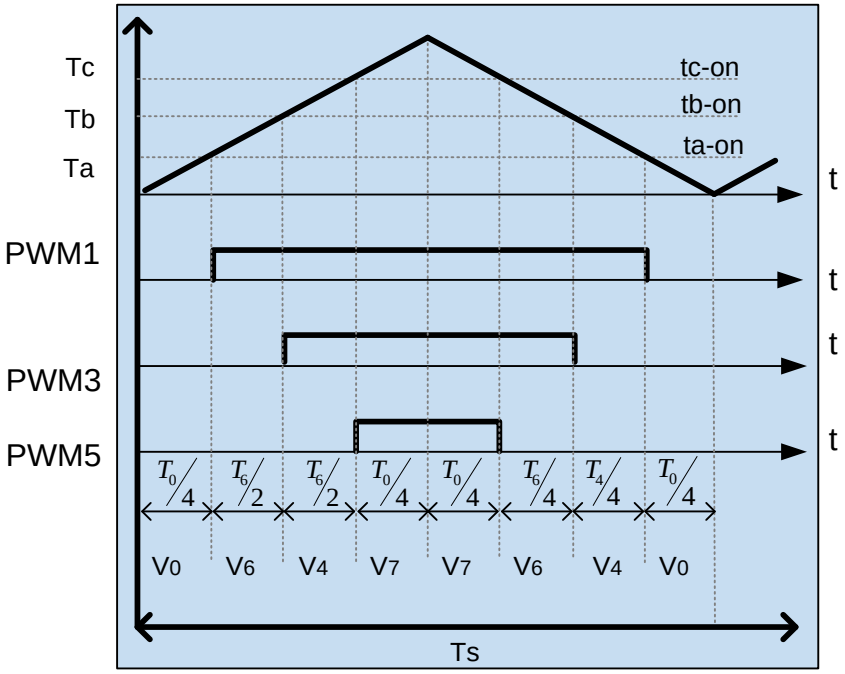

Figure A. 11 PWM patterns and duty cycle for sector contained by U0 and U60.

Appendix B - Modelling of Induction Machine

B.1 **Voltage and Current Equations in Stator Reference Frame**

Using vector notation, the stator and rotor winding can be represented by simple resistive-inductive circuits as described in Figure B.1 According to Faraday's law, an emf induced in a coil is proportional to the rate of change of flux linkage in the coil. Using Faraday's and Kirchhoff's voltage laws an induction motor machine model can be described mathematically using a set of differential equations. Via space vector notation the equation in the stator winding can be written as:

$$\overline{v_s^s} = R_s \overline{i_s^s} + \frac{d\overline{\psi_s^s}}{dt} \tag{B.1}$$

and that of the rotor winding:

$$\overline{v_r^r} = R_r \overline{i_r^r} + \frac{d\overline{\psi_r^r}}{dt} \tag{B.2}$$

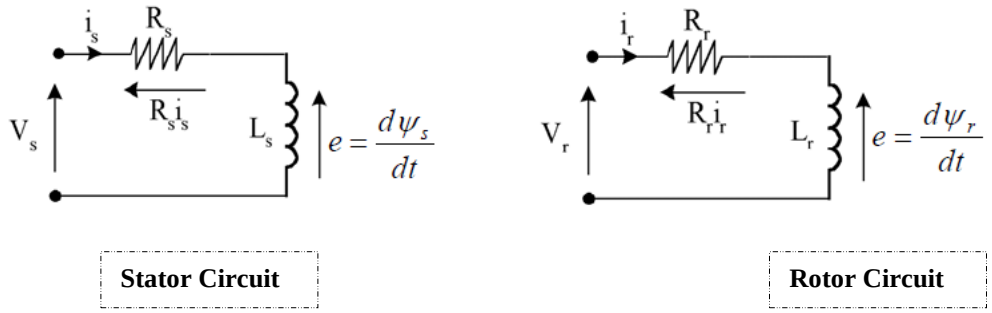

Figure B. 1 Resistive-inductive equivalent circuit of induction machine.

The superscripts s & r stand for the stator and rotor reference frames while the subscripts s & r stand for the stator and rotor quantities. Where and are the per phase stator and rotor resistances respectively. Expressing the rotor's voltage in the stator reference frame requires transforming rotor quantities into stator-referred quantities. Transformation of actual rotor vectors into stator referred vectors with respect to turns ratio is similar to that used in steady state theory of the transformer. In such a transformation, the actual rotor current is divided by n while the rotor voltage and flux

linkage are multiplied by n, where n is the ratio of the number of primary turns to that of the secondary turns. To account for rotational motion, operator $e^{j\theta}$, is employed and the resulting transformation is as follows:

$$\bar{\imath}_r^s = \frac{e^{j\theta}}{n} . \bar{\imath}_r^r \tag{B.3}$$

$$\bar{v}_r^s = ne^{j\theta} . \bar{v}_r^r \tag{B.4}$$

$$\bar{\psi}_r^s = ne^{j\theta} . \overline{\psi}_r^r \tag{B.5}$$

Rearranging (A-3), results in

$$\bar{\imath}_r^r = n . e^{-j\theta} . \bar{\imath}_r^s \tag{B.6}$$

The relation between the actual rotor resistance and the stator-referred resistance with respect to the turns ratio is

$$R_r^s = n^2 R_r^r \tag{B.7}$$

Substitute (B.2) with (B.6) and re-arrangement of (B.4) and (B.5) gives:

$$\bar{v}_r^r = R_r \bar{\imath}_r^r + \frac{d\bar{\psi}_r^r}{dt}$$

$$\frac{\bar{v}_r^s}{n} . e^{-j\theta} = \frac{R_r^s}{n^2} . n\bar{\imath}_r^s . e^{-j\theta} + \frac{d(\bar{\psi}_r^s . e^{-j\theta})}{ndt}$$

$$\frac{\bar{v}_r^s}{n} . e^{-j\theta} = \frac{R_r^s}{n^2} . n\bar{\imath}_r^s . e^{-j\theta} + \frac{1}{n}\left\{\frac{d\bar{\psi}_r^s}{dt} \mathrm{e}^{-j\theta} + \mathrm{e}^{-j\theta}\bar{\psi}_r^s(-\mathrm{j}\frac{\mathrm{d}\theta}{\mathrm{dt}})\right\}$$

Eliminate the term n, $e^{j\theta}$ and let $\frac{d\theta}{dt} = \omega_r$ which is the angular rotor speed. Use differential operator $\frac{d}{dt} = p$ and re-arrange the above equation resulting in

$$\bar{v}_r^s = R_r^s \bar{\imath}_r^s + \frac{d\bar{\psi}_r^s}{dt} - j\bar{\psi}_r^s \omega_r$$

$$\bar{v}_r^s = R_r \bar{\imath}_r^s + \bar{\psi}_r^s (p - j\omega_r) \tag{B.8}$$

Equation (B-8) is the rotor voltage equation expressed in the stationary reference frame. Subscript ‘s’ on stator referred rotor resistance is eliminated for clarity.

The flux linkage vectors $\bar{\psi}_r^s$, $\bar{\psi}_s^s$ can be expressed in terms of current vectors $\bar{\imath}_r^{sr}$, $\bar{\imath}_s^s$ and motor inductance.

$$\begin{bmatrix}\bar{\psi}_s^s \\ \bar{\psi}_r^s\end{bmatrix} = \begin{bmatrix}L_s & L_m \\ L_m & L_r\end{bmatrix}\begin{bmatrix}\bar{\imath}_s^s \\ \bar{\imath}_r^s\end{bmatrix} \quad \text{(B.9)}$$

$$L_s = L_m + L_{ls}$$

$$L_r = L_m + L_{lr}$$

Where L_m is the mutual inductance, L_s, L_r are the self-inductance of the stator and rotor respectively. L_{ls}, L_{lr} are the stator and rotor leakage inductance respectively. Substituting flux linkage vectors in (B.1) and with (B.9) results in the following equations.

Stator voltage vectors:

$$\bar{v}_s^s = R_s\bar{\imath}_s^s + p(L_s\bar{\imath}_s^s + L_m\bar{\imath}_r^s)$$

$$\bar{v}_s^s = (R_{s+} + pL_{s)}\bar{\imath}_s^s + pL_m\bar{\imath}_r^s) \quad \text{(B.10)}$$

Rotor voltage vectors:

$$\bar{v}_r^s = R_r\bar{\imath}_r^s + (L_r\bar{\imath}_r^s + L_m\bar{\imath}_s^s)(p - j\omega_r)$$

$$\bar{v}_r^s = R_r\bar{\imath}_r^s + (L_r\bar{\imath}_r^s + L_m\bar{\imath}_s^s)p - j\omega_r(\,L_r\bar{\imath}_r^s + L_m\bar{\imath}_s^s)$$

$$\bar{v}_r^s = (R_r + (p - j\omega_r)L_r)\bar{\imath}_r^s + (p - j\omega_r)L_m\bar{\imath}_s^s \quad \text{(B.11)}$$

Substitute (B-11) with their d-q-axis components yields:

$$v_{dr}^s + jv_{qr}^s = (R_r + (p - j\omega_r)L_r(i_{dr}^s + ji_{qr}^s) + (p - j\omega_r)L_m(i_{ds}^s + ji_{qs}^s)$$

$$v_{dr} = R_r i_{dr} + pL_r i_{dr} + pL_m i_{ds} + \mathrm{P}\omega_r L_r i_{qr} + \mathrm{P}\omega_r L_m i_{qs} \quad \text{(B .12)}$$

$$v_{qr} = R_r i_{qr} + pL_r i_{qr} + pL_m i_{qs} - \mathrm{P}\omega_r L_r i_{dr} - \mathrm{P}\omega_r L_m i_{ds} \quad \text{(B .13)}$$

Term P was added for a machine having P-pole pairs. Previously, it was assumed the machine has two-poles.

In matrix form the stator and rotor equation can be written as:

$$\begin{bmatrix}\bar{v}_s^s \\ \bar{v}_r^s\end{bmatrix} = \begin{bmatrix}R_s + pL_s & pL_m \\ (p - j\omega_r) & R_r + (p - j\omega_r)\end{bmatrix}\begin{bmatrix}\bar{\imath}_s^s \\ \bar{\imath}_r^s\end{bmatrix} \quad \text{(B.14)}$$

In vector control, stator and rotor vector quantities are represented using dq-axis model.

Voltage vectors:

$$\bar{v}_s^s = v_{ds} + jv_{qs} \quad \text{(B.15)}$$

$$\bar{v}_r^s = v_{dr} + jv_{qr} \quad \text{(B.16)}$$

Current vectors:

$$\bar{\imath}_s^s = i_{ds} + ji_{qs} \quad \text{(B.17)}$$

$$\bar{\imath}_r^s = i_{dr} + ji_{qr} \quad \text{(B.18)}$$

Flux linkage vectors:

$$\bar{\psi}_s^s = \psi_{ds} + j\psi_{qs} \quad \text{(B.19)}$$

$$\bar{\psi}_r^s = \psi_{dr} + j\psi_{qr} \quad \text{(B.20)}$$

Substituting all the vector quantities with their associated dq-components results in the following equations:

$$v_{ds} + jv_{qs} = (R_s + pL_s)(i_{ds} + ji_{qs}) = pL_m(i_{dr} + ji_{qr})$$

$$\bar{v}_s^s = (R_s + pL_s)\bar{\imath}_s^s + pL_m\bar{\imath}_r^s$$

Collecting the direct and quadrature terms yields:

$$v_{ds} = (R_s + pL_s)i_{ds} + pL_m i_{dr} \quad \text{(B.20)}$$

$$v_{qs} = (R_s + pL_s)i_{qs} + pL_m i_{qr} \quad \text{(B.21)}$$

The rotor flux linkage vector can be written as:

$$\bar{\psi}_r^s = L_r\bar{\imath}_r^s + L_m\bar{\imath}_s^s$$

$$\psi_{dr} + j\psi_{qr} = L_r(i_{dr} + ji_{qr}) + L_m(i_{ds} + ji_{qs})$$

Collecting the real and imaginary parts together yields:

$$\psi_{dr} = L_r i_{dr} + L_m i_{ds} \quad \text{(B.22)}$$

$$\psi_{qr} = L_r i_{qr} + L_m i_{qs} \quad \text{(B.23)}$$

Solving for i_{dr} and i_{qr} gives:

$$i_{dr} = \frac{\psi_{dr} - L_m i_{ds}}{L_r} \quad \text{(B.24)}$$

$$i_{qr} = \frac{\psi_{qr} - L_m i_{qs}}{L_r} \quad \text{(B.25)}$$

Substitute rotor currents in (B.20) and (B.21) with (B.24) and (B.25) respectively:

$$v_{ds} = (R_s + pL_s)i_{ds} + pL_m\left(\frac{\psi_{dr} - L_m i_{ds}}{L_r}\right)$$

$$v_{ds} = (R_s + pL_s)i_{ds} + p\frac{L_m}{L_r}\psi_{dr} - p\frac{L^2{}_m}{L_r}i_{ds} \quad \text{(B.26)}$$

$$v_{qs} = (R_s + pL_s)i_{qs} + pL_m\left(\frac{\psi_{qr} - L_m i_{qs}}{L_r}\right)$$

$$v_{qs} = (R_s + pL_s)i_{qs} + p\frac{L_m}{L_r}\psi_{qr} - p\frac{L^2{}_m}{L_r}i_{qs} \quad \text{(B.27)}$$

Re-arranging (B.26) and (B.27) and solving for rotor flux linkage vectors, yields:

$$p\psi_{dr} = \left(v_{ds} - (R_s + pL_s)i_{ds} + p\frac{L^2{}_m}{L_r}i_{ds}\right)\frac{L_r}{L_m} \quad \text{(B.28)}$$

$$p\psi_{qr} = \left(v_{qs} - (R_s + pL_s)i_{qs} + p\frac{L^2{}_m}{L_r}i_{qs}\right)\frac{L_r}{L_m}$$

Recall the rotor voltage vector:

$$\overline{v_r^s} = R_r\overline{i_r^s} + (p - j\omega_r)\bar{\psi}_r^s$$

Substitute voltage, rotor and stator currents with its dq-components

$$v_{dr} + jv_{qr} = R_r\left(i_{dr} + ji_{qr}\right) + (p - j\omega_r)(\psi_{dr} + j\psi_{qr})$$

Collecting the d-q components together yields:

$$v_{dr} = R_r i_{dr} + p\psi_{dr} + \omega_r\psi_{qr} \quad \text{(B.30)}$$

$$v_{qr} = R_r i_{qr} + p\psi_{qr} - \omega_r\psi_{dr} \quad \text{(B.31)}$$

Substitute rotor currents in (B.30) with (B.31)

$$v_{dr} = R_r\left(\frac{\psi_{dr} - L_m i_{ds}}{L_r}\right) + p\psi_{dr} + \omega_r\psi_{qr}$$

$$v_{dr} = \frac{R_r}{L_r}\psi_{dr} - \frac{R_r}{L_r}L_m i_{ds} + p\psi_{dr} + \omega_r\psi_{qr}$$

Re-arrange and solve for d-axis rotor flux linkage yields:

$$p\psi_{dr} = v_{dr} + \frac{R_r}{L_r}(L_m i_{ds} - \psi_{dr}) - \omega_r\psi_{qr} \quad \text{(B.32)}$$

Similar substitution for rotor current in (B.31) using (B.25) results in:

$$v_{qr} = \frac{R_r}{L_r}\psi_{qr} - \frac{R_r}{L_r}L_m i_{qs} + p\psi_{qr} - \omega_r\psi_{dr}$$

$$v_{qr} = R_r\left(\frac{\psi_{qr} - L_m i_{qs}}{L_r}\right) + p\psi_{qr} - \omega_r\psi_{dr}$$

Re-arrange and solving for q-axis rotor flux linkage yields:

$$p\psi_{qr} = v_{qr} + \frac{R_r}{L_r}\left(L_m i_{qs} - \psi_{qr}\right) + \omega_r\psi_{dr} \quad \text{(B.33)}$$

For a squirrel cage machine, the rotor is short circuited therefore d-q voltage components are zero and (B.32) and (B.33) can be simplified as:

$$p\psi_{dr} = \frac{R_r}{L_r}(L_m i_{ds} - \psi_{dr}) - \omega_r\psi_{qr} \quad \text{(B.34)}$$

$$p\psi_{qr} = \frac{R_r}{L_r}\left(L_m i_{qs} - \psi_{qr}\right) + \omega_r\psi_{dr} \quad \text{(B.35)}$$

B.2 **Electromagnetic Torque**

The power flowing into the machine is clearly the instantaneous product of the voltage across and currents through the machine windings. The torque developed can be derived using the power flow relationship in the machine. Consider, the instantaneous power flowing into the dq-equivalent two-pole machine in the synchronously rotating reference frame.

$$p = \frac{3}{2}(v_{ds}i_{ds} + v_{qs}i_{qs} + v_{dr}i_{dr} + v_{qr}i_{qr}) \quad \text{(B.36)}$$

The term 3/2 is the proportionality constant between three-phase quantities and the resulting dq-equivalents. Transforming Equation (B.1) and (B.2) into synchronously rotating frame yields

$$\bar{v}_s = R_s\bar{\imath}_s + \frac{\overline{d\psi}_r^s}{dt} + j\omega_r\bar{\psi}_s) \quad \text{(B.37)}$$

$$\bar{v}_r = R_r\bar{\imath}_r + \frac{d\bar{\psi}_r}{dt} + j(\omega - \omega_r)\bar{\psi}_r \quad \text{(B.38)}$$

Where, ω is the speed of the synchronously rotating reference frame.

Solving equation (B.37) and (B.38) into the dq-components, and substitute them into the instantaneous power equation (B.36) results in:

$$p = \frac{3}{2}(\psi_{qr} i_{dr} - \psi_{dr} i_{qr})\omega_r \quad \text{(B.39)}$$

The torque generated by rotating mass at the speed of ω_r with power P_o can be calculated as:

$$T = \frac{P_0}{\omega_r} \quad \text{(B.40)}$$

Substitute (B.39) into (B.40) and generalize the equation for a P-pole machine yields:

$$T = \frac{3}{2}\frac{P_0}{2}(\psi_{qr} i_{dr} - \psi_{dr} i_{qr}) \quad \text{(B.41)}$$

B.3 **Mechanical Modeling**

The electromechanical equation that governs behavior of the machine can be represented as:

$$T_e = J\frac{d\omega_r}{dt} + T_L \quad \text{(B.42)}$$

Where, J is the inertia of the system, $T_e$is the electromagnetic torque produced by the machine, ω_r is the rotor speed and T_L is the load.

Appendix C - Simulink® Modelling

This appendix describes the construction of the Simulink® blocks for voltage-fed model of the induction machine and mechanical model of the system.

C.1 Induction Motor Simulink® Model

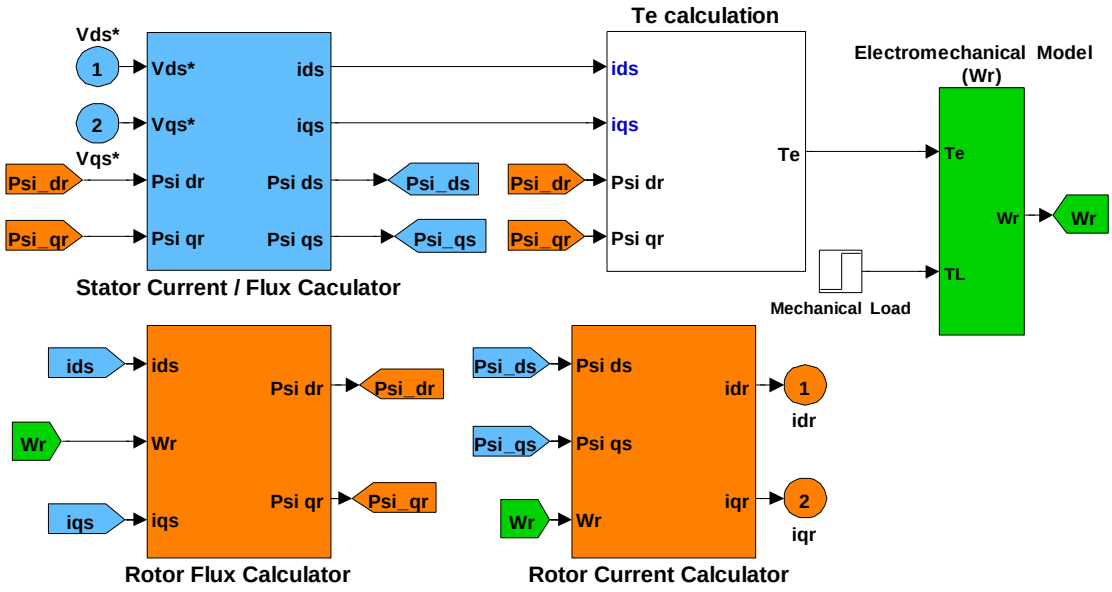

Figure C. 1 Induction motor simulink® model.

By rearranging equations (B.20) and (B.21) in terms of i_{ds} and i_{qs} as well as substituting i_{dr} and i_{qr} with their respective values in equations (B.24) and (B.25) yields:

$$i_{ds} = [L_r \int (v_{ds} + R_s i_{ds})dt - L_m \psi_{dr}] i_{dr} \frac{1}{L_s L_r - {L_m}^2} \quad \text{(C.1)}$$

$$i_{qs} = [L_r \int (v_{qs} + R_s i_{qs})dt - L_m \psi_{qr}] i_{dr} \frac{1}{L_s L_r - {L_m}^2} \quad \text{(C.2)}$$

Figure C.2 Shows the Simulink® representation of the above two equation which calculate the stator currents and the stator flux.

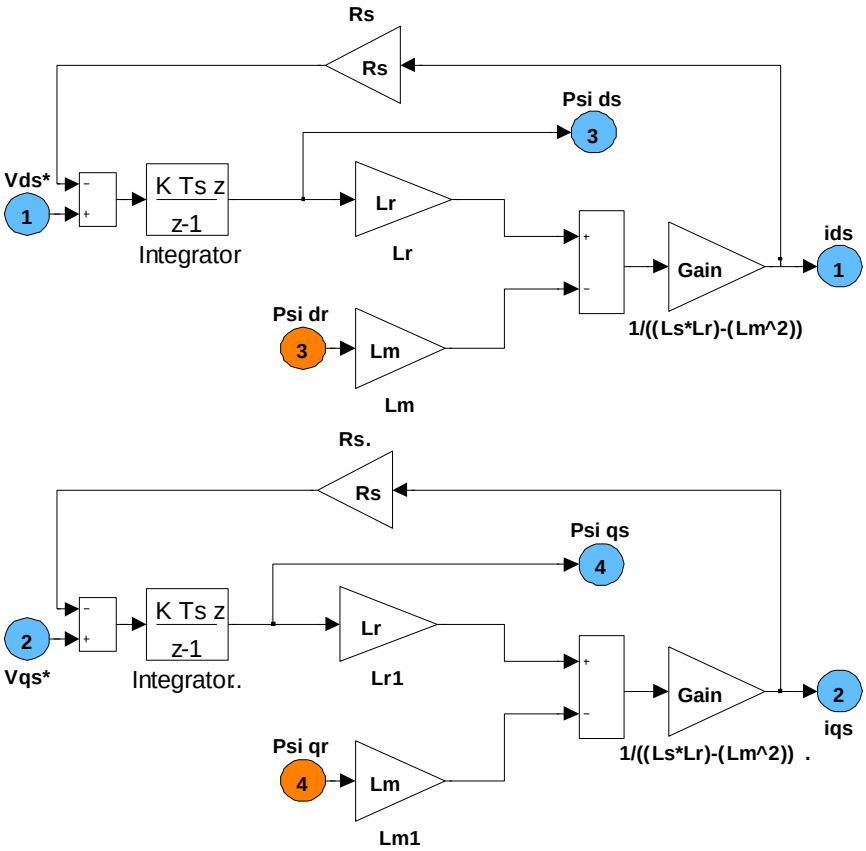

Figure C. 2 Stator current and stator flux calculator.

The rotor flux calculator is based on equation (B.34) and equation (B.35).

$$\psi_{dr} = \int \left(\frac{R_r}{L_r}\left(L_m i_{ds} - \psi_{dr}\right) - \omega_r \psi_{qr}\right) dt \tag{C.3}$$

$$\psi_{qr} = \int \left(\frac{R_r}{L_r}\left(L_m i_{qs} - \psi_{qr}\right) - \omega_r \psi_{dr}\right) dt \tag{C.4}$$

The Simulink® block implementation of the rotor flux calculator is shown in Figure C.3.

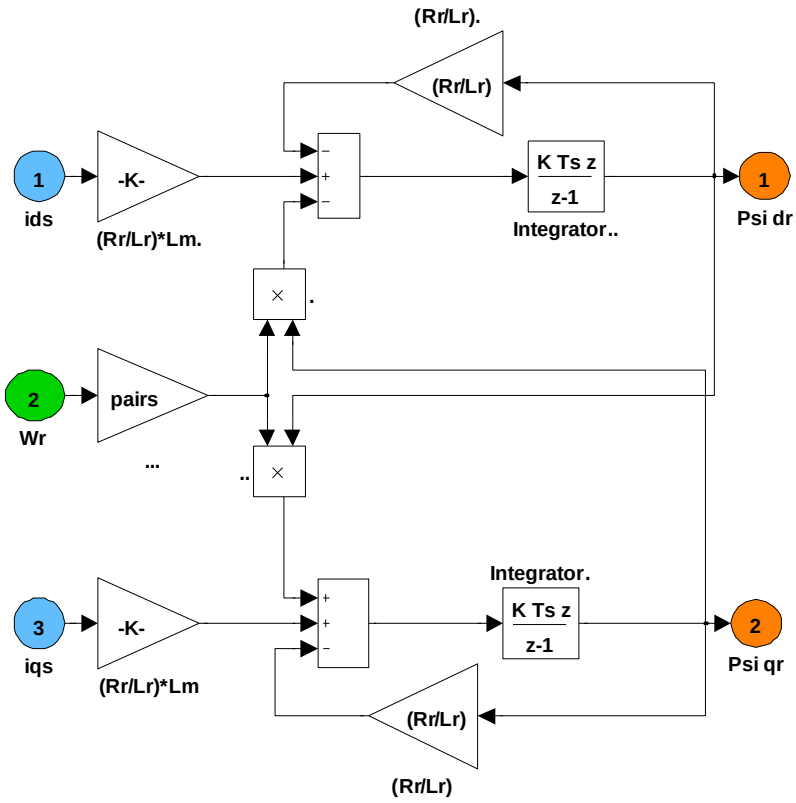

Figure C. 3 Rotor flux calculator.

The rotor circuit is based on equations (B.30) and (B.31) which were re-arranged and solved to calculate (ψ_{dr}, ψ_{qr}) and considering the fact that the rotor is short circuited, yields:

$$v_{dr} = R_r i_{dr} + p\psi_{dr} + \omega_r \psi_{qr} \quad \text{(B.30)}$$

$$v_{qr} = R_r i_{qr} + p\psi_{qr} - \omega_r \psi_{dr} \quad \text{(B.31)}$$

$$\psi_{dr} = \int \left(-R_r i_{dr} - \omega_r \psi_{qr}\right) dt \quad \text{(C.5)}$$

$$\psi_{qr} = \int \left(-R_r i_{dr} + \omega_r \psi_{dr}\right) dt \quad \text{(C.6)}$$

Manipulate equations of rotor flux, currents and voltage resulting in explicit form of (d, q) rotor currents as shown below:

$$i_{dr} = (\psi_{dr} L_s - \psi_{ds} L_m) \frac{1}{L_r L_s - {L_m}^2} \quad \text{(C.7)}$$

$$i_{qr} = (\psi_{qr} L_s - \psi_{qs} L_m) \frac{1}{L_r L_s - {L_m}^2} \quad \text{(C.8)}$$

The Simulink® implementation is shown in Figure C.4.

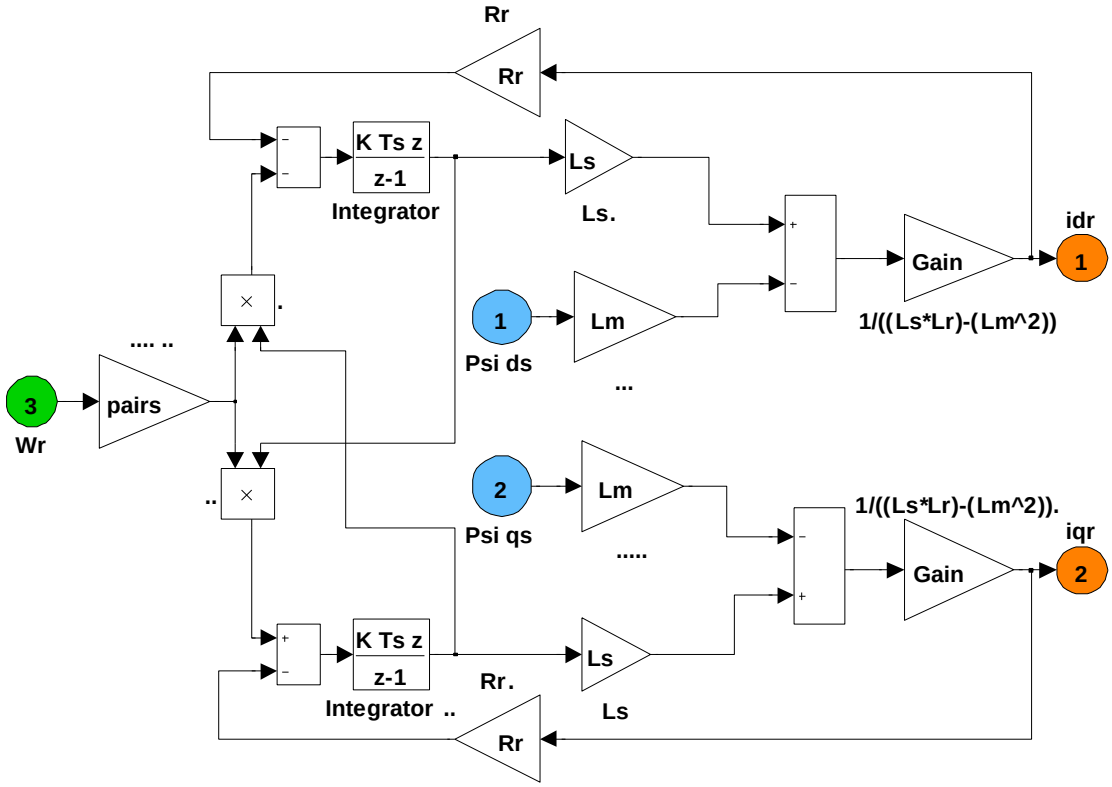

Figure C. 4 Rotor current calculator.

Figure C.5 shows the electromagnetic torque model of the machine that was constructed using Equation (B.41) using output rotor's circuit of Figure C.4.

$$T = \frac{3}{2}\frac{P_0}{2}(\psi_{qr} i_{dr} - \psi_{dr} i_{qr}) \quad \text{(B.41)}$$

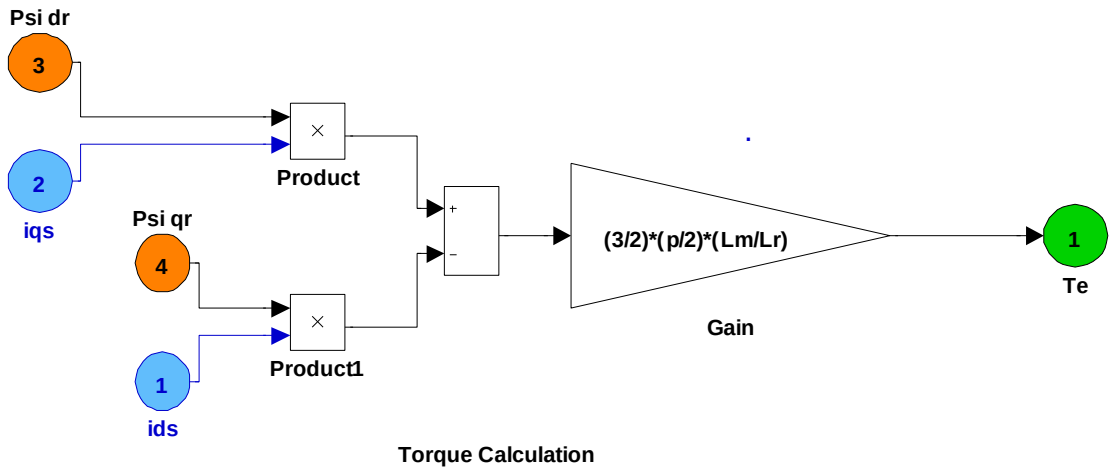

Figure C. 5 Electromagnetic torque calculator.

C.2 Mechanical model

Mechanical modelling as shown in equation (B.42) is implemented in Simulink® as shown in Figure C.5.

$$T_e = J\frac{d\omega_r}{dt} + T_L \qquad \text{(B.42)}$$

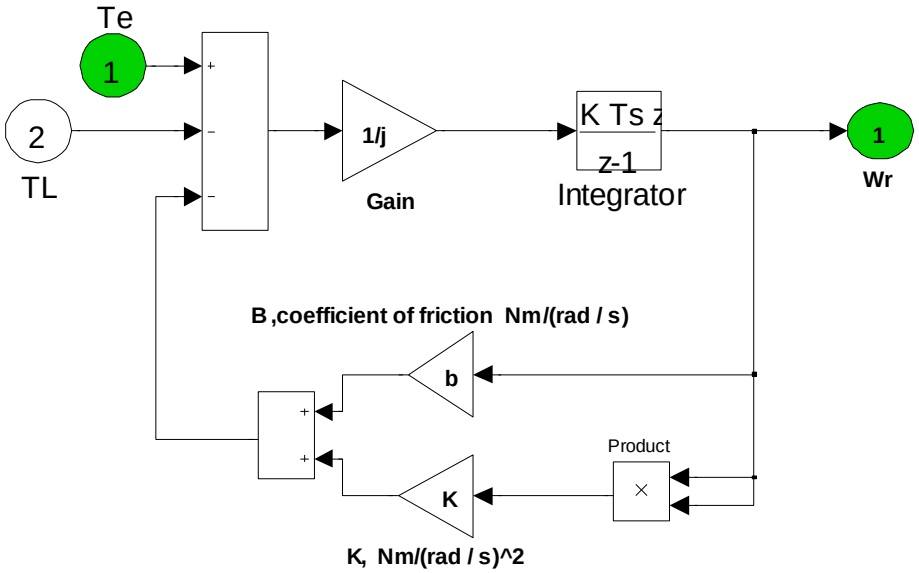

Figure C. 6 Electromechanical model.

C.3 MRAS Simulink® Model

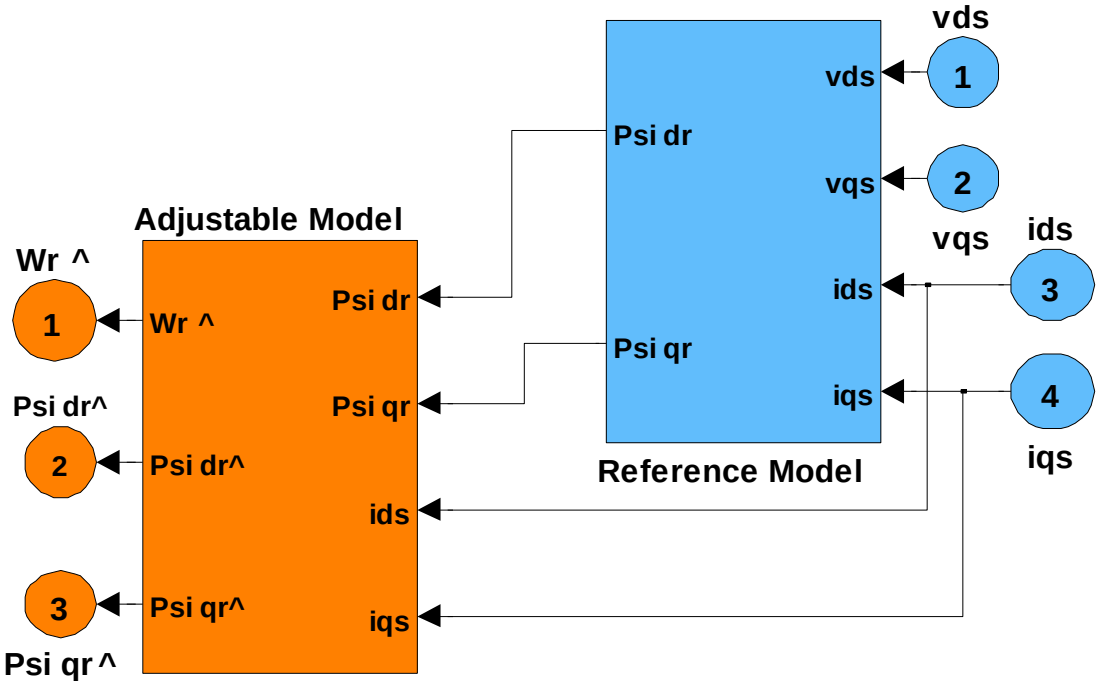

Figure C. 7 MRAS - simulink® model.

$$\psi_{dr}{}^{s} = \frac{L_r}{L_m}\left(\int(V_{ds}{}^{s} - R_s i_{ds}{}^{s})dt + \sigma L_s i_{ds}{}^{s}\right) \quad (3.30)$$

$$\psi_{qr}{}^{s} = \frac{L_r}{L_m}\left(\int(V_{qs}{}^{s} - R_s i_{qs}{}^{s})dt + \sigma L_s i_{qs}{}^{s}\right) \quad (3.31)$$

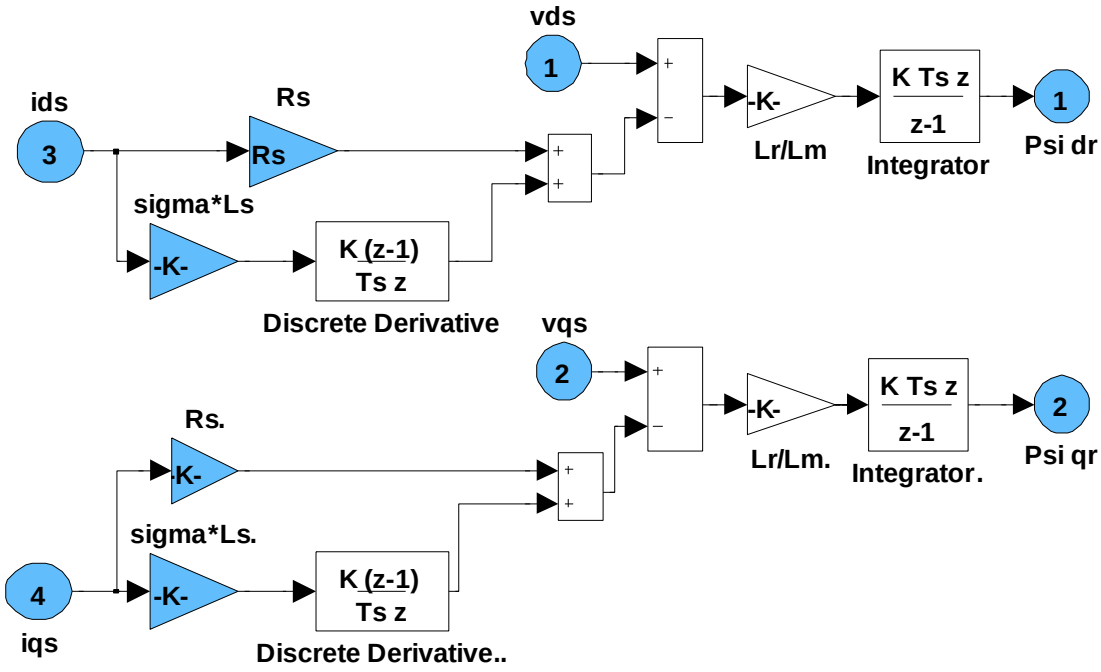

Figure C. 8 MRAS - reference model.

$$\frac{d\psi_{dr}{}^{s}}{dt} = \frac{L_m}{T_r} i_{ds}{}^{s} - \omega_r \psi_{qr}{}^{s} - \frac{1}{T_r} \psi_{dr}{}^{s} \tag{3.37}$$

$$\frac{d\psi_{qr}{}^{s}}{dt} = \frac{L_m}{T_r} i_{qs}{}^{s} + \omega_r \psi_{dr}{}^{s} - \frac{1}{T_r} \psi_{qr}{}^{s} \tag{3.38}$$

$$\omega_r(t) = K_p . \varepsilon_\psi(t) + K_i \int \varepsilon_\psi(t)\, dt$$

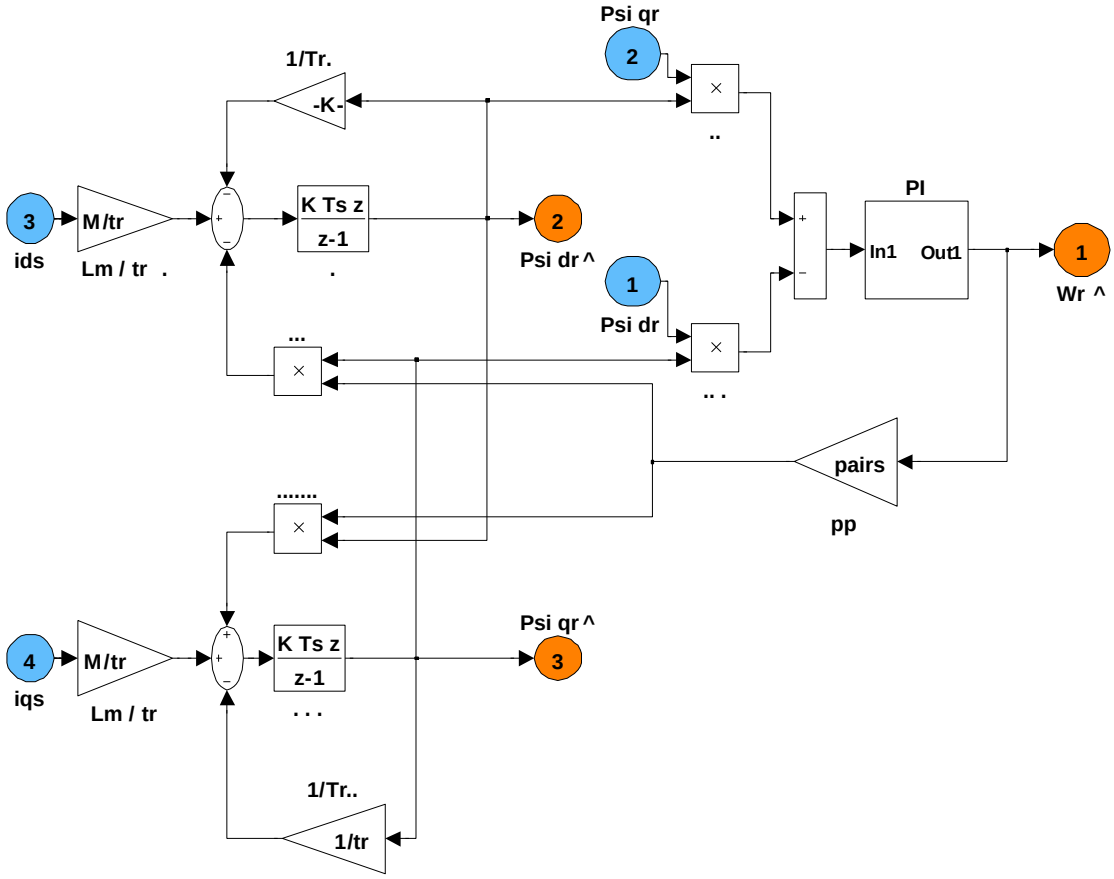

Figure C. 9 MRAS - adaptive model.

Blank Page

Blank Page